DOCTORAATSPROEFSCHRIFT

Faculteit Wetenschappen

Influence of nitrogen on the growth of diamond thin films by microwave plasma assisted Chemical Vapour Deposition

Proefschrift voorgelegd tot het behalen van de graad van
Doctor in de Wetenschappen, richting Natuurkunde

THIERRY VANDEVELDE

Promotor : Prof. dr. L.M. Stals

2000

INSTITUUT VOOR MATERIAALONDERZOEK

LIMBURGS
UNIVERSITAIR
CENTRUM
IN HET CENTRUM VAN DE KENNIS

DOCTORAATSPROEFSCHRIFT

Faculteit Wetenschappen

Influence of nitrogen on the growth of diamond thin films by microwave plasma assisted Chemical Vapour Deposition

Proefschrift voorgelegd tot het behalen van de graad van
Doctor in de Wetenschappen, richting Natuurkunde

THIERRY VANDEVELDE

Promotor : Prof. dr. L.M. Stals

2000

INSTITUUT VOOR MATERIAALONDERZOEK

LIMBURGS
UNIVERSITAIR
CENTRUM
IN HET CENTRUM VAN DE KENNIS

According to the guidelines of the Limburgs Universitair Centrum, a copy of this publication has been filed in the Royal Library Albert I, Brussels, as publication D/2000/2451/122

Chairman :

Prof. Dr. Freddy Dumortier
Vice-rector LUC

Promotor :

Prof. Dr. Lambert Stals
IMO-LUC

Members of the jury :

Prof. Dr. Volker Buck
Universität GH Essen
Dr. Volker Schulz-von der Gathen
Universität GH Essen
Prof. Dr. Renaat Gijbels
UIA
Prof. Dr. Ir. Jean Vereecken
VUB
Prof. Dr. Ir. Annick Hubin
VUB
Prof. Dr. Jean-Pierre François
LUC
Prof. Dr. Gilbert Knuyt
LUC
Dr. Milos Nesladek
IMO-LUC

To my wife Ann for her love and support,
and to our daughter Sarah for fulfilling my life.

Thierry

Acknowledgements

I am mostly obliged to Professor Lambert Stals for having given me the opportunity to achieve my PhD at the Materials Physics Division of the Institute for Materials Research (Limburgs Universitair Centrum). His fruitful discussions and support made this work possible.

I thank the I.R.S.I.A. and the I.W.T. for having supported my work financially.

I am grateful to Ir. Marc Van Stappen who allowed me to put the final touch to my thesis during my working hours.

I cannot forget all the people, as well academics as technicians, who, whichever the way you look at it, contributed to the elaboration of this work. I could not have managed this work without you.

Finally, I want to thank my parents for their encouragement throughout these years.

Thierry Vandevelde, December 2000.

Table of contents

Abstract

It is well known that nitrogen can seriously influence the growth of diamond films during Plasma Assisted-Chemical Vapour Deposition (PA-CVD) *(Chapter 1)*. If the generic mechanisms by which diamond is deposited at pressures and temperatures at which it is thermodynamically metastable are well understood, generally accepted chemical mechanisms that lead to low-pressure growth of diamond are still lacking, even for the most commonly used binary methane-hydrogen feed gas mixture. Therefore, the mechanisms of nitrogen incorporation in the diamond film are still missing too. This is mainly due to the extreme complexity of the processes involved, as it is unlikely that there is a single and simple diamond growth mechanism that applies to all deposition systems and deposition conditions *(Chapter 2)*.

In this work, Optical Emission Spectroscopy (OES), proviso the needed precautions, is used as a non-intrusive analysis technique to monitor variations in the plasma chemistry during microwave PA-CVD. Semi-quantitative analysis is made possible by the use of actinometry, while the temperature of some plasma species is determined by using the so-called Boltzmann plot technique *(Chapter 3)*. It is proven for the first time that small nitrogen fractions can seriously modify the plasma chemistry, such as the relative concentration and the temperature of the light emitting species in the plasma. A home-made optical probe was built to reduce drastically the volume captured by the optical set-up, allowing us to achieve some spatial resolution. With the optical probe, we show that the spatial distribution as well as the temperature of the light emitting species varies together with the distance from the substrate surface. We demonstrate that plasma chemical reactions as well as surface chemical reactions lead to the production of the presumed precursors responsible for the growth of CVD diamond *(Chapter 4)*.

Characterisation of the deposited films by Scanning Electron Microscopy, X-ray diffraction, micro-Raman analysis and Secondary-Ion Mass Spectrometry demonstrate respectively the strong evolution in morphology, preferred orientation, film quality and relative concentration of hydrogen and nitrogen in the diamond film as a function of the nitrogen content in the feed gas mixture *(Chapter 5)*.

The plasma and surface reaction paths proposed in this work try to explain how the various plasma emitting species are produced and under which form nitrogen could be incorporated in the diamond lattice *(Chapter 6)*.

Finally, we draw some conclusions and proposed solutions to the problems encountered in this work *(Chapter 7)*.

Samenvatting

Introductie

Het idee van de synthese van diamant vond zijn oorsprong in de jaren 1770 toen Lavoisier en Tennant ontdekten dat diamant een kristalvorm van koolstof is.

Het is pas in de jaren 1920 dat men de eerste experimenten uitvoerde om kunstmatig diamant aan te maken. De eerste methode die gevolgd werd was het aanmaken van diamant in het gebied waar het thermodynamisch stabiel is. Extreem hoge temperaturen en drukken waren nodig om grafiet in diamant om te zetten. De eerste successen werden in de jaren 1950-1960 door Zweedse en Amerikaanse wetenschappers geboekt. Deze methode werd verbeterd door het gebruik van metallieke katalysatoren (Ni, Co, Fe). Zo wordt nu 90% van het diamantpoeder, gebruikt in abrasieve toepassingen, bereid langs hoge druk synthese. Eind 1952 ontwikkelde Eversole uit de Verenigde Staten een ander proces om kunstmatig diamant te produceren. Het berustte op een lage druk synthese in het thermodynamische domein waar diamant metastabiel is. Eversole maakte gebruik van een cyclische reactie op een verwarmd diamantsubstraat. Een koolstofgasbehandeling werd gevolgd door een waterstofbehandeling op hoge temperatuur en lage druk. Onder deze omstandigheden werd het koolstofgas door de hitte ontbonden om simultaan diamant en grafiet te vormen. Het gebruik van waterstof bij hoge temperatuur diende om het grafiet van het diamantsubstraat weg te etsen.

Deze uitvinding werd "Chemical Vapour Deposition" (CVD) genoemd. De groeisnelheid was nochtans heel laag tegenover de hoge druk processen en de CVD methode werd toen meer als een curiosum beschouwd. Het is pas in het begin van de jaren 80, toen het Japanse "National –Institute for Research in Inorganic Materials" (NIRIM) nieuwe afzettingstechnieken ontwikkelde, dat deze cyclische behandeling door een continu proces vervangen werd. Het afzettingsproces steunde op het gebruik van een plasma dat diende om de verschillende gasspecies te activeren. Atomaire waterstof en koolstofhoudende radicalen, die als precursors voor de groei van diamant dienen, worden onder andere in het plasma geproduceerd. Eindelijk konden aanvaardbare groeisnelheden (> 1µm/h) behaald worden. De moderne "Plasma Assisted-Chemical Vapour Deposition" (PA-CVD) was geboren.

Het plasma dient om de verschillende gasspecies te activeren. De activatie van het gasmengsel is van belang om atomaire waterstof te verkrijgen. In PA-CVD systemen, kan de activatie van de gasspecies onder andere met behulp van een vlam, een filament, radiofrequentie, of microgolven plaats vinden.

De morfologie van de deklaag kan voornamelijk beïnvloed worden door de depositieparameters (methaan-waterstofverhouding, druk en afzettingstemperatuur) aan te passen. Een andere manier om de morfologie van de diamantdeklaag te beïnvloeden, is het toevoegen van kleine hoeveelheden ongewoon gas (argon, helium of stikstof) aan het normale gasmengsel tijdens de afzetting. Het toevoegen van heel kleine stikstofverhoudingen in het gebruikelijke methaan-waterstof gasmengsel is verantwoordelijk voor een progressieve verandering in de morfologie en voor een verhoging in de groeisnelheid van de afgezette diamantdeklaag. Stikstof kan ook opgenomen worden in het diamantkristalrooster als substitutiespecie op dezelfde wijze als voor hoge druk synthetisch Ib diamant en de intrinsieke elektrische eigenschappen van de diamantdeklaag veranderen. Het substitutie stikstofatoom is een diepe donor, met een ionisatie energie van ongeveer 2eV. Stikstof gedoteerde diamanten zijn daarom niet geschikt voor halfgeleidertoepassingen. Vandaag zijn de recepten om verschillende diamantmorfologieën aan te maken grotendeels bekend. Toch is het groeimechanisme van diamant uitgaande van geactiveerde koolwaterstof gasspecies nog niet precies bekend.

In het kader van dit proefschrift interesseren we ons voor de invloed van het toevoegen van kleine hoeveelheden stikstof (ppm schaal) op de groei van diamantdeklagen op silicium (100) wafers, aangebracht met behulp van een Astex PDS-17 microgolf plasma ondersteund CVD systeem. De invloed van het toevoegen van stikstof op de fysische eigenschappen van het plasma, zoals de temperatuur van de gasspecies, en op de chemische eigenschappen van het plasma, zoals de chemische samenstelling, wordt met behulp van Optische Emissie Spectroscopie (OES) bestudeerd. Optische Emissie Spectroscopie heeft als voordeel ten opzichte van massa spectrometrie, het plasma niet te storen. Het grootste gebrek van de OES techniek is dat enkel en alleen maar de lichtemitterende species hiermee geïdentificeerd kunnen worden. Semi-kwantitatieve analyse met OES is nochtans mogelijk met het toepassen van actinometrie. Met actinometrie kunnen veranderingen in de concentratie van atomaire waterstof op de voet gevolgd worden door het toevoegen van enkele volumeprocenten argon. De temperatuur van de plasmaspecies werd m.b.v. de Botlzmann plot techniek en m.b.v. het Dopplereffect berekend.

De invloed van stikstof op de fysische en chemische eigenschappen van de diamantdeklaag kan met behulp van Scanning Electron Microscopy (SEM), X-stralen diffractie (XRD), micro-Raman Spectroscopy en Secondary-Ion Mass Spectroscopy (SIMS) gevolgd worden. Hiermee kunnen respectievelijk de morfologie, de voorkeursoriëntatie, de sp^2/sp^3 verhouding en de samenstelling van de diamantdeklaag bepaald worden.

Optische emissie spectroscopie

De OES opstelling bestaat uit een Jobin-Yvon HR 460 monochromator in een Cerny-Turner configuratie gekoppeld aan een Spectraview 2D CCD detector. Het lichtsignaal wordt naar de monochromator verstuurd m.b.v. een optische glasvezel. De grenshoek van de optische vezel is zo groot dat het volledige plasmavolume in een keer gemeten wordt. Om het volume gevangen door de optische vezel te reduceren, was het noodzakelijk een optisch systeem of optische meetsonde op te bouwen waarmee de samenstelling van het plasma in functie van de afstand van het substraatoppervlak gemeten kon worden. De optische meetsonde bestaat uit een cilindrisch buisje met een diameter van 10mm waarin een UV verrijkingslens en de optische vezel plaatsvinden. De afstand tussen de lens en het centrum van het plasma komt overeen met de brandpuntsafstand (f) van de lens, terwijl de afstand tussen de lens en de optische vezel f/2 bedraagt. Voor het gebruik, werd de spectrale afhankelijkheid van de volledige optische opstelling opgemeten m.b.v. een wolfram lamp waarvan de stralingsdichtheid bekend is.

De plasmasamenstelling is afhankelijk van de samenstelling van het gebruikte gasmengsel tijdens de afzettingen. Voor een methaan-waterstof plasma, vinden we atomaire waterstof (Balmer atomaire waterstof) emissielijnen, waterstof (H_2) Fulcher α systeem, CH $A^2\Delta$-$X^2\Pi$ en $B^2\Sigma$-$X^2\Pi$ systemen en C_2 Swan systeem in het optische emissie spectrum terug. Het toevoegen van stikstof in dit plasma zorgt voor de aanwezigheid van de CN emissiebanden (CN violet systeem) en zelfs voor de aanwezigheid van de N_2 emissiebanden bij hoge stikstofconcentratie (>2000ppm). Argon wordt in het plasma gedetecteerd door de aanwezigheid van de emissielijn op 750.4nm. De detectielimiet voor de verschillende geïdentificeerde gasspecies werd ook vastgelegd.

Invloed van stikstof op een methaan-waterstof plasma

In deze reeks experimenten werd de stikstof verhouding gewijzigd van 0vol.% tot 10vol.% op constant microgolfvermogen, druk, gasdebiet, methaan-waterstof verhouding en substraattemperatuur. Actinometrie toont aan dat de relatieve concentratie van atomaire waterstof (IH_α/IAr) verhoogt met een factor 1.5, terwijl de relatieve concentratie van moleculair waterstof vermindert met dezelfde factor tussen 0 – 1000ppm N_2. De relatieve concentratie van CN (ICN/IH_α), C_2 (IC_2/IH_α) en CH (ICH/IH_α) verhoogt met toenemende stikstofconcentratie in het gasmengsel. De ICN/IC_2 verhouding verhoogt met de stikstofconcentratie in het plasma, terwijl de ICH/IC_2 verhouding constant blijft over hetzelfde concentratie-interval. Deze resultaten suggereren dat stikstof de dissociatie van methaan bevordert, aangezien de productie van CN niet ten koste van de concentratie van de C_2 en CH radicalen gebeurt. Aangezien de concentratie van moleculaire waterstof vermindert met de toenemende stikstofconcentratie in het plasma, is het niet uitgesloten dat stikstof ook een invloed heeft op de dissociatiegraad van moleculaire waterstof in het plasma.

De temperatuur van waterstofatomen, berekend m.b.v. een Boltzmann plot, vermindert met toenemende stikstofconcentratie van 0 naar 1000ppm, terwijl de vibrationele temperatuur van de C_2 species verhoogt tussen hetzelfde interval.

Invloed van stikstof op het plasma

Het toevoegen van kleine hoeveelheden stikstof in het plasma is verantwoordelijk voor opvallende veranderingen in de chemie van het plasma. De relatieve concentratie van de CN, CH en C_2 radicalen verhoogt lineair met de toenemende stikstofverhouding in het procesgasmengsel (tussen 0 en 1000ppm N_2). Actinometrie toont aan dat de relatieve concentratie van atomaire waterstof stijgt met toenemende stikstofconcentratie in het plasma terwijl de concentratie van moleculair waterstof daalt over hetzelfde concentratiegebied. Aangezien de toename in de relatieve concentratie van de CN radicalen niet gebeurt ten koste van de relatieve concentratie van de CH en C_2 radicalen, kunnen we uit deze resultaten afleiden dat stikstof de dissociatiegraad van methaan verhoogd.

De temperatuur van waterstofatomen, berekend m.b.v. een Boltzmann plot, vermindert met toenemende stikstofconcentratie van 0 naar 1000ppm van respectievelijk 5330K tot 4600K, terwijl de vibrationele temperatuur van de C_2 species verhoogt in hetzelfde interval van respectievelijk 3050K tot 4500K. Het verschil tussen de vibrationele temperatuur van C_2 en de temperatuur van waterstofatomen vermindert met de toenemende stikstofconcentratie in het plasma. Voor stikstoffracties groter dan 475ppm zijn beide temperaturen gelijk. Dit resultaat suggereert dat stikstof verantwoordelijk is voor een thermalisatie van het plasma.

Distributie van de verschillende species in het plasma

Door in de hoogte de substraathouder millimeter per millimeter te verplaatsen was het mogelijk verschillen in de emissie intensiteiten van de plasmaspecies te registreren in functie van de afstand van het substraatoppervlak.

Voor een constante stikstofconcentratie in het plasma van 450ppm bleef de IH_α/IH_β verhouding constant van 1mm tot en met 12mm boven de substraatoppervlakte. De actinometrische IH_α/IAr and IH_β/IAr verhoudingen verhogen met een factor 2 over hetzelfde interval. De ICH/IH_α and IC_2/IH_α verhoudingen verhogen op een exponentiële wijze met de afstand van de substraatoppervlakte terwijl de ICN/IH_α verhouding vermindert over hetzelfde interval. De vermindering in de relatieve concentratie van de CN radicaal gebeurt grotendeels binnen de 2mm van het substraatoppervlak. De ICN/IC_2 en ICH/IC_2 verhoudingen verminderen ook in een exponentiële wijze van het substraatoppervlak naar de plasmabulk.

Deze resultaten suggereren dat de CN radicalen preferentieel kort aan of aan het substraatoppervlak gevormd worden. Het lijkt wel of er twee wegen bestaan die beide leiden tot het aanmaken van de CN radicaal. De CN radicalen worden in de bulk van het plasma en aan het substraatoppervlak aangemaakt. Deze hypothese werd bevestigd door een eenvoudig experiment.

De temperatuur van de waterstofatomen in het plasma verhoogt van 4750K ± 570K tot 5275K ± 630K. De temperatuurtoename gebeurt grotendeels op 4mm tot 6mm van het substraatoppervlak. De rotationele temperatuur van de C_2 moleculen vermindert van 4570K ± 460K tot 4230K ± 425K over hetzelfde interval. Het merendeel van de temperatuurvermindering gebeurt ook 4mm tot 6mm van het substraatoppervlak. Deze resultaten suggereren dat het toevoegen van stikstof verantwoordelijk is voor een thermalisatie van het plasma

Analyse van de diamantdeklagen

De groeisnelheid verhoogt met een factor 5 tot het toevoegen van 300ppm N_2. Boven een concentratie van 500ppm N_2 vermindert de groeisnelheid aanzienlijk.

De morfologie van de diamantdeklaag evolueert met de stikstoffractie in het gasmengsel. Zonder stikstof groeit de diamantdeklaag zonder voorkeursoriëntatie. Het toevoegen van 47.5ppm N_2 zorgt voor een toename in de grootte van de diamantkristallen en voor het begin van een voorkeursoriëntatie. De {111} facetten zijn wel gevormd.

Deze trend gaat door tot een stikstofconcentratie van 190ppm N_2. De <100> groeirichting staat loodrecht op de substraatoppervlakte. Met het toevoegen van een grotere stikstofconcentratie evolueert de diamantmorfologie naar een {100} textuur met een {100} voorkeursoriëntatie. Boven de 665ppm N_2 groeit de diamantdeklaag met de typische 'bloemkool' textuur.

De Raman kwaliteit van de diamantdeklaag vermindert op een exponentiële wijze met de toenemende stikstofverhouding in het plasma.

De SIMS metingen tonen aan dat de waterstof en stikstof verhoudingen in de diamantdeklagen toenemen met de stikstofconcentratie in het gasmengsel.

Mogelijk groeilooppad van diamantdeklagen met stikstoftoevoeging

De bovenverzamelde gegevens over het plasma en de diamantdeklaag worden gebruikt om een reeks plasma en oppervlakte chemische reacties voor te stellen die de groei van diamant onder deze procesvoorwaarden kan uitleggen.

Er wordt dieper nagekeken hoe de verschillende species in het plasma aangemaakt worden en hoe stikstof geïncorporeerd wordt in het diamant kristalrooster.

Conclusies

In het kader van dit doctoraatswerk hebben we kunnen bewijzen dat stikstof een duidelijke invloed heeft op de groei van CVD diamantdeklagen.

We hebben kunnen aantonen dat een eenvoudige meettechniek zoals Optische Emissie Spectroscopie, mits de nodige voorzorgen, gebruikt kan worden voor het bepalen van de relatieve concentratie van de plasma lichtemitterende species en hun toebehorende temperatuur. Door het gebruiken van een optische sonde hebben we de ruimtelijke verdeling en de temperatuur van verschillende species in het plasma kunnen vastleggen. Het lijkt wel dat stikstof verantwoordelijk is voor een thermalisatie van het plasma.

We hebben aangetoond dat stikstof, door het verhogen van de concentratie koolstofhoudende species in het plasma, verantwoordelijk is voor een verhoging van de groeisnelheid met een factor 5. De verhoging in de groeisnelheid gaat samen met een verandering in de morfologie, voorkeursoriëntatie en Raman kwaliteit van de diamantdeklaag. In lage concentratie bevordert stikstof de groei van {100} gestructureerde diamantdeklagen. De XRD textuurcoëfficiënten tonen aan dat de diamantdeklaag duidelijk evolueert naar een {100}-voorkeursoriëntatie. De SIMS waterstof en stikstof verhoudingen in de diamantdeklaag verhogen met de stikstofconcentratie in het proces gasmengsel.

Met de verzamelde gegevens hebben we niet kunnen bewijzen dat stikstof enkel en alleen maar in het diamant kristalrooster opgenomen wordt. Het is niet uit te sluiten dat stikstof grotendeels in de grafietachtige fase van de deklaag opgenomen wordt, aangezien de sp^2 verhouding en de stikstof verhouding in de diamantdeklaag tegelijkertijd toenemen.

De voorgestelde plasma en oppervlakte reactieschema's kunnen een deel van de opgemeten bevindingen verklaren, alhoewel er tot nu toe geen algemeen aanvaard groeischema bestaat voor het binaire methaan-waterstof gasmengsel.

1. Introduction

1.1 Man-made diamond

The extreme hardness, high thermal conductivity, excellent infrared transparency, and remarkable semiconductor properties (*Table 1*) combine to make diamond one of the most technologically and scientifically valuable materials found in nature [1-3]. However, natural diamond is rare and only available as gemstones in small sizes and at great expense. The scarcity and high cost have motivated researchers to attempt to duplicate nature and synthesise diamond since it was discovered in 1797 by Smithson Tennant that diamond is an allotrope of carbon.

Because of the hybrid sp, sp^2 and/or sp^3 carbon orbitals that are readily available for bonding, the solid carbon phase can exist under many different forms. Amongst the most widely known phases of crystalline carbon, we find diamond and graphite (Fig.1.1). Cubic diamond contains only sp^3 carbons, while the hexagonal graphite contains only sp^2 carbons. Lonsdaleite, which also contains only sp^3 carbons, is a rare but well-established carbon phase. Lonsdaleite is a natural mineral and is sometimes known as hexagonal diamond. The lonsdaleite and diamond crystal structures differ in the stacking sequence (Fig.1.1) and in the configuration of the C-C bond in the stacking direction of the different planes of carbon atoms (Fig.1.2). The slightly higher energy of these eclipsed lonsdaleite carbons causes its structure to be less stable than that of diamond.

At room temperature and atmospheric pressure, graphite is the stable crystalline form of carbon, with an enthalpy only ± 2 kJ mol^{-1} lower than diamond (*reaction 1*).

$$\text{Graphite} \Leftrightarrow \text{Diamond} : \pm 2 \text{ kJ mol}^{-1} \qquad (1)$$

Diamond is, relative to graphite, thermodynamically stable only at high pressures (> 10 GPa), as shown in the carbon phase diagram (Fig.1.3) [3-5]. The achievement of such pressures is, however, not a sufficient criterion for diamond formation from graphite since activation energy barriers inhibit spontaneous transitions. Therefore, the early attempts to convert graphite into diamond by simply increasing pressure were unsuccessful for over one hundred years until high pressure-high temperature (HPHT) processes came into being. The development of the HPHT processes is a result of the extensive research during the 1940's.

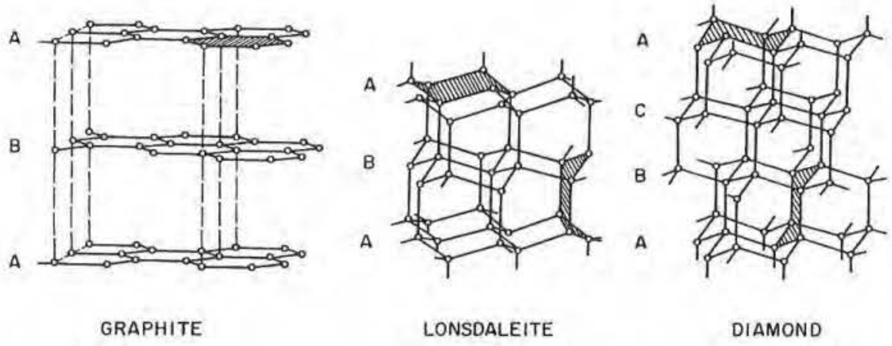

Figure 1.1: Schematic drawings showing the crystal structures of hexagonal graphite, hexagonal lonsdaleite and cubic diamond. Note the differences between the shaded hexagonal rings: planar for graphite, boat form for lonsdaleite and chair form for diamond [6].

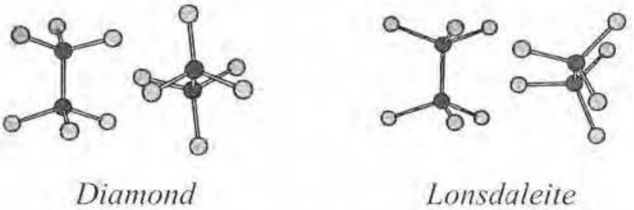

Figure 1.2: View down the C-C bond in stacking direction of planes shown in Fig.1.1. Diamond shows a staggered configuration of the next-nearest-neighbour C-C bonds, whereas lonsdaleite shows an eclipsed configuration [6].

Table 1.1: Properties of CVD diamond and single-crystal diamond [1].

Property	
Density	$3515\ kg/m^{-3}$
Thermal conductivity at 298 K	$2200\ W\ m^{-1}\ K^{-1}$
Thermal expansion coefficient at 298 K	$8\ 10^{-7}\ K^{-1}$
Scalar heat capacity (C_p=C_v)	$6{,}195\ J\ mol^{-1}\ K^{-1}$
Indirect band gap	5.45 eV
Electrical resistivity	$10^{14}\ \Omega\ m$
Relative dielectric constant at 300K	5,66
Maximum electron velocity	$2.7\ 10^5\ m\ s^{-1}$
Carrier mobility	
Electron (n)	$0{,}22\ m^2V^{-1}s^{-1}$
Positive hole (p)	$0{,}16\ m^2V^{-1}s^{-1}$
Compression strength	16.53 GPa
Vickers hardness	90 GPa
Index of refraction at 589,29nm	2.417

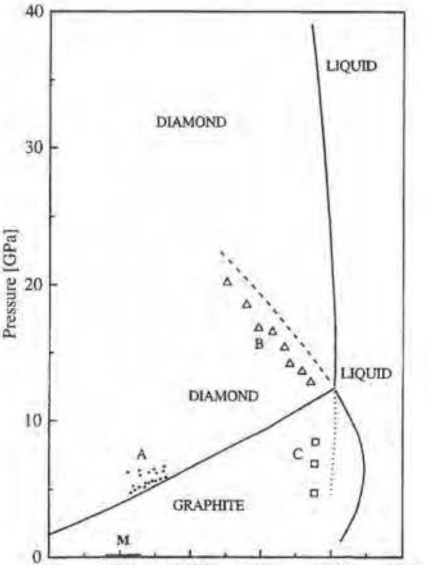

Figure 1.3: Carbon phase diagram with temperatures and pressure ranges corresponding to various diamond synthesis processes [3].

The HPHT synthesis of diamond essentially duplicates the natural process by converting graphite into diamond under conditions at which diamond is the thermodynamically favoured phase. Direct conversion of graphite to diamond in static HPHT processes requires high pressures (> 12 GPa) and high temperature (> 3000 K) to overcome the kinetic barrier and obtain any observable conversion rate, hence not economically viable. The difficulties in the direct conversion of graphite to diamond resulted in the development of new synthesis processes involving lower temperature and pressure. The major breakthrough in HPHT synthesis came when a solvent-catalyst reaction with a transition metal was used to surmount the kinetic barrier to diamond formation [7-9]. The solvent-catalytic HPHT process allows graphite to diamond conversion to occur at conditions much nearer the graphite-diamond equilibrium line but at lower temperatures (Fig.1.3). Typically, pressures range from 5 GPa to 10 GPa and temperatures from 1600 K to 2600 K. This technique, commercialised by General Electric in the U.S., along with the dynamic HPHT technique, i.e., shock-wave synthesis [10], industrialised by Du Pont in the U.S., provides a reproducibility and tailor ability unavailable in natural diamond in terms of chemistry, morphology, size, shape, toughness, and other properties for abrasive and heat-sink applications [11]. Synthetic diamond produced by HPHT methods is nowadays widely commercialised for use in industry. The development of the techniques also increases knowledge of the carbon phase diagram, which has advanced carbon research in general. Research in the HPHT synthesis of diamond is still underway in an effort to lower production costs.

Proceeding in parallel with the early studies of the HPHT diamond synthesis, different ways to synthesise diamond at low pressure were investigated. The most significant sustained effort at growing diamond at low pressures was that of W. G. Eversole of the Union Carbide Corporation in the U.S. [12].

By the end of 1952, predating the first successful HPHT synthesis, W. G. Eversole succeeded in synthesising diamond by Chemical Vapour Deposition (CVD) at low pressures and temperatures where diamond is metastable with respect to graphite (Fig.1.3). In the original report [12], diamond substrates were exposed to a hydrocarbon gas and then to hydrogen at high temperatures and low pressures. Under these conditions, the hydrocarbon was pyrolysised to form diamond and graphite and then hydrogen was used to etch away the graphite in a cyclic process (*reaction 2* and *reaction 3*).

$$CH_4 \xrightarrow{\text{Heat}} \text{Deposit (Diamond \& Graphite)} + 2\,H_2 \quad \mathbf{(2)}$$

$$H_2 + \text{Deposit} \xrightarrow{\text{Heat}} \text{Diamond} + CH_4 \quad \mathbf{(3)}$$

Contemporarily, B. V. Derjaguin *et al.* at the Institute of Physical Chemistry of the Academy of Science of the former U.S.S.R. [13] and J. C. Angus *et al.* at the Case Western Reserve University in the U.S. [14] initiated efforts to grow diamond at low pressures. Working independently from one another and unaware of Eversole's work, both groups were able to co-deposit diamond and graphite on diamond seed crystals. The depositions processes were inconvenient and required frequent interruptions to remove the accumulated graphite by hydrogen etching at temperatures and pressures greater than 1300 K and 5 GPa, or by oxidising in air at atmospheric pressure [13]. The growth rates of diamond under these conditions were less than 0.1 µm/h. In 1966, J. J. Lander and J. Morrison of the Bell Telephone Laboratories in the U.S. found that hydrogen could allow metastable grow of diamond by impeding the conversion of diamond to graphite at temperatures between 1150 K and 1600 K [15]. They pointed out that the growth of diamond on a single-crystal diamond substrate is possible as long as carbon atoms are added at a rate low enough to prevent stable graphite from forming. Although the average growth rates at the time were too low to be of commercial significance.

The role of hydrogen in the growth process was a major focus of the research. This was strongly motivated by the early results (Lander and Morrison) and by general chemical considerations that led to the conclusion that a hydrogen-rich environment should suppress the nucleation and growth of graphite deposits. The sustained efforts of Derjaguin, Angus and their co-workers showed the crucial role played by atomic hydrogen in the diamond growth process (Fig.1.4).

This discovery was a historic milestone in the development of diamond CVD techniques and led by the mid 1970's to the growth of diamond crystals on non-diamond substrate at a commercially practical deposition rate (> 1 µm/h) (*reaction 4*).

$$CH_4 \xrightarrow{\text{Heat \& Atomic hydrogen}} \text{Diamond} + 2\,H_2 \quad (4)$$

The first published descriptions of methods for rapid growth of diamond at low pressure were made by a group of Japanese researchers associated with the National Institute for Research in Inorganic Materials (NIRIM). Successful diamond synthesis was first achieved in 1981 by Matsumoto and Setaka using a hot filament to activate CH_4/H_2 gas mixtures. Shortly thereafter the NIRIM research group reported that diamond films could be grown on various substrates using a mixture of methane diluted in hydrogen at subatmospheric pressures by RF as well as by microwave plasma assisted CVD systems.

These results -that were supported by the first convincing diamond characterisation by electron microscopy, X-ray diffraction and Raman spectroscopy- confirmed the earlier experiments and refocused world-wide attention on the synthesis of diamond by CVD.

A single method of producing diamond thin films which is adequate for all of the proposed applications of diamond thin film technology has not emerged yet. The key task is to identify the deposition method that will produce a diamond-containing product possessing the greatest performance/cost ratio. It is therefore increasingly obvious that further technological developments in CVD of diamond films require a detailed understanding and control of the fundamental phenomena associated with diamond nucleation and growth. These phenomena, especially the nucleation and early growth stages, critically determine film properties (morphology, homogeneity, defect formation, adhesion, etc...) and the type of substrates that can be successfully coated.

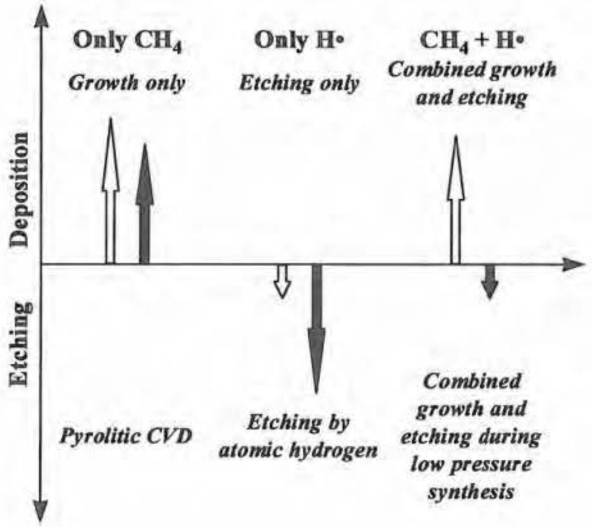

Figure 1.4: Relative etching and deposition rates of diamond (white arrows) and graphite (black arrows) [16].

In the past decade, a wide variety of energetically assisted CVD processes have evolved for diamond synthesis, allowing depositing diamond onto large areas (400cm^2 [3]) on a wide variety of substrate materials and shapes. Linear growth rates have been increased to the order of hundreds of micrometers per hour [17-20], high enough to be nowadays of commercial significance. The various existing CVD methods, although different in their process details, can be divided into four major categories according to the specific method of initiating the chemical reactions that lead to diamond formation (*Table 1.2*).

Diamond of similar quality and morphology has been grown using a variety of species, including aliphatic and aromatic hydrocarbons, ketones, amines, ethers, alcohols, carbon monoxide and dioxide and halogen (CCl_4, CF_4). Methane largely diluted into hydrogen is the most frequently used feed gas mixture.

Fig.1.5 provides a common scheme for all major CVD methods used to date. It can be seen that the gas compositions suitable for diamond depositions are restricted to a well defined area within the diagram, independent of the deposition methods or carbon species used.

Table 1.2: Routes for the CVD synthesis of diamond.

Thermal CVD
Thermal decomposition
Chemical transport reaction
Hot filament technique
Oxyacetylene torch
Halogen-assisted CVD
DC plasma CVD
Low pressure DC plasma
Medium pressure DC plasma
Hollow cathode discharge
DC arc plasmas and plasma jets
RF plasma CVD
Low pressure RF glow discharge
Thermal RF plasma
Microwave plasma CVD
915 MHz plasma
Low pressure 2.45 GHz plasma
Atmospheric pressure 2.45 GHz plasma torch
2.45 GHz magnetised (ECR) plasma
8.2 GHz plasma

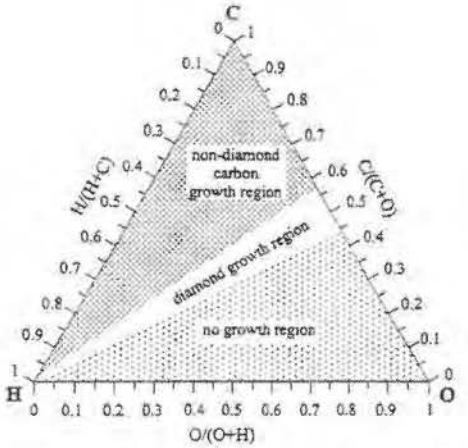

Figure 1.5: Atomic C-H-O diamond deposition phase diagram, showing the gas compositions suitable for diamond growth [20].

1.2 Plasma diagnostic techniques

The techniques used for understanding the gas composition in diamond CVD can be divided into 3 types: sample extraction, physical probes and optical probes. The sample extraction methods use *ex situ* analysis of an extracted portion of the gas. The most common sample extraction methods used in diamond CVD are gas chromatography (GS), mass spectrometry (MS) and matrix isolation Fourier transform infrared spectroscopy (MI-FTIR). The primary advantage of these techniques is the ability to monitor many species simultaneously. Absolute concentrations of compounds can be used through the use of standards to calibrate the response of the instrument. To monitor the chemically relevant gas in the vicinity of the growth surface, a probe must be inserted to extract the reaction gases. The necessity of introducing a probe into the reactive gas mixture is a significant disadvantage of the sampling techniques. The probe causes changes in gas velocity, composition, temperature and pressure in a region extending several probe diameters around the sampling region. Physical probe methods introduce a probe (Langmuir, thermocouple) into the reaction chamber. Because of the use of a probe, physical methods perturb the gas environment being studied too.

Optical diagnostic techniques, which use photons to transmit the information from the plasma to the detection medium, are the least intrusive *in situ* plasma diagnostic methods. The photon-based diagnostics include the often-used emission spectroscopy, absorption spectroscopy, and laser induced fluorescence (LIF), but also Raman scattering, coherent anti-Stokes Raman spectroscopy (CARS), optogalvanic effects, laser interferometry, and ellipsometry.

Optical Emission Spectroscopy (OES), which is the spectral analysis of the light emanating from a plasma, is probably the most widely used method for monitoring and diagnosis of plasma processes. By measuring the wavelengths and intensities of the emitted spectral lines, one can identify the neutral particles and ions present in the plasma. The method is implemented both in research laboratories and in manufacturing for production control.

The spectral fingerprint of the optical plasma emission provides information about the chemical and physical processes that occur in the plasma. This technique has the advantage of being external to the reactor and vacuum system and provides besides spatial and temporal resolution also high reliability. However, the OES technique is limited to the monitoring of light-emitting species, and the emission intensity is not always directly related to the concentration of the species in the plasma.

1.3 Modelling reactor scale processes

Numerical and analytical solutions of the continuum equations governing the conservation of momentum (fluid flow), mass, and energy (temperature) have led to many insights into the mechanisms and conditions under which diamond may be grown by CVD. Modelling many types of diamond reactors has proven successful primarily because the main hydrocarbon sources used are CH_4 and C_2H_2, and the pyrolysis and combustion mechanisms for these fuels are well understood for the stoichiometries used [21-25]. Thermodynamic and thermophysical data for the various gaseous species are known.

The reactor configurations and operating conditions used in direct current (DC) arc-jet, radio frequency (RF) plasma, combustion, and hot-filament systems often lend themselves to geometric simplifications that, in turn, make the numerical models tractable, even with detailed homogeneous end heterogeneous chemistry. One-dimensional models of these reactors have proven successful in describing qualitative (e.g. diamond growth rate) features in systems where charged species (plasma) chemistry does not play a significant role [26-31].

More detailed modelling that captures multidimensional effects and ion-neutral chemistry is still required in order to adequately describe systems containing non-thermal plasmas (e.g. microwave reactors).

Because of the difficulties that are involved in modelling non-thermal plasma systems, fewer theoretical studies have been performed on microwave reactors [32].

A driving force for the development of more complex reactor models is the knowledge that the properties of diamond films and their microstructure are integrally related. By definition, the continuum-reactor models cannot address crucial issues such as morphological evolution, defect formation, and grain growth. The continuum models provide one-dimensional predictions of the growth rate, but are incapable of directly incorporating microscopic information into the model or predicting any quantities that are microstructure dependent.

1.3.1 Simulating growth on atomic scale

The prediction of atomic and structural information and the self-consistent calculation of the properties of different film orientations can be accomplished by combining the surface reaction chemistry used in conventional growth models with a realistic three-dimensional atomic representation of the film. This approach has been adopted in two recent studies [33-34], but only to predict growth rates and morphologies of individual surface orientations. The self-consistent comparative study of diamond growth on different surface orientations is only now being explored. In contrast to a reactor-scale model, atomic-scale models are able to predict the growth velocities for surfaces of any orientation, vacancies incorporation, and surface reconstruction. Such models require detailed knowledge of the flow field, temperature, and composition in the gas adjacent to the deposition surface. Thus, there is a tight coupling between the reactor-scale models and the atomic-scale models. For a given set of operating conditions, the reactor-scale models may be used to produce a two-dimensional map of gas-phase conditions at the deposition surface. The atomic-scale models, in turn, use these conditions to accurately predict microscopic growth information, such as the growth rate that may be passed back to the continuum models or forward to the microstructural models.

1.3.2. Modelling of diamond CVD growth process

Generally accepted chemical mechanisms that lead to low pressure growth of diamond are still lacking. Since the atomic processes involved in diamond growth cannot be observed *in situ*, much of our understanding is extracted from the modelling and simulation or inferred from experimental observations. While calculations of surface states energies can provide the kinetics of individual reaction events, these techniques are not suited to the time and length scales required to study diamond film growth. One-dimensional growth models, elaborated mainly by Badzian *et al.* [35], Frenklach *et al.* [36, 37], Dandy *et al.* [26, 38] and Harris *et al.* [39, 40], have been useful for verifying proposed growth mechanisms. However, these models typically consider the kinetics of only one diamond growth mechanism, and do not explicitly account for competing mechanisms or the effect of surface atomic structure and morphology on growth behaviour. Three-dimensional atomic-scale simulations of diamond growth have been performed recently by Dawnkaski *et al.* [33], but were limited to growth at particular surface configurations on the {100} diamond surface.

Lately, Battaile *et al.* [41] introduced a more realistic three-dimensional simulation method based on a rigid three-dimensional lattice capable of simulating hours of growth under most CVD conditions and on virtually any surface [26, 40].

1.4 CVD diamond processing

CVD processes offer an opportunity to exploit some of the outstanding physical properties of diamond (*Table 1.1*). The ability to coat large areas on a variety of substrate materials with diamond films vastly expands the potential application areas of CVD diamond over those possible with natural or HPHT diamond (*Table 1.3*).

The substrate temperature and composition of the process gas mixture are clearly the most important factors governing the film texture and surface morphology. CVD diamond exhibits mostly {100} and {111} facets [42, 43]. Thus, isolated freely growing crystals are cubo-octahedral in shape and are bounded {100} and/or {111} faces. The crystal shape and, thus, the densities of both types of surface orientations bounding the crystal are controlled by the relative rates of growth of the two surface orientations. This information is commonly expressed by the following growth rate parameter introduced by Wild *et al.* [44]:

$$\alpha = \frac{V_{100}}{V_{111}}\sqrt{3}$$

where V_{hkl} is the growth rate of the $\{hkl\}$ facet. This dependence of crystal shape on α is shown in Fig.1.6.

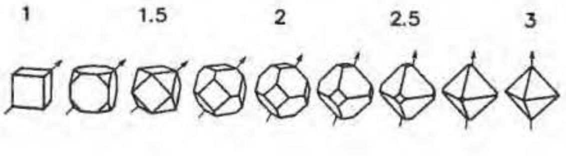

Figure 1.6: Idiomorphic crystal shapes for different values of the growth parameter α. The arrows indicate the direction of fastest growth [44].

Low values of α (≤ 1) yield cubic crystals with {100} faces, high values (≥ 3) produce octahedral crystals with {111} faces, and intermediate values lead to cubo-octahedral crystals bounded by both surface orientations. When a continuous polycrystalline diamond film is formed by the coalescence of multiple single crystal nuclei, the microstructural properties of the film (morphology, texture, grain size, etc.) are determined by this growth-rate parameter. The rates of growth of the different facets and the orientations of the nuclei determine which grains will survive when the film thickens (i.e. the crystallographic texture) and which facet orientation will be represented on the surface (i.e. the surface morphology). In other words, the polycrystalline diamond growth can be explained by the Van der Drift model [45], which states that crystals with the fastest growth rate in the vertical direction will survive and overgrow adjacent crystals.

Fig.1.7 shows the dependence of τ_{100}, the tilt angle of <100> directions with respect to the substrate normal ($\cos(\tau_{100}) = \frac{1}{|\upsilon|}$, where υ is the direction of fastest growth), on the methane concentration for different deposition temperatures [44]. In general, a temperature increase leads to an increase in τ_{100} and thus to a decrease in α.

The variation and control of film texture are also achievable by adding oxygen [46-53] or nitrogen-containing species to the gas mixture.

The addition of small amounts of nitrogen (ppm range) [54-67] leads to a transition of the film surface morphology from nanocrystalline to large, coplanar {100} facets with concomitant change of the crystal structure from a <110> to a <100> texture and a significant improvement of the crystalline quality. The growth experiments were performed with microwave plasma assisted CVD [55, 56] at low microwave power levels of several hundred of watts. A slight enhancement of the growth rate has been reported under these conditions [56]. On the other hand, a drastic increase of the growth rate has been observed with some 10ppm nitrogen added to the process gas mixture at multi-kW power levels [52].

Nitrogen addition is not only interesting for textured diamond growth. It can also be incorporated as a single substitutional species in the same manner as for high-temperature high-pressure synthetic Ib diamond

and change the electronic properties of the diamond film. This nitrogen centre is a deep donor with an ionisation energy of about 2 eV [68].

Table 1.3: Actual and potential applications of CVD diamond [4].

Application area	*Application examples*	*Physical properties of diamond used in the applications*
Grinding/cutting tools	Inserts Twist drills Whetstones Industrial knives Circuit-board drills Slitter blades Surgical scalpels Saws	great hardness great wear resistance high strength and rigidity good lubricating properties general chemical inertness
Wear parts	Bearings Jet-nozzle coatings Slurry valves Extrusion dies Abrasive pump seals Computer disk coatings Engine parts Mechanical implants Ball bearings Drawing dies Textile machinery	great hardness great wear resistance high strength and rigidity good lubricating properties general chemical inertness
Acoustical coatings	Speaker diaphragms	high sound propagation speed high stiffness low weight
Diffusion/corrosion protection	Crucibles Ion barriers (sodium) Fibre coatings Reaction vessels	general chemical inertness high strength and rigidity good temperature resistance
Optical coatings	Laser protection Fibre optics X-ray windows Anti reflection UV to IR windows Radomes	transparency from UV through visible into IR good radiation resistance
Photonic devices	Radiation detectors Switches	large bandgap
Thermal management	Heat-sink diodes Heat-sink PC boards Thermal printers Target heat-sinks	high thermal conductivity high electrical resistivity
Semiconductor devices	High-power transistors High-power microwave Photovoltaic elements Resistors Capacitors Field-effect transistors UV sensors Integrated circuits	high dielectric strength high thermal conductivity good temperature resistance good radiation resistance high power capacity good high-frequency performance low saturation resistance

The incorporation of substitutional nitrogen in diamond causes large lattice dilatation, since the effective volume occupied by substitutional nitrogen in diamond is approximately 40% larger than that of carbon [67, 70]. A high substitutional nitrogen incorporation in the diamond lattice therefore leads to a lot of lattice dilatation sites and even to non-diamond sp^2 carbon defects [60].

If we know how to improve empirically the diamond film quality by adjusting the process parameters, we are still unable to picture exactly the growth mechanisms involved.

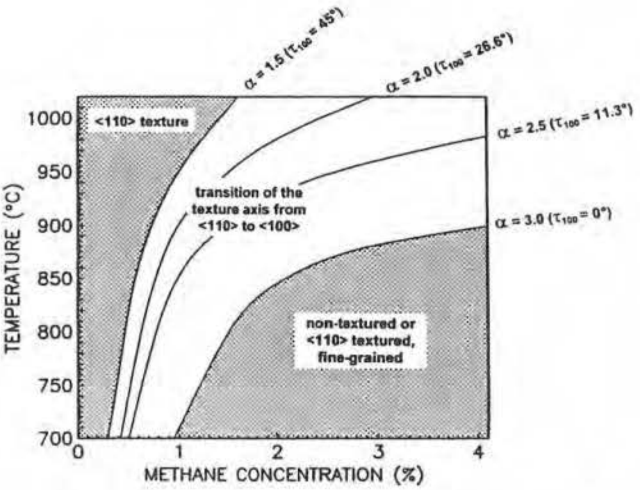

Figure 1.7: Dependence of the film texture and morphology on CH_4 concentration and substrate temperature [44]. The parameter τ_{100} is the tilt angle of <100> directions with respect to the substrate normal.

1.5 Objectives of this work

The purpose of this work is to tackle the influence of minute nitrogen addition (ppm range) on the growth of diamond films by microwave plasma-assisted Chemical Vapour Deposition.

To study the composition and chemistry of the plasma, we chose for Optical Emission Spectroscopy (OES). This technique is based on the identification of light emitting species, which is also the main drawback of the technique, as only light emitting species in the plasma can be identified, but, on the other hand, OES has the main advantage of being non-intrusive and easy to implement. Used as is, OES has little interest, as the only information that one can get from the spectra is a partial qualitative analysis of the plasma. But, as the literature shows, this technique can also be used for semi-quantitative analysis (actinometry) and to determine the temperature of the observed plasma species. With the proper optic set-up, it can be also used to determine the relative concentrations of the various light emitting species as a function of the distance from a reference point, in our case, the substrate surface. Taking into account the physical constraints of our deposition set-up, we built a specific optical probe to reduce the volume captured by the probe, allowing therefore to sample the plasma over much smaller volumes.

In this work, the relative concentration of atomic hydrogen was monitored as a function of the nitrogen flow injected into the system. Electron and vibrational temperatures of some emitting plasma species were calculated from the emission spectra by the Boltzmann plot technique.

Variations in the electronic and vibrational temperatures were observed not only as a function of the nitrogen content in the gas phase but as a function of the distance from the substrate surface too. By using this technique, we were able to see where the different plasma species originated.

To propose a growth model based on the experimental observations, we had to perceive how nitrogen could intervene in the surface chemistry too. We therefore investigated the effect of nitrogen addition on the properties of the deposited diamond films. Differences in morphology were studied by Scanning Electron Microscopy (SEM), while the preferred orientations of the diamond film were calculated from X-Ray Diffraction (XRD) spectra. The film quality, or the relative sp^2/sp^3 ratio in the film, was determined by micro-Raman Spectroscopy. Variations in the chemical composition of the deposited film are presented as a function of the nitrogen fraction in the feed gas using Secondary Ion Mass Spectroscopy (SIMS).

The various film characteristics are correlated to the OES observations of the plasma.

Combining all gained informations, we propose a simplified growth model, which tries to account for possible plasma and surface chemical reactions involved under these specific growth conditions with nitrogen addition.

2. Fundamentals of plasma

2.1 Plasma parameters

Low-pressure plasma, cold plasma, non-equilibrium plasma and glow discharges are some of the synonymously used terms to designate the same type of process. The technologies using these plasma-assisted processes are generally referred to as plasma assisted Chemical Vapour Deposition (PA CVD), ionitriding, plasma etching, etc.

At the base of the mentioned technologies is the cold plasma, a phenomenon similar to that occurring in fluorescent bulbs or neon lights, that is, an electrical discharge in a gas at low pressure. The phenomena occurring in cold plasmas are very complex and still not fully understood. However, it is possible with the present knowledge of plasma physics and chemistry to adjust and control the composition of the gas mixtures and the parameters of the discharge to achieve the required results in terms of processing and materials properties. The plasma assisted techniques allow increased production rates, precise production, and devising of materials with unique properties which evolve from the chemistry of cold plasmas. Taking into consideration the energy of the particles constituting it, the plasma is energetically the fourth state of the matter, apart from the solid, liquid and gas states (Fig.2.1).

A plasma can be defined as a quasi-neutral gas of charged and neutral particles characterised by a collective behaviour.

Let us define the collective property of the plasma. The behaviour of a neutral gas is described by the kinetic theory of gases. According to this theory, in an ordinary neutral gas no forces act between the molecules of the gas (gravitational forces are considered negligible), and the particles travel in straight lines, with a distribution of velocities. The motion of the molecules is controlled by the collision among themselves and with the walls of the container. As a result of these collisions, the molecules of a neutral gas follow a random Brownian motion, as illustrated in Fig.2.2(a).

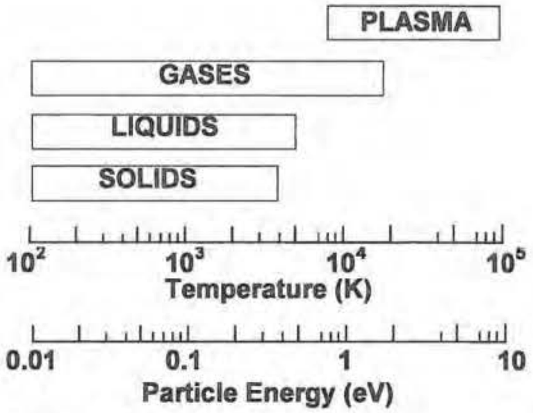

Figure 2.1: State of the matter versus temperature [71]

Assuming the particles of the neutral gas to be rigid spheres of radius r and their density n, the kinetic theory of gases defines the cross section for collision, σ, and mean free path, λ, as

$$\sigma = \pi r^2$$

$$\lambda = \frac{1}{\sigma n}$$

The average number of collisions per second, called the collision frequency, ν, and the mean time between collisions, τ, are given by

$$\nu = \frac{\bar{\upsilon}}{\lambda}$$

$$\tau = \frac{1}{\nu} = \frac{\lambda}{\bar{\upsilon}}$$

where $\bar{\upsilon}$ is the average velocity of the molecules in the gas which is determined by its temperature T:

$$\bar{\upsilon} = \sqrt{\frac{3kT}{M}} \qquad (Eq.2.1)$$

where M is the mass of the molecule, and k is the Boltzmann constant [71].

If the temperature of the gas is constant, the collisional mean free path is inversely proportional the pressure in the system:

$$\lambda = \frac{C}{p}$$

where C is a constant depending on the gas and p is the gas pressure [71].

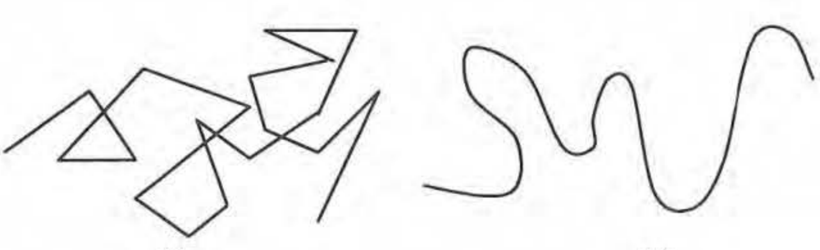
(a) (b)

Figure 2.2: Particle path in a neutral gas and under collective behaviour in a plasma: (a) Brownian motion of a neutral gas molecule; (b) motion of a charged particle in a plasma [71].

In a plasma, contrary to the preceding description, the motion of the particles can cause local concentrations of positive and negative electric charges. These charge concentrations create long-range Coulombic fields that affect the motion of charged particles far away from the charge concentrations. Thus elements of the plasma affect each other, even at large distances, giving the plasma its characteristic collective behaviour. A charged particle in a plasma moves along a path, which on average follows the electric field. Such a path is illustrated in Fig.2.2(b). In some conditions, at low pressures, the effect of the long-range electromagnetic forces on the motion of the particles can be much stronger than the effect of the collisions between the particles. In such cases, the plasma is called a collisionless plasma.

A plasma, especially one sustained in a mixture of molecular gases, contains a multitude of different neutral and charged particles. A group of identical particles in a plasma is commonly referred to as a species.

The plasma is broadly characterised by the following basic parameters:

- the density of the neutral particles, n_n.
- the densities of the electrons and ions n_e and n_i. In the quasi-neutral state of plasma the densities of the electrons and of the ions are usually equal, $n_i=n_e=n$ and n is called the plasma density.
- the energy distributions of the neutral particles, $f_n(W)$, ions, $f_i(W)$, and electrons, $f_e(W)$.

The plasma density is an important parameter in plasma processing because the efficiency of the processes occurring in the plasma and their reaction rates are generally dependent directly on the density of the charged particles. Being electrically charged, both electrons and ions interact with the applied external electric field and are accelerated by absorbing energy from it. Because the electrons are the lightest particles in the plasma, they are easiest accelerated and absorb the largest amount of energy from the external field. The electrons then transfer through collisions energy to the molecules of the gas and cause their excitation, ionisation and dissociation. The effectiveness of these processes increases with increasing electron density. Ions, too, play a significant role in the chemical reactions taking place in the plasma. Many of the reactions occurring in a plasma are controlled, or affected, by ion chemistry. It is therefore important to achieve high ion densities to increase the rates of reactions involving the ions.

As in any gaseous system, particles in the plasma are in continuous motion, inducing collisions between them. The collisions, which take place between the particles in the plasma, are of two types, elastic or inelastic. Collisions between electrons and heavy targets (i.e. neutral or charged particles) that do not result in an excitation of the target are called elastic collisions, whereas those collisions that leave the target in an excited state are called inelastic collisions.

The energy transfer W_{Tr} in an elastic collision between an electron and a heavy target is determined by the mass ratio of the particles

$$W_{Tr} = \frac{2m_e}{M} W$$

where M represents the mass of the heavy particle, W, the energy of the electron and m_e, the mass of the electron [71].

The fraction of transferred energy in an elastic collision of an electron with a heavy target is therefore very small. On the other hand, a significant amount of energy is transferred in a collision between two electrons.

The electrons gain energy through acceleration by the electric field, which sustains the plasma and transfers that energy by inelastic collisions with the neutral gas molecules. The inelastic collisions between energetic electrons and the heavy species of the plasma result in excitation, ionisation, or dissociation of the target if it is multiatomic. Energy transfer in an inelastic collision is not controlled by the mass ratio of the colliding particles. In an inelastic collision between two particles, the fraction of transferred energy is given by

$$\frac{W_{Tr}}{W} = \frac{M}{m_{in} + M}$$

where m_{in} is the mass of the particle losing energy [71].

According to the above equation, in an inelastic collision between an electron and a heavy particle ($m_{in} = m_e << M$), the electron can transfer almost all its energy to the heavy particle, creating an energetic plasma species. The inelastic collisions therefore sustain the plasma by producing the particles that form it and giving the plasma its special features. Inelastic collisions involve energy transfer in amounts that vary from less than 0.1 eV (for rotational excitation of molecules) to more than 10 eV (for ionisation) [71].

Electron-electron collisions can also play a significant role in the energy transfer processes. Their importance depends on the degree of ionisation prevalent in the plasma.

For degrees of ionisation below 10^{-10}, the contribution of the electron-electron collisions to the energy transfer is negligible [21, 71].

The parameter that defines the density of the charged particles in the plasma is the degree of ionisation of the gas. It specifies the fraction of the particles in the gaseous phase, which are ionised. The degree of ionisation, α, is defined as

$$\alpha = \frac{n_i}{n}. \qquad \textit{(Eq.2.2)}$$

For plasmas sustained in low-pressure discharges, the degree of ionisation is typically 10^{-6} to 10^{-3} [21]. However, if the electrical discharge is assisted and confined by an additional magnetic field, the degree of ionisation can reach values of 10^{-2} or higher. The degree of ionisation in a plasma is a function of the elements contained in the plasma.

One of the physical parameters defining the state of a neutral gas in thermodynamic equilibrium is its temperature, which represents the mean translational energy of the molecules in the system. A plasma contains a mixture of particles with different electric charges and masses. At a first approximation, the plasma may be considered, thermally, as consisting of two systems: the first containing only electrons and the second containing heavy species, that is, neutral atoms or molecules, ions, and neutral molecular fragments.

The electrons gain energy from the electric field, which energises the plasma, and lose part of it by transfer to the second system through elastic or inelastic collisions. The system of heavy particles loses energy to the surroundings, either by radiation or by heat transfer to the walls of the vessel containing the plasma.

The electrons and the heavy species in the plasma can be considered approximately as two subsystems, each in its own thermal quasi-equilibrium.

The ions and electrons in the plasma can therefore be characterised by their specific different average temperatures: the ion temperature, T_i, and the electron temperature, T_e. The situation is much more complicated for the heavy species in the plasma. The heavy species can be characterised by several temperatures at the same time: the temperature of the gas, T_g, which characterises the translational energy of the gas; the excitation temperature, T_{ex}, which characterises the energy of the excited particles in the plasma; the ionisation temperature, T_{ion}; the dissociation temperature, T_d, which characterises the energy of ionisation and dissociation; and the radiation temperature, T_r, which characterises the radiation energy. Thermodynamic equilibrium will exist in the plasma only if the following equation is satisfied:

$$T_g = T_{ex} = T_{ion} = T_d = T_r = T_e.$$

Complete thermodynamic equilibrium cannot be achieved in the entire plasma because the radiation temperature, T_r, at the envelope of the plasma cannot equal the temperature in the plasma bulk. However, under certain experimental conditions, it is possible to achieve local thermodynamic equilibrium in a plasma in volumes of order of the mean free path length. If this happens, the plasma is called a local thermodynamic equilibrium (LTE) plasma. In low-pressure plasmas, produced by direct current glow discharge, radio frequency excitation, the LTE conditions are generally not achieved.

In non-LTE plasmas, the temperatures of the heavy particles are normally too small to promote chemical reactions in thermodynamic equilibrium. The electron temperature is therefore the most important temperature in non-LTE plasmas. The temperature and thermodynamic equilibrium aspects are discussed in further detail in the following chapter.

If an electrical field is created in the plasma, the charged particles will react to reduce the effect of the field. The lighter, more mobile, electrons will respond fastest to reduce the electric field and the electrons will move to cancel the charge. The response of charged particles to reduce the effect of local electric fields is called the Debye shielding and the shielding gives the plasma its quasi-neutrality characteristic. Let assume that an electric potential is applied between two surfaces immersed in a plasma. The surfaces will attract equal amounts of charged particles of opposite sign. The concentration of charged particles near the two surfaces will shield the charged surface from the plasma bulk, which will remain neutral. The applied electrical potential will therefore develop mostly near the surfaces, over a distance λ_D, called the Debye length, and defined by:

$$\lambda_D = \left(\frac{\varepsilon_0 k T_e}{n_e e^2} \right)^{1/2}$$

where ε_0 is the permittivity of the free space and e, the charge of the electron [71].

The Debye length decreases with increasing electron density. An ionized gas is considered a plasma only if the density of the charged particles is large enough such that $\lambda_D << L$, where L is the dimension of the system. If this condition is satisfied, local concentrations of electric charges which may occur in the plasma are shielded out by the Debye shielding effect over distances smaller than the Debye length. Outside these volumes of charge concentrations the plasma bulk is quasi-neutral. The Debye length, λ_D, is therefore the characteristic dimension of regions in which breakdown of neutrality can occur in a plasma. Typical values found in a cold plasma are $T_e = 1$ eV, $n_e = 10^{10}$ cm^{-3} and $\lambda_D = 74$ μm [71].

Another plasma parameter related to the Debye length is the number of particles N_D, in a Debye sphere, that is, in a sphere of radius equal to λ_D. Assuming that the shielding effect is produced by a large number of electrons, or in other words, that the shielding is caused by electrons in the Debye sphere, N_D is related to the Debye length by the relation:

$$N_D = \frac{4\pi}{3} n_e \lambda_D^3 = \frac{1.38 \times 10^3 T_e^{3/2}(K)}{n_e^{1/2}} = \frac{1.718 \times 10^9 T_e^{3/2}(eV)}{n_e^{1/2}}.$$

N_D has to be therefore much larger than the unity to fulfil the collective characteristic of the plasma [71]. For electrons temperatures $T_e > 1$ eV and densities $n_e < 10^{12}$ cm^{-3}, the condition $N_D >> 1$ is easily satisfied. In cold plasmas, N_D ranges from about 10^4 to 10^7 electrons in a Debye sphere.

Ions and electrons reaching a solid surface recombine and are lost from the plasma system. Electrons have much higher thermal velocities than ions reach the surface faster and leave the plasma with a positive charge in the vicinity of the surface. An electric field that retards the electrons and accelerates the ions develops near the surface in such way as to make the net current zero. As a result, the surface achieves it at a negative self-bias relative to the plasma. The plasma is therefore always at a positive potential relative to any surface in contact with it. Because of the Debye shielding effect, the potential developed between the surface and the plasma bulk is confined to a layer of thickness of several Debye lengths. This layer of positive space charge that exists around all surfaces in contact with the plasma is called the plasma sheath.

The sheath potential, V_s, is the electrical potential developed across the plasma sheath. Only electrons having sufficiently high thermal energy will penetrate the sheath and reach the surface, which, being negative relative to the plasma, tends to repel the electrons. The value of the sheath potential adjusts itself in such way that the flux of these electrons is equal to the flux of ions reaching the surface. The thickness of the plasma sheath, d_s, is defined as the thickness of the region where the electron density is negligible and where the potential drop V_s occurs. As explained previously, the thickness of the plasma sheath is related to the Debye length. It also depends on the collisional mean free path in the plasma and is affected by external biases applied to the surface.

At higher pressures, when the collisional mean free path is of the same order of magnitude as the thickness of the plasma sheath, the latter can be estimated from [72]:

$$d_s \approx \eta^{2/3} \times \lambda_D$$

with

$$\eta = \frac{e(V_p - V_B)}{kT_e}$$

where d_s is the thickness of the plasma sheath, V_B, the bias on the considered surface (self or external bias), and V_p, the plasma potential.

It was experimentally found that the thickness of the plasma sheath is affected by more parameters than these figuring in the above equation. The relation between the thickness of the plasma sheath and those additional parameters is still not clearly understood. The thickness of the plasma sheath was found to be also dependent on the frequency of the electromagnetic field and the pressure in the system.

2.2 Microwave plasmas

Microwave plasmas are sustained by power supplies operating at a frequency ω of 2.45 GHz. This frequency, which is commonly used for industrial or home heating applications, makes suitable power supplies readily available. The excitation of the plasma by microwaves is similar to the excitation with RF, while differences result from the range of frequencies. In typical microwave plasmas the strength of the electric field is about $E_0 \approx 30$ V/cm.

The power absorption by the MW discharge can be either collisional or collisionless. In a collisionless situation, an electron would oscillate in the MW field and would reach maximal velocity x', amplitude x and energy W, given by [73]

$$x' = \frac{eE_0}{m_e \omega}$$

$$x = \frac{eE_0}{m_e \omega^2}$$

$$W = \frac{m_e x'^2}{2}$$

where E_0 is the amplitude of the electric field. In a collisionless situation, the maximum amplitude of the electron at microwave frequencies is $x < 10^{-3}$ cm, and the corresponding maximum energy acquired by an electron during one cycle is about 0.03 eV. This energy is far too small to sustain a plasma. Therefore microwave discharges are more difficult to sustain at low pressures (< 14 Pa) than DC or RF discharges.

In a collisional discharge, at constant electric field and power density, the average MW power transferred from the outside electric field to the unit volume of gas, $\overline{P_v}$, is

$$\overline{P_v} = \frac{n_e e^2 E_0^2}{2m_e}\left(\frac{m}{v^2 + \omega^2}\right)$$

where v is the collision frequency [71]. The absorption of microwave power is thus a function of the collision frequency of the electrons with the heavy species and is therefore dependent on the pressure in the discharge.

Microwave plasmas have their greatest glow intensity at the coupling microwave cavity and diminishes rapidly outside it because of the small wavelength of microwaves ($\lambda = 12.24$ cm for a frequency of 2.45 GHz). In a microwave plasma, the magnitude of the electric field can vary within the reactor, which has dimensions of the same order of magnitude as the wavelength. One can thus find active species from the discharge still persisting into a region free of the glow of the plasma that is in the afterglow.

The maximum of the electron density (n_e) far from the walls, along the axis of the reactor, should not exceed much more than the one corresponding to the oscillation frequency, that is 10^{11} cm^{-3}, in the case of microwave plasmas operating at 2.45 GHz. Above this limit, also called the cut off frequency, the incident microwave would not penetrate efficiently the plasma [74]. For very high electron density, incident waves might even be reflected back by the plasma. In the case of a 2.45 GHz microwave plasma used in diamond deposition, 10^{12} cm^{-3} is considered as the upper limit for the electron density [71].

2.3 Chemical processes in a plasma

The chemical processes in the plasma follow several steps: initiation, propagation, termination, and reinitiation [75, 76].

In the initiation stage free radicals or atoms are produced by collision of energetic electrons or ions with molecules. The radical formation takes place by dissociation of molecules in the gaseous phase or of molecules adsorbed on the surface of the substrate or on the deposited film. Both molecules and radicals are adsorbed on the surfaces exposed to the plasma.

The propagation step of the reactions can also take place in both the gas and on the modified surface (deposited film, etched surface). In the gas phase, propagation involves the interaction between radicals, ions, and molecules in ion-molecule and radical molecule reactions. Propagation takes place on the solid surface through interactions of surface free radicals with the gas phase or adsorbed molecules, radicals, or ions.

In the termination step, reactions similar to those described for propagation result in the formation of the final product.

Reinitiation develops when radicals, which are formed through the conversion of the deposited film, again enter the reaction chain. The conversion to the radicals can be caused by impact of energetic particles or by photon absorption.

During CVD processing it is important to prevent the termination of the main reaction chain in the homogeneous gas phase. If not prevented, these homogeneous reactions will affect the film deposition rate and the quality of the deposited films.

Due to the magnitude of the phenomena affecting the plasma and the resulting complexity of the plasma chemistry, it is not always possible to control the pathways of the chemical reactions or to predict from the first principles the right combination of processes required for a certain outcome of the process. The kinetics of chemical reactions in a cold plasma can be considered as a particular case of non-equilibrium chemical kinetics. While equilibrium kinetics can be explained by means of theories of elastic collisions, the kinetics of plasma chemistry also has to take into account inelastic collisions. In the absence of thermodynamic equilibrium in the cold plasma, the state of a plasma is determined by external parameters, such as electric power, pressure, gas flow rate, and internal parameters, that is, the rate constants of the reactions leading to the formation or destruction of plasma species.

The knowledge of the kinetic constants is still insufficient for quantitative calculations of expected chemical behaviour of most systems in the plasma.

The existence of energetic particles and electromagnetic radiation in the plasma requires consideration of their interaction with the exposed surfaces. These physical interactions, which take place at any surface exposed to the plasma, have a significant effect on the results of the plasma treatment whether by affecting the heterogeneous chemical reactions or the treated surfaces. The plasma-surface interactions can be divided into two categories. One type of interaction takes place relatively far from the surface in which the electronic excitation energy of the particles dominates. The second type of interaction requires a much closer proximity to the surface or even penetration of the particles from the plasma into the crystal lattice, and therefore, involves the kinetic energy of the particles. Neutralisation of slow ions and associated electron emission fall into the first category, while cascade effects and sputtering fall into the second category.

Another aspect of plasma-surface interactions is the transfer of energy. Energy transfer from the plasma to solid surfaces occurs through optical radiation and fluxes of neutral particles and ions. The optical radiation has components in the infrared, visible, ultraviolet, and sometimes soft X-ray. When absorbed by a solid surface, the radiation usually transforms into heat.

The energy of the neutral particles is composed of kinetic, vibrational, dissociation (for free radicals), and excitation (for metastables) fractions. The dissipation of the kinetic and vibrational energy fractions causes heating of the substrate. The dissociation energy can also be dissipated through surface chemical reactions.

2.4 Conclusions

In this chapter we defined a plasma as a quasi-neutral gas of charged and neutral particles characterised by a collective behaviour. This collective behaviour of the plasma can be characterised by the use of physical parameters, such as the degree of ionisation and the temperature of the various plasma species, which will be more developed in the case of our deposition set-up in *Chapter 4*.

We showed that the processes taking place in plasmas are complex and in some cases, not yet fully understood. The plasma state exists under different forms, depending on the way they are generated.

Taking into account the wide ranges of parameters, the plasmas can be classified into several categories: plasmas in complete thermodynamic equilibrium, plasma in local thermodynamic equilibrium, and plasmas that are not in any local thermodynamic equilibrium, also called the cold plasmas.

In a microwave plasma discharge, the electrons are heated by the high frequency electric field. They undergo elastic and inelastic collisions which result in momentum and energy transfer from electron kinetic energy mode to internal and translational heavy particles energy modes. Reactive collisions between electrons and feed gas species also take place. They result in dissociation, ionisation, and electron attachment processes. Besides these electron impact processes, heavy particle-heavy particle collisions result in chemical reactions and energy redistribution between the different energy modes of the heavy species.

Due to the magnitude of the phenomena affecting the plasma and the resulting complexity of the plasma chemistry, it is not always possible to control the pathways of the chemical reactions or to predict the right combination of processes required for a certain outcome of the process.

Because the kinetics of chemical reactions in plasmas can be considered as a particular case of non-equilibrium chemical kinetics, the knowledge of the kinetic constants is still insufficient for quantitative calculations of expected chemical behaviour of most systems in the plasma. Modelling of the various chemical processes that take place in the plasma is therefore rather puzzling, as it will be seen in *Chapter 6*.

However, it is possible with the present knowledge of plasma physics and chemistry to adjust and control the composition of the gas mixtures and the parameters of the discharge to achieve the required results in terms of processing and materials properties, as presented in *Chapter 4* and *Chapter 5*.

3. Optical Emission Spectroscopy : the theory

3.1 Optical emission spectroscopy

Optical Emission Spectroscopy (OES) is a technique in which the photons emitted by electronically excited species are detected. It is applicable to systems in which there are sufficient numbers of excited species present, namely in plasmas during diamond CVD. OES is a very sensitive method of detection. It can be utilised to a wide variety of fluorescing species. To extract excited-state populations from emission intensities requires detailed knowledge of the radiative and non-radiative (e.g., quenching) processes for each emitting state.

The intensity of radiation of frequency ν_{ki} emitted by an atom or a molecule as a result of a radiative transition between two discrete states (*k*) and (*i*) is determined by the probability of finding the atom or molecule in the initial *k* state as well as by the inherent probability of the particular transition *k*→*i*.

It can be shown by statistical mechanics [77] that for a system in equilibrium at a temperature *T*, the ratio of the numbers of atoms *N* occupying the two energy states E_k and E_i is given by the Maxwell-Boltzmann formula:

$$\frac{Nk}{Ni}=\frac{gk}{gi}e^{-(Ek-Ei)/kT}.$$

The statistical weight *g* of a state is equal to its degeneracy – that is the number of distinct sub-states having the same energy. For atoms, a level of given quantum number *J* has a degeneracy of *2J+1*, that is a statistical weight of *2J+1*. Similarly, each rotational level of the simple vibrator-rotator model of a diatomic molecule has a statistical weight of *2J+1* multiplied by the statistical weight of the relevant electronic state (vibrational levels being non-degenerated).

The intensity of a given spectral line depends not only on the population of the initial level but also on the intrinsic probability of the particular transition, defined by the Einstein coefficients:

$$Iki=\frac{1}{4\pi}Akih\nu ikNk$$

where *h* is the Planck's constant, A_{ki} is the probability of spontaneous emission from the *k* state to *i* level in unit time (s) ($k>i$), and N_k is the population in atoms per cm³ of the *k* level.

3.2 Actinometry

To derive the total concentration of a species (including its ground electronic state) requires a further understanding of the excitation processes that created the emitting species. In practise, it is often impossible to relate observed emission intensities to ground state species concentrations. Actinometry provides a method to determine the relative concentration of some ground-state species with OES in the plasma [78]. In this technique, an actinometer, e.g. a noble gas, is chosen which has an excited-state energy level close to that of the species of interest and a small amount is added to the input gas stream. Since the energy levels of the actinometer and the studied species are close, the excitation efficiencies by electron impact or energy transfer are assumed to be similar. If an emitting state of an actinometer atom is produced by a direct electron impact, the intensity ratio of the chosen spectral line intensities of the observed component I_n and of the actinometer I_{act} does not depend on the electron density (*Eq. 3.1*).

$$\frac{In}{Iact} = \frac{KnNn}{KactNact} \approx k\frac{Nn}{Nact} \qquad \textit{(Eq.3.1)}$$

In this equation, N_n and N_{act} are respectively the concentrations of the analysed component and of the actinometer. K_n is the excitation rate coefficient of the observed spectral line, and is defined by

$$Kn = \int \sigma n(E) f(E)\sqrt{E}dE \qquad \textit{(Eq.3.2)}$$

where σ_n is the excitation cross-section and $f(E)$ is the electron distribution function, which is assumed to follow a Maxwell distribution. If the excitation rate coefficients are assumed to be equal and all the processes of loss of the excited state by other means than spontaneous emission are negligible, k is constant and the relationship (*Eq.3.1*) is linear.

Relative ground state atomic hydrogen concentrations were determined with OES during diamond CVD using argon as actinometer [78-81]. Argon presents radiative states with excitation thresholds close to that of the H-atom (Table 3.1 and *Appendix A.*).

Table 3.1: Involved emission lines and energy levels of H and Ar atoms

Wavelength (nm)	E_j	E_i
H_α (656.2)	12.09 eV	10.2 eV
H_β (486.1)	12.75 eV	10.2 eV
Ar (750.4)	13.48 eV	11.83 eV

For instance, the $2p^1$ radiative state of argon has a threshold at 13.48 eV which is very close to that of the hydrogen atom in the n=3 level with a threshold at 12.09 eV. For actinometry to be valid, both excited species Ar(4p) and H(n=3) have mainly to be excited directly from their respective ground electronic states by the collision of a single electron. The main processes involved for the production and the consumption of the H(n=3) electronic state of the H-atom are:

Production and consumption of H(n=3):

- electron excitation from the ground state:
  $\mathrm{H(n=1) + e \rightarrow H(n=3\ (s, p, d)) + e}$ (1)
- electron excitation from the n=2 state:
  $\mathrm{H(n=2) + e \rightarrow H(n=3\ (s, p, d)) + e}$ (2)
- dissociative excitation:
  $\mathrm{H_2 + e \rightarrow H(n=3) + H(n=1) + e}$ (3)
- radiative de-excitation:
  $\mathrm{H(n=3\ (s, p, d)) \rightarrow H(n=2\ (s, p)) + h\nu}$ (4)
  $\mathrm{H(n=3\ (p)) \rightarrow H(n=1\ (s)) + h\nu}$ (5)
- quenching processes :
  $\mathrm{H(n=3) + M_i \rightarrow H(n=1) + M_i^*}$ (6)
- ionisation processes from H(n=3):
  $\mathrm{H(n=3) + e \rightarrow H^+ + 2\ e}$ (7)

Since H(n=2) may be an intermediate in the production of H(n=3), its production and loss have to be taken into account.

Production and consumption of H(n=2):

- electron excitation from the ground state:
  $\mathrm{H(n=1) + e \rightarrow H(n=2\ (s, p)) + e}$ (8)
- collisional mixing processes:
  $\mathrm{Ar(metastable) + H(n=1) \rightarrow H(n=2) + Ar}$ (9)
  $\mathrm{Ar + H(n=2\ (s)) \rightarrow H(n=2\ (p)) + Ar}$ (10)
- electron excitation to the n=3 state:
  $\mathrm{H(n=2\ (s)) + e \rightarrow H(n=3\ (s, p, d)) + e}$ (11)
- radiative de-excitation:
  $\mathrm{H(n=2\ (p)) \rightarrow H(n=1\ (s)) + h\nu}$ (12)
- quenching processes:
  $\mathrm{H(n=2\ (s)) + M_i \rightarrow H(n=1) + M_i^*}$ (13)

For the Ar atom, the reaction paths for production and consumption are:

- electron excitation from the ground state:

  $Ar(n=3\ (p)) + e \rightarrow Ar(n=4\ (p)) + e$ (14)
- excitation from a metastable:

  $Ar(metastable) + e \rightarrow Ar(n=4\ (p)) + e$ (15)
- excitation to metastable:

  $Ar(n=3\ (p)) + e \rightarrow Ar(metastable) + e$ (16)
- radiative de-excitation:

  $Ar(n=4\ (p)) \rightarrow Ar(n=4\ (s)) + h\nu$ (17)
- quenching processes:

  $Ar(n=4\ (p)) + M_i \rightarrow Ar(n=3\ (s), n=4\ (p)) + M_i^*$ (18)

The processes of production of the states H(n=3) and H(n=2) through radiative cascades are here neglected due to the relatively high deposition pressures and low electron temperatures involved in diamond CVD processes.

In principle, actinometry can only be used if the excitation processes (1) and (15) and the de-excitation processes (4) and (17) are predominant. Then the following simple relationship can be obtained:

$$\frac{[H]}{[Ar]} = \frac{xH}{xAr} = k\frac{IH}{IAr}$$

where k depends on the electron energy distribution function (EEDF) due to the fact that the shapes and thresholds of the cross sections of the two excited species are not strictly equal. $[H]$ and $[Ar]$ represent respectively the concentration of atomic hydrogen and argon, xH and xAr their mole fractions and IH and IAr their associated emission intensities. In case where quenching processes are not negligible, the constant k depends on the quenching cross sections, the pressure, and the gas temperature.

Some species, such as methyl radicals, acetylene and methane, do not fluoresce efficiently enough and have not been detected by this method.

3.3 Temperature measurements

The particles contained in a gas mixture possess energy in various forms and may dissociate or ionise into fragments. They may also emit and absorb radiation at certain wavelengths. In thermodynamic equilibrium, for an adiabatic system, the distribution of energy over the various translational and internal degrees of freedom and the distribution of the radiation density, are governed by a single and universal parameter T. This parameter is the temperature of the system. At a given value of T, these distributions are independent of the type and rate of the detailed mechanisms through which energy is exchanged between the various forms or through which dissociation and ionisation are achieved.

Plasmas are not truly adiabatic systems. A net transport of heat, radiation, and mass occurs through the plasma. Under these conditions, a general thermodynamic state of equilibrium, characterised by a single temperature value, cannot exist. However, if the rate of these transport processes is comparatively slow with respect to the rate at which energy is locally partitioned over the various degrees of freedom, the concept of a local thermodynamic equilibrium characterised by a local temperature is meaningful.

The distribution of an assembly of gas particles with respect to available internal energy states is given by the Maxwell-Boltzmann formula

$$Nj = \frac{Ngj\, e^{-Ej/kT}}{\sum_{j} gj\, e^{-Ej/kT}} \qquad (Eq.3.3)$$

where N_j is the number of particles having energy E_j, N is the total number of particles, g_j is the statistical weight (probability) of energy E_j, k is Boltzmann constant, and T is the absolute temperature. The internal degrees of freedom of gas particles are nearly independent of each other. For each energy distribution, a corresponding statistical temperature, such as vibrational temperature, rotational temperature, or electronic temperature, can be defined.

In order for a temperature derived from an emission spectrum to have a meaning, the emitting species must be thermalised, that is, vibrational and/or rotational energy states populated according to Boltzmann distributions. For a system in thermodynamic equilibrium, population distributions in all energy states follow Boltzmann distributions that are defined by a single temperature, $T_g=T_e=T_v=T_J$, where the subscripts g, e, v and J refer respectively to the gas, electron, vibrational and rotational temperature. For reacting plasmas, departures from thermodynamic equilibrium are common, so differences between electronic, vibrational and rotational temperatures and gas temperatures can be expected. The differences observed for these temperatures in optical emission spectra are direct consequences of excitation processes that produce non-equilibrated excited state species distributions and a number of subsequent competing de-excitation processes, including spontaneous emission, collisional quenching, rotational (RET) and vibrational (VET) energy transfer. The optical emission spectrum provides therefore an ensemble measurement of the excited-state population distribution that reflects the net effect of the excitation and de-excitation processes involved. If the rate of collisional quenching is slow relative to the other excited-state collisional processes, the excited–state population distribution may become thermalised prior to spontaneous emission. In this case a temperature may be associated with this distribution and determined from the emission spectrum. On the other hand, if collisional quenching is relatively fast, then the emission spectrum will more closely reflect the nascent population distribution in the excitation process. Rates of RET and VET are currently available only for a limited number of reactive environments and is an active area of research today [82]. Nevertheless, since rates for RET are generally near gas kinetic and about ten times faster than those for VET [83,84], temperatures deduced from the rotational distribution of emitting molecules are more likely to reflect the gas temperature.

3.3.1 The Boltzmann plot method

At equilibrium, the populations of different energy states corresponding to internal degrees of freedom are given by the Maxwell-Boltzmann distribution (*Eq.3.3*). In principle, T can be found by measuring the absolute intensity of the emission line, provided A_{ki} is also known absolutely. In practice, the errors associated with the absolute intensity measurements and absolute values of oscillator strengths make this method very unreliable. To circumvent this problem, relative measurements are preferred. *Eq.3.3* can conveniently be rewritten as [85]:

$$\ln\frac{Iki\lambda ki}{gkAki} = const - \frac{Ek}{kT} \qquad (Eq.3.4).$$

A plot of $log(I\lambda/gA)$ against E for several spectral lines should be a straight line of slope $1/kT$. Deviations from the Boltzmann distribution should show up as deviations from the straight line.

Vibrational and rotational levels of molecules can be used instead of atomic levels. For vibrational levels, *Eq.3.4* becomes:

$$\ln\frac{I\lambda^4}{q\upsilon'\upsilon''} = const. - E\upsilon'/kT\upsilon \qquad (Eq.3.5),$$

where the relative band strengths are given by the Frank-Condon factors $q_{v'v''}$ and where $E_{v'}$ represents the energy of the upper vibrational level [85]. A plot of $ln(I\lambda^4/q_{v'v''})$ against $E_{v'}$ should yield a straight line whose slope determines T.

The straight line that fits the data points for the determination of the electron and/or vibration temperature with the Boltzmann plot method is generated by a linear least squares fitting function, assuming that all data points have an equal weight.

3.3.2 The Doppler broadening

Three different processes may contribute to the finite width of a spectral line: natural broadening, Doppler broadening, and interactions with neighbouring particles. In case of free atoms and molecules, this last can be mainly treated as pressure broadening.

When the Schrödinger equation is solved for a system that is changing with time, it is found that it is impossible to specify its energy levels exactly. If on average a system survives in a state for a time τ, the lifetime of the state, then its energy levels are blurred to an extent of order δE, where $\delta E \approx h/2\pi\tau$. This relation is reminiscent of the

Heisenberg uncertainty principle. According to it, the position and momentum (or velocity) of a particle cannot be simultaneously measured with any direct accuracy. No excited state has an infinite lifetime. Therefore, all states are subject to some lifetime broadening, and the shorter the lifetimes of the states involved in a transition, the broader the spectral lines. Two processes are principally responsible for the finite lifetimes of excited states. The dominant one is collisional deactivation, which arises from the collisions of atoms and molecules with other atoms and molecules or the walls of the container. The collisional lifetime ($\tau_{collision}$) can be lengthened by working at low pressures. Spontaneous emission, the process by which an excited state discards photon, is responsible for a natural limit on the lifetime, $\tau_{natural}$, and gives rise to the natural linewidth of the transition. This is an intrinsic property of the transition and cannot be changed by modifying the conditions. Natural linewidths depend strongly on the transition frequency (they increase as ν^3), and so-low-frequency transitions (e.g. microwave transitions of rotational spectroscopy) have very small natural linewidth, and collisional and Doppler line-broadening processes are dominant. The natural lifetimes of electronic transitions are much greater than those of vibrational and rotational transitions. For example, a typical electronic excited state natural lifetime is about 10^{-8} s, corresponding to a natural width of about 5 10^{-4} cm^{-1} (15 MHz). A typical rotational natural lifetime is about 10^{3} s, corresponding to a natural linewidth of only 5 10^{-15} cm^{-1} (10^{-4} Hz).

Thermal motion of light-emitting particles in the plasma leads to a wavelength shift of the observed radiation due to the Doppler effect. When a source emitting radiation of wavelength λ recedes from an observer with a speed υ, the observer detects radiation of wavelengths $(1+ \upsilon/c)\,\lambda$, where c is the speed of the radiation. A source approaching the observer appears to be emitting radiation of wavelengths $(1- \upsilon/c)\,\lambda$.

Atoms and molecules reach high speeds in all directions in a gas, and a static observer detects the corresponding Doppler shifted range of wavelengths. Some molecules approach the observer, some move away. Some move quickly, others slowly. The detected spectral 'line' is the emission profile arising from all the resulting Doppler shifts. This profile reflects the Maxwell distribution of atomic and molecular speeds parallel to the line of sight, which is a bell-shaped gaussian curve.

A Doppler-broadened line is determined entirely by the atomic or molecular weight of the emitter and its kinetic temperature:

$$\frac{\Delta\lambda_D}{\lambda_0} = \frac{2}{c}\sqrt{\frac{2RT}{M}} \qquad (Eq.3.6)$$

where $\Delta\lambda_D$ is the Doppler broadening measured at the wavelength λ_0, c is the speed of light, R is the gas constant, M is the atomic mass of the atom, and T is the temperature expressed in K. Notice that the line broadens as the temperature is increased.

As atomic hydrogen is the lightest atom, the Doppler broadening line is particularly large, and this is advantageous for temperature measurements.

The full width at half maximum (FWHM) of the mercury line at 546.0 nm is used to determine line broadening due to the OES set-up.

3.4 Conclusions

In this chapter we show that Optical Emission Spectroscopy (OES) can be used for other purposes than just the qualitative analysis of the plasma.

Semi-quantitative analysis of the plasma, or actinometry, can be achieved if certain precautions and assumptions are taken. Results on actinometry will be further presented in *Chapter 4*.

We also show that it is possible to calculate the temperature of the emitting species from an optical emission spectrum. In order for a temperature derived from an emission spectrum to have a meaning, the emitting species must be thermalised, that is, the population of the different energy states corresponding to internal degrees of freedom of the emitting species should follow a Maxwell-Boltzmann distribution. Departures from thermodynamic equilibrium are common for reacting plasmas. A plasma is therefore characterised by a gas, electron, vibrational and rotational temperature that are the direct consequences of the excitation processes that produce non-equilibrated excited state species distributions and of subsequent competing de-excitation processes. The presented concepts will be used in *Chapter 4* to determine the temperature of some of the plasma species during deposition.

4. Characterisation of the plasma

4.1 Deposition set-up

The diamond thin films are synthesised in a 5 kW Astex PDS-17 microwave PA-CVD system operating in the high growth rate mode with typical deposition rates varying between 0.5 µm/h and 3 µm/h (Fig.4.1). To achieve high growth rates, depositions are carried out at sub-atmospheric pressures (from 6.6 kPa to 16 kPa) at high microwave power (typically from 3 kW to 5 kW).

Figure 4.1: Astex PDS-17 kW microwave PA-CVD system.

The shape and size of the plasma ball are function of the vessel pressure and of the dissipated microwave power. Since diamond depositions are to be achieved on a constant surface of 6 cm in diameter, it was important to optimise the size of the plasma to the deposition area. Since emission intensities are volume dependent, it was also crucial to study a plasma ball which volume remains as good as constant over the explored domain. The parameters choice was therefore set on symmetric plasma balls obtained at pressures of about 11.5 kPa and at microwave powers of about 3 kW. In such conditions, the average input microwave power density (in W/cm³), defined as the input microwave power over the volume of the plasma [86], is equal to 26.5 W/cm³. The relative error made on the determination of the plasma volume has been estimated around 10 %, owing to the difficulty to determine the plasma volume, that on the power density at around 10 %, owing to the uncertainty on the injected power (injected and reflected powers are measured only by the instrumental power-meters). The absorbed power is not known. However, according to Tan *et al.* [87], it should be close to the net injected power.

The electron density (n_e) is not accessible experimentally. It was estimated by analogy, along the axis of the reactor, from the one-dimensional H_2 plasma diffuse flow model developed at the laboratory of Gicquel *et al.* [86] for a microwave plasma operating in the same processing conditions as ours. The electron density was estimated at 2.06 10^{12} cm^{-3} for a pressure of 11.5 kPa and an average injected power density of 26.5 W/cm³. According to Gicquel *et al.* [86], the error made on the electron density is mainly attributed to the power effectively absorbed by the plasma and to the assumption that the electron energy distribution function is Maxwellian. Calculations by Scott *et al.* [88] carried out without assuming a Maxwell distribution for the electron energy, indicated that n_e is overestimated by 20 % to 35 % when assuming a Maxwell distribution.

The electron energy distribution function might be sensitive to the excitation frequency, the pressure, the metastable and the radiative species concentrations, and the atom fraction [86]. In addition, in the case of diamond deposition plasmas, it should be sensible to the fraction of methane introduced and to its degree of dissociation.

A new molybdenum holder of 6 cm in diameter was developed in which the substrates were fully embedded. This configuration allowed us to keep the plasma sheet parallel to the substrate surface and to minimise variations in the plasma volume in the vicinity of the substrate surface by giving the plasma a cylindrical shape up to a distance of 12 mm from the substrate surface.

During depositions, the substrate temperature is monitored by an infrared photo-pyrometer calibrated in function of the emissivity of diamond.

The depositions are carried out on (100) silicon wafers. To decrease the incubation time and to increase the nucleation density, the silicon wafers are abraded for about 20 min by 0.1 µm diamond powder on a vibrating plate. The samples are then ultrasonically rinsed in ethanol for about 10 min.

4.1 Gas phase precursors

Diamond of similar quality and morphology has been grown using a wide variety of species, including aliphatic and aromatic hydrocarbons, ketones, amines, ethers, alcohols, carbon monoxide, carbon dioxide and halogen containing alkanes (CBr_4, CI_4, CCl_4, CF_4) [4, 89]. Methane is the most frequently used reagent because it has one of the highest diamond growth efficiency.

For this reason, we chose for conventional methane-hydrogen plasmas to which we added, for the purpose of our study, minute quantities (ppm range) of nitrogen.

The gases used for deposition with their related purity are summarised in Table 4.1 below.

Table 4.1: Gases used for deposition with related purity.

Gas	*Purity*
Hydrogen	99.9997 vol.%
Methane	99.995 vol.%
Oxygen	99.9995 vol.%
Hydrogen-nitrogen (1 vol.% ± 0.02 vol.%) mixture	99.9999 vol.%
Argon	99.9999 vol.%

The gas flows are controlled by mass-flow controllers (MFC) calibrated for diatomic nitrogen. Gas correction factors depending on the specific heat capacity of the various gas species used are applied to derive the mass flow coming out of each flow controller. During deposition, the total mass-flow is set at 210 sccm (standard cubic centimetre per minute).

The accuracy and resolution of the various mass-flow controllers used are listed in ***Table 4.2***.

Table 4.2: Accuracy and resolution of the mass-flow controllers.

Gas	*Accuracy*	*Resolution*
Hydrogen	± 5 sccm	0.5 sccm
Methane	± 0.5 sccm	0.05 sccm
Oxygen	± 0.5 sccm	0.05 sccm
Hydrogen-nitrogen mixture	± 0.2 sccm	0.02 sccm
Argon	± 0.1 sccm	0.01 sccm

The impurities present in the feed gases and the vacuum leakage of the deposition system contribute to a flux of respectively 1.5 ppm N_2 and 1.6 ppm N_2.

4.3 Characterisation of the OES set-up

The advantages of the OES technique are that it is inexpensive, fairly easy to implement and does not in any way disturb the deposition processes. Drawbacks of OES technique are that OES alone provides an initial but incomplete picture of the chemical environment, as only light emitting species are identified, and that models have to be included to get more than data on the composition out of it.

The set-up for OES is illustrated in Fig.4.2. The light emitted by the plasma is captured by an optical fibre and is sent to a Spectraview UV enhanced CCD detector through a Jobin-Yvon HR 460 SHL monochromator (Fig.4.3) in a Czerny-Turner configuration. The monochromator with a focal length of 0.46 m is equipped with a 1200 grooves per mm holographic grating blazed at 330 nm. With this set-up we are able to monitor a 45 nm wide window in the 240-1200 nm spectral range with a theoretical resolution of 0.06 nm.

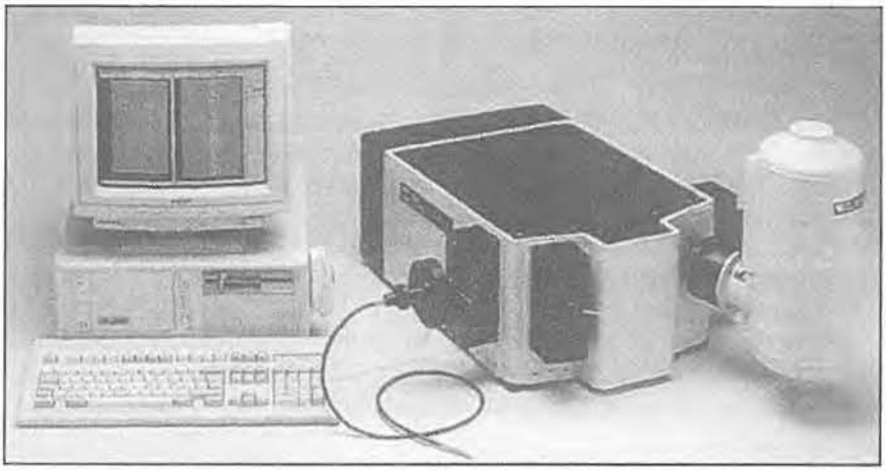

Figure 4.2: HR460 flat field spectrograph equipped with a SpectraView-2D™ CCD detection system with fibre optic adapter and automatic shutter.

The acquired emission intensities are average intensities over the volume captured by the optical fibre. The *critical angle* of the optical fibre is calculated from the indices of refraction of the core and the clad of the optical fibre. The sine of the critical angle is called the numerical aperture, abbreviated N.A.

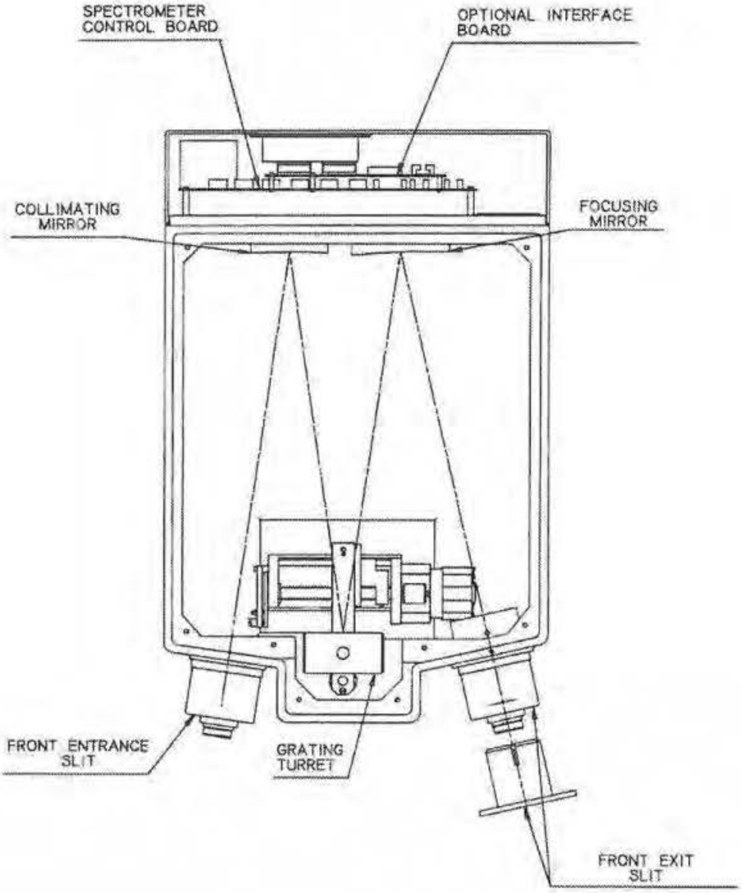

Figure 4.3: Schematic view of the SHL 460 monochromator. Front entrance with automatic shutter and optical fibre, front exit with CCD detector.

For example, the numerical aperture of the optical fibre given by the manufacturer is equal to 0.22, which corresponds to a critical angle of 12.7 degrees. As the fibre accepts light up to 12.7 degrees off axis in any direction, we define the *acceptance angle* of the fibre as twice the critical angle, or in this case, 25.4 degrees. The f/number equivalent of the N.A. is calculated as follows:

$$f\# = \frac{1}{2N.A.}.$$

The size of the plasma volume captured can therefore be approximated to a cone ($V_{captured} \approx 490\ cm^3$) embracing the whole plasma ball ($V_{plasma} \approx 114\ cm^3$). In this configuration, the optical measurements are significantly perturbed by light scattering, which effect is amplified by the highly reflective stainless steel reactor walls.

To investigate the plasma composition at different stages in the plasma ball, it was therefore necessary to reduce the volume captured by the optical fibre. For this purpose, an optical probe was built (Fig.4.4).

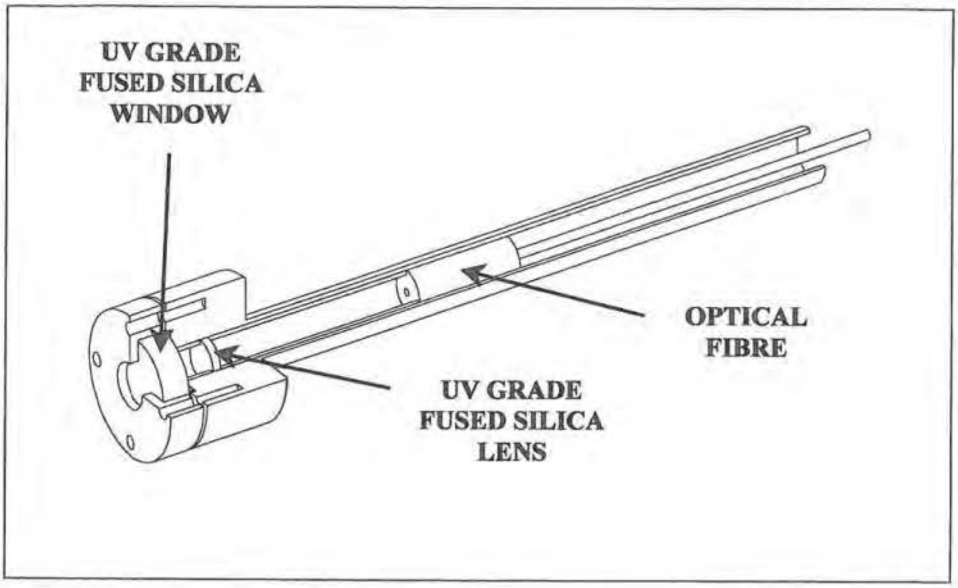

Figure 4.4: Cross-section of the home-made optical probe.

The optical probe consists of a cylindrical stainless steel tube containing an UV-enhanced fused silica bi-convex lens. The distance between the lens and the centre of the plasma ball corresponds to the focal distance (f = 100 mm) (Fig.4.5), while the distance separating the lens from the optical fibre is fixed at f/2. A plane parallel UV-enhanced fused silica window ensures the separation between the vacuum chamber and the optical lens.

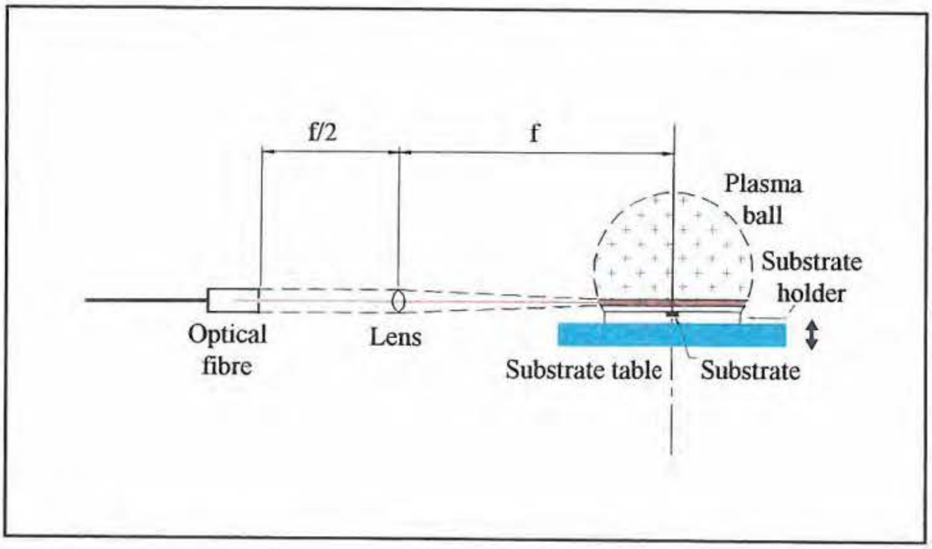

Figure 4.5: Schematic representation of the OES set-up.

By moving a tungsten ribbon lamp with a 1mm large filament along the optical fibre-lens axis (Fig.4.6) and perpendicular to it at the focal distance f (Fig.4.7), it was possible to define the plasma volume captured by the optical probe. In this described configuration, the use of the probe reduces the captured plasma volume to a conical bundle of about 0.2 cm^3. This set-up reduces considerably the interference of scattered light on the determination of the real emission intensities. It also makes it possible to sample small plasma volumes at the vicinity of the substrate surface without recording interference due to the substrate holder.

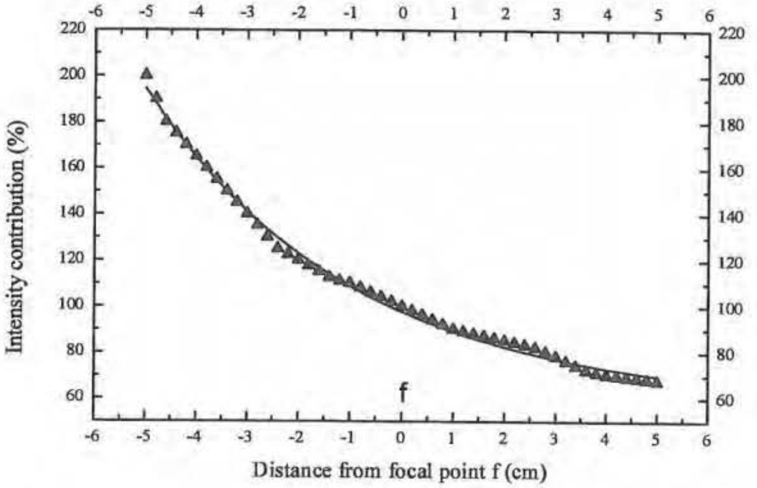

Figure 4.6: Relative intensity recorded as a function of the distance from the focal point on the optical fibre-lens axis.

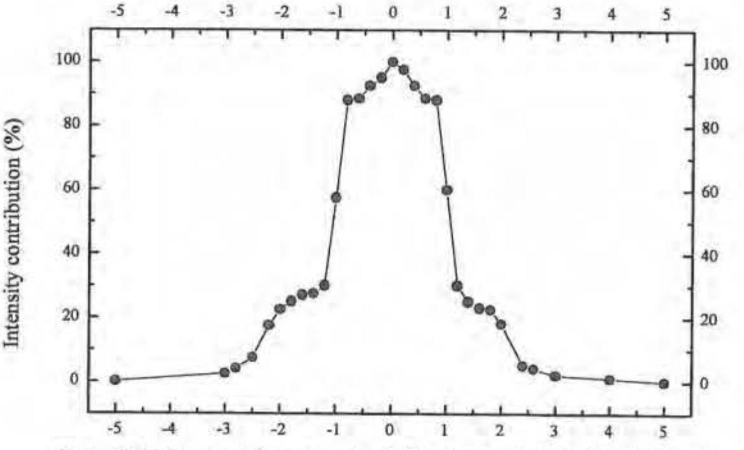

Figure 4.7: Relative intensity recorded as a function of the distance perpendicular to the optical fibre-lens axis at the focal point f.

The spectral dependence of the complete OES set-up was settled by using a tungsten ribbon lamp with a well-known spectral radiance distribution. The ratio of the halogen lamp spectrum measured through the OES set-up (I_f) over the spectral radiance distribution of the halogen lamp (I_i) gives the spectral dependence (transmittance I_f/I_i) of the OES system for the 1200 grooves per mm grating (Fig.4.8).

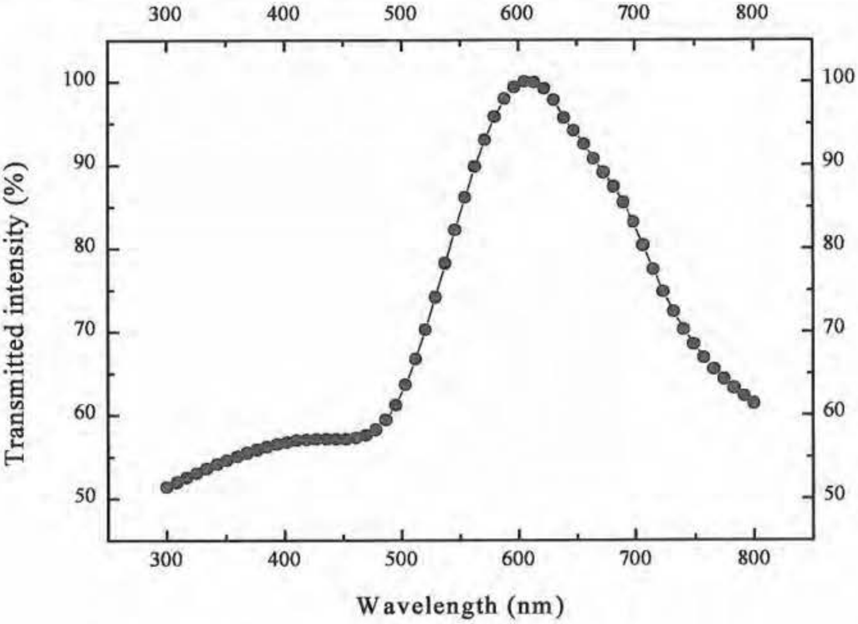

Figure 4.8: Transmittance curve (I_f/I_I) of the complete optical set-up as a function of the wavelength.

The wavelength calibration is accomplished by comparing the peak values of the atomic hydrogen lines of the Balmer series to the measured one taken with the optical probe [70, 90-92].

4.4 Identification of the light emitting species

Pure hydrogen plasma are characterised by the presence of the Balmer atomic hydrogen emission lines (H_α 656.3 nm, H_β 486.1 nm, H_γ 434 nm and H_δ 410.2 nm) and the Fulcher α ($d^3\Pi_u$-$a^3\Sigma_g$) molecular hydrogen bands mainly dispersed over the 590 nm – 640 nm region [78] (Fig.4.9).

When methane is added to the hydrogen plasma, the CH $A^2\Delta$-$X^2\Pi$ system with the Q(0,0) band head at 431.4 nm, the CH $B^2\Sigma$-$X^2\Pi$ system with the Q(0,0) band head at 388.9 nm and the C_2 Swan system ($A^3\Pi_g$-$X^3\Pi_u$) with the Q(0,0) and Q(1,1) band heads respectively at 516.5 nm and at 512.9 nm as most intense C_2 emission bands, superimpose on the hydrogen spectrum [90-92] (Fig.4.9).

Small nitrogen quantities in a methane-hydrogen plasma are mainly detected by the presence of the CN violet system ($B^2\Sigma$-$X^2\Sigma$), with the Q(0,0) band head at 388.3 nm as most intense and sensitive CN band. At much higher nitrogen concentrations (> 2000 ppm N_2), N_2 emission bands are present in the spectrum, with the Q(0,0) band head at 337.1 nm as most intense N_2 band [92] (Fig.4.9).

The addition of more than 5 vol.% O_2 to a methane-hydrogen plasma gives rise to the presence of OH emission bands from the 3064 Å system ($A^2\Sigma^+$-$X^2\Pi$), with the $Q_1(0,0)$ and $Q_2(0,0)$ band heads at 307.8 nm and 308.9 nm as most intense emission bands, and from the Meinel bands ($X^2\Pi$), with the 771.47 nm from the R branch and the 775.58 nm from the Q branch as most intense emission band heads [92] (Fig.4.9).

When added to the feed gas for actinometric purposes, argon is mainly detected by the presence of the 750.4 nm emission line (Fig.4.9).

Further information about the transition in the given radicals and molecules can be obtained from *Appendix A*.

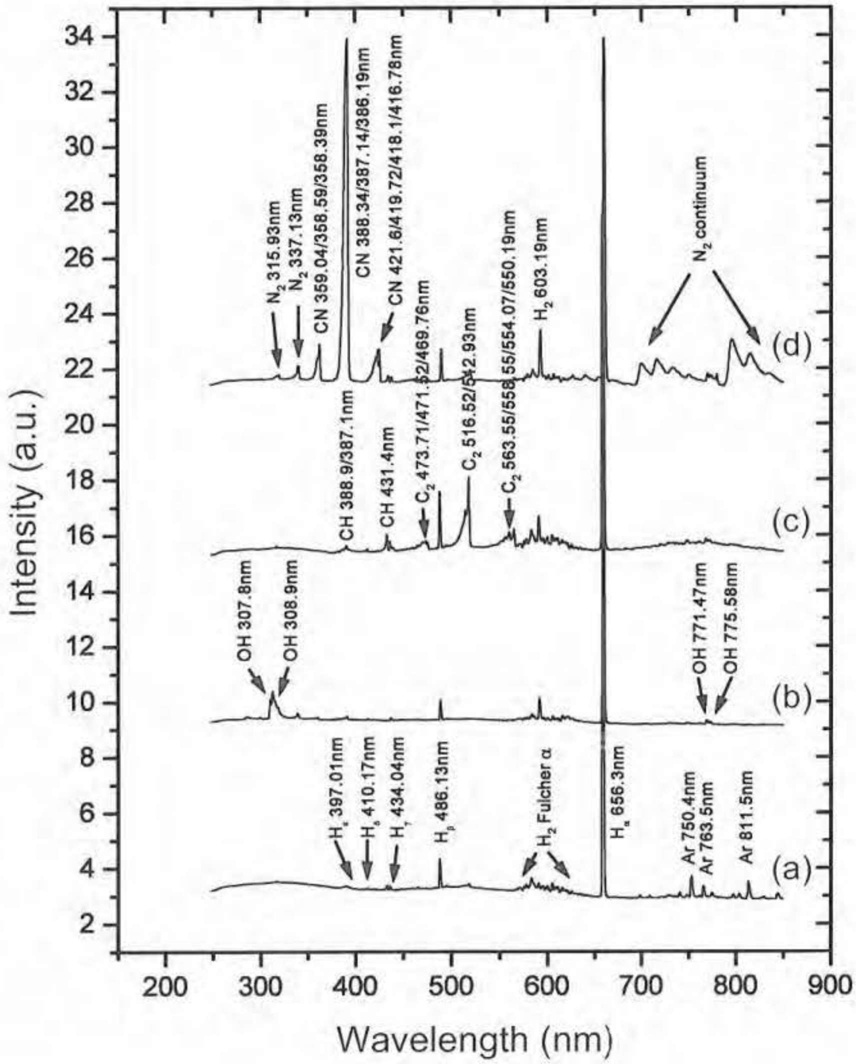

Figure 4.9: OES spectra of H_2+Ar (a), H_2+O_2 (b), H_2+CH_4 (c), and H_2+CH_4+N_2 (d) plasmas recorded using the same experimental conditions.

4.5 Limit of detection

The detectability of species depends on the strength of the fluorescence transition (i.e., the dipole transition moment), the rate of non-radiative quenching processes and the concentration of excited species produced by the plasma.

The detection is defined as the minimum concentration that can be detected by the analytical method, optical emission spectroscopy, with a given certainty. This is often taken [93] as the mean value of the blank, plus three times its standard deviation (Fig.4.10). According to this definition, the following detection limits were calculated for the various gas species added to a 3kW hydrogen microwave plasma obtained at a pressure of 11.5 kPa with a total gas flow of 210 sccm (Table 4.3). It must be borne in mind that the absence of emission lines of an element indicates merely that the element is not present in sufficient amount to be detected with the source (plasma) and equipment used.

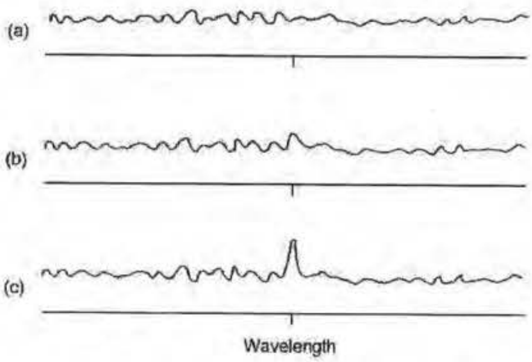

Figure 4.10: Detection limit. No signal occurs in (a), with the response appearing as background noise. In example (b), while it may appear that a small signal occurs at the specified wavelength, this is not discernible from the background noise. The most likely signal occurs in example (c) [93].

With our OES set-up, the intensity of a given emission line is measured with an uncertainty of about 2 % (1 σ).

Table 4.3: OES detection limits of the various gas species used.

Gas	*I.D.*	*Detection limit*
CH_4	C_2 at 516.5 nm	10 vol.ppm
N_2	CN at 388.3 nm	15 vol.ppm
Ar	Ar at 750.4 nm	1 vol.%
O_2	OH at 308.9 nm	1.5 vol.%

4.6 Optical Emission Spectroscopy during deposition

For all actinometry measurements, 2 vol.% argon are added to the deposition gas mixture. Experimental measurements show that argon does not disturb the IH_β/IH_α ratio up to 5 vol.%.

4.6.1 Effect of methane concentration on the plasma chemistry

The process parameters used for this set of OES measurements are summarised in Table 4.4.

Table 4.4: Methane addition: process parameters for the OES measurements.

Microwave power	3000 W
Vessel pressure	11.5 kPa
Total gas flow	210 sccm
Methane percentage (in volume)	0-10 %
Substrate material	Si (100)
Substrate temperature	1000-1050 K

The OES measurements are taken at a distance of 5 mm above the substrate surface using the optical probe with a build-in focusing lens.

The addition of methane in hydrogen plasmas is detected by the presence of the CH and C_2 emission bands. In the bulk of the plasma, the intensity of the CH(431.4 nm) and C_2(516.5 nm) band heads increases linearly with the percentage of methane added to the feed gas (Fig.4.11). The IH_β/IH_α ratio on the other hand does not seem to be affected by methane addition, as the IH_β/IH_α intensity ratio remains approximately constant up to 10 vol.% methane. Actinometric measurements of the relative atomic hydrogen concentration in the plasma with 2 vol.% Ar show that the IH_α/IAr(750.4 nm) ratio stays almost constant when the methane concentration in the feed gas increases from 0 vol.% to 10 vol.%. This result is in agreement with the results obtained by Gicquel *et al.* [80], Mucha *et al.* [94] and Celii *et al.* [42] who observed a similar behaviour in the atomic hydrogen concentration as a function of the methane fraction in microwave plasma.

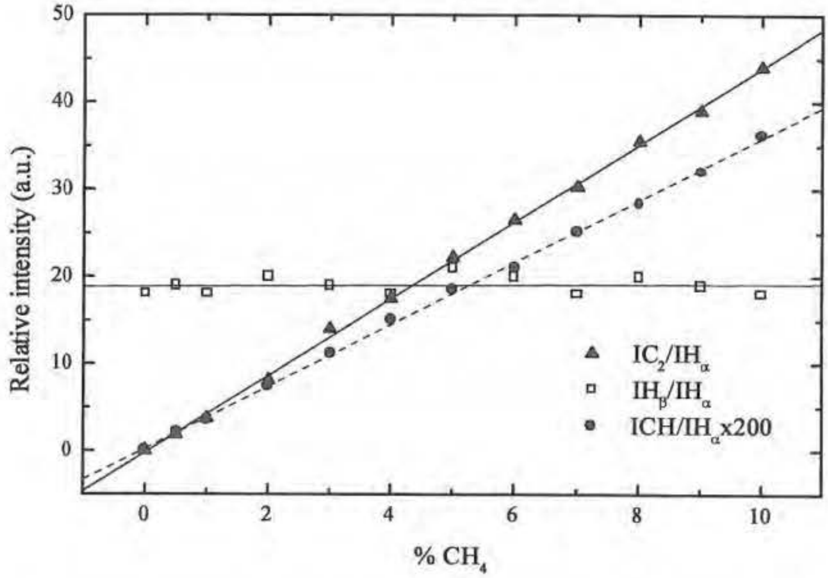

Figure 4.11: Evolution of the relative intensity of CH, C_2, and H_β as a function of the methane fraction in a hydrogen plasma.

Assuming that the H_α emission line broadening is Doppler dominated, the average temperature of the hydrogen atom is found to be around 4900 K. Increasing the methane content in the plasma does not affect the Doppler broadening of the atomic hydrogen lines. This is probably due to the poor resolution of the spectrometer. The main error on the determination of the temperature of the hydrogen atom relies on the fact that the emission line broadening is not fully Doppler dominated. Gicquel *et al.* [86] showed that not taking into account the Stark broadening and pressure broadening could lead to an underestimation of the temperature of hydrogen atoms calculated from the H_α emission line. The Stark broadening and the pressure broadening are responsible for "lowering" of respectively 100 K to almost 200 K and of 20 K to 60 K of the temperature of the hydrogen atoms according to the experimental conditions.

The addition of 5 vol.% methane to a hydrogen plasma produced at 3000W and 11.5 kPa shows that the temperature of the hydrogen atoms determined from a Boltzmann plot decreases from 5500 K to 5200 K, that is a loss of about 300 K (Fig.4.12). A least squares fit on the data set shows that the standard error made on the slope contributes to a relative error of about 2% on the determination of the atomic hydrogen temperature.

The vibrational temperature of the C_2 radical is calculated from the Q(1,0), Q(2,1), Q(3,2) and Q(4,3) band heads of the C_2 Swan system $A^3\Pi_g$-$X'^3\Pi_u$. The main error made on the determination of the vibration temperature of the C_2 radical relies, as for the Boltzmann atomic hydrogen temperature, on the difficulty to determine the slope of the fitting straight line. In this case, the error made on the slope is responsible for a relative error of 2% on the determination of the vibrational temperature. The Franck-Condon factors used for the calculation of the vibrational temperature from a Boltzmann are summarised in Table 4.5.

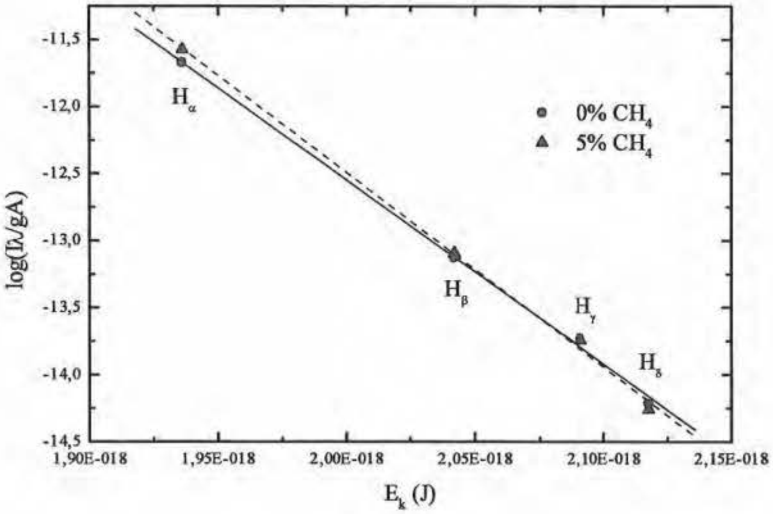

Figure 4.12: Determination of the temperature of hydrogen atoms ($T(H_\alpha)$) in the plasma by the Boltzmann plot technique using the Balmer atomic hydrogen emission lines. E represents the energy of the transition level. I, λ, g, and A are respectively the intensity, the wavelength, the statistical weight and the transition probability of the emission line of interest.

Table 4.5: Molecular constants of C_2 used in calculations for $\Delta v=1$ [90]

C_2	*Wavelength (nm)*	Franck-Condon factor
Q(1,0)	473.71	$q_{10} = 0.248$
Q(2,1)	471.54	$q_{21} = 0.375$
Q(3,2)	469.76	$q_{32} = 0.423$
Q(4,3)	468.49	$q_{43} = 0.431$

The vibrational temperature is determined from the Boltzmann plot of $ln(I\lambda^4/q_{v'v''})$ against $E_{v'}$ which yields a straight line proportional to $1/T$ (Fig.4.13).

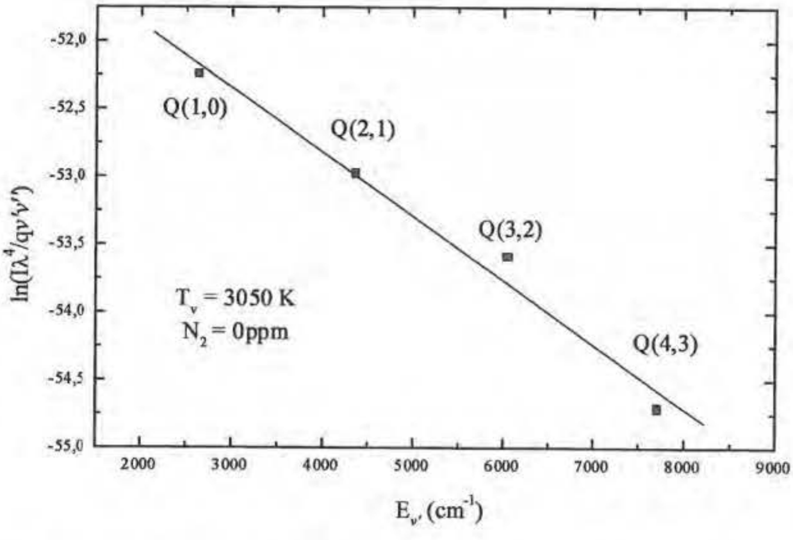

Figure 4.13: Determination of the vibrational temperature of C_2 from a Boltzmann plot. I, λ, $q_{v'v''}$ and $E_{v'}$ are respectively the intensity, the wavelength, the Franck-Condon factor and the level energy of the transition of interest.

For a methane fraction of 5 % in volume, the vibrational temperature of the C_2 radical was found to be equal to 3050 K ± 305 K.

4.6.2 Effect of minute nitrogen addition on the plasma chemistry

The OES measurements are taken 1 mm above the substrate surface. The process conditions are summarised in Table 4.6.

The relative atomic hydrogen concentration determined by actinometry (Fig.4.14) shows that the IH_α/IAr increases by a factor 1.5 over the 0 – 1000 ppm N_2 range, while, over the same range, the relative molecular hydrogen concentration decreases by the same factor.

Table 4.6: Nitrogen addition: process parameters for the OES measurements.

Microwave power	3000 W
Vessel pressure	11.5 kPa
Total gas flow	210 sccm
Methane percentage (in volume)	4.8 %
Argon percentage (in volume)	3.8 %
Nitrogen content (in volume)	0-950 ppm
Substrate material	Si (100)
Substrate temperature	1000-1050 K

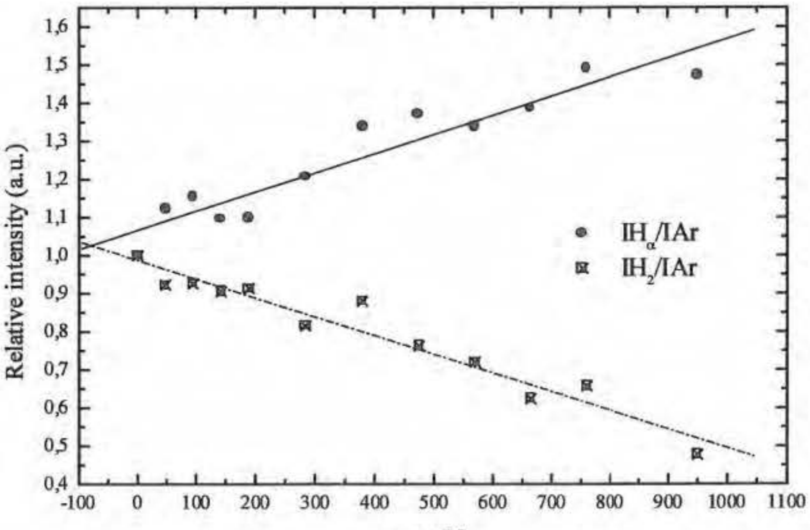

Figure 4.14: Evolution of the relative intensity of atomic hydrogen H_α and molecular hydrogen H_2(603.16 nm) as a function of the nitrogen content in the feed gas.

The relative concentrations of CN(388.3 nm), C_2(516.5 nm) and CH(431.4 nm) increase linearly as a function of the nitrogen content in the gas phase (Fig.4.15 and Fig.4.16). The ICN/IH_α ratio increases by a factor 30 from 47.5 ppm to 950 ppm, while over the same range, the ICH/IH_α and IC_2/IH_α ratios only increase by a factor 2. The ICH/IH_α ratio is about an order of magnitude lower than the IC_2/IH_α ratio.

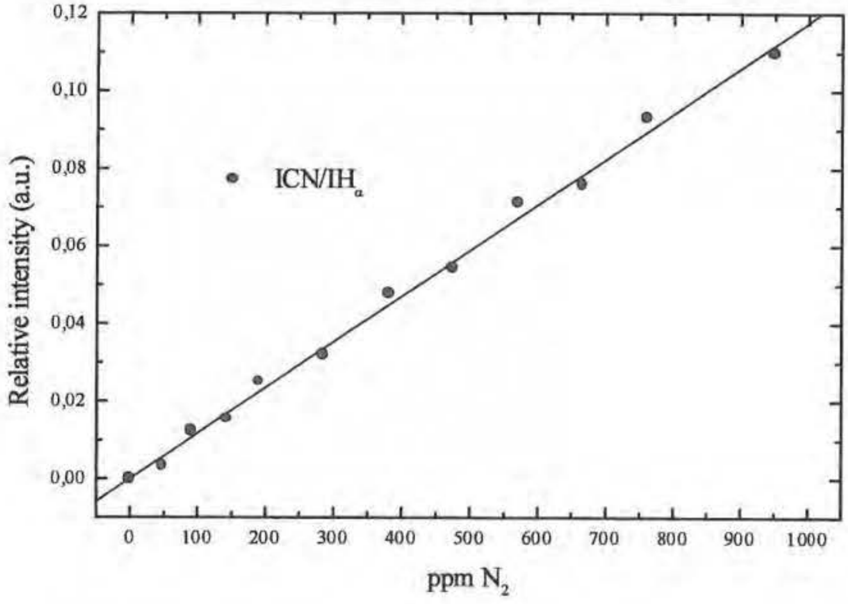

Figure 4.15: Evolution of the relative intensity ICN(388.3 nm)/IH_α as a function of the nitrogen content in the feed gas.

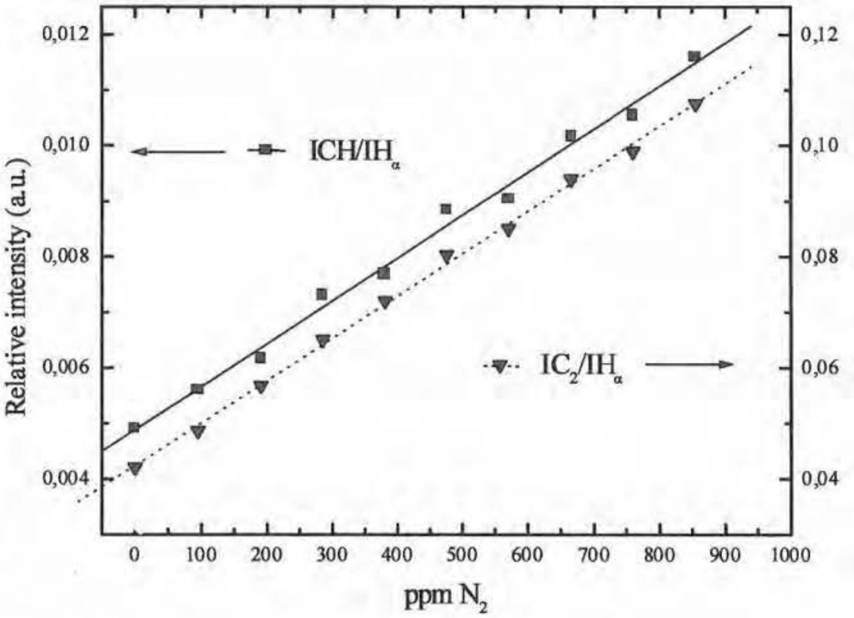

Figure 4.16: Evolution of the relative intensity ICH(431.4 nm)/IH$_\alpha$ and IC$_2$(516.5 nm)/IH$_\alpha$ as a function of the nitrogen content in the feed gas.

Fig.4.17 shows that the ICH(431.4 nm)/IC$_2$(516.5 nm) ratio is rather constant as a function of the nitrogen fraction in the plasma and oscillates around 1:10. The ICN(388.3 nm)/IC$_2$(516.5 nm) ratio increases linearly from 0 to 1 between 0 ppm and 950 ppm N$_2$.

Nitrogen seems to enhance the dissociation of methane in the plasma, as the production of CN does not occur at the expense of the CH and C$_2$ radicals. On the contrary, the intensity of all emitting carbon containing radicals increases with the nitrogen fraction in the feed gas. As atomic hydrogen is a dissociation product of methane, its concentration in the plasma rises with the nitrogen content in the plasma too. The relative molecular hydrogen concentration in the plasma decreases with the increasing nitrogen content in the feed gas. This suggests that nitrogen could have an impact on the dissociation degree of molecular hydrogen in the plasma too.

From the OES point of view, it is clear that nitrogen, even at very low concentrations, disturbs significantly the plasma chemistry and increases the total amount of carbon containing radicals in the plasma.

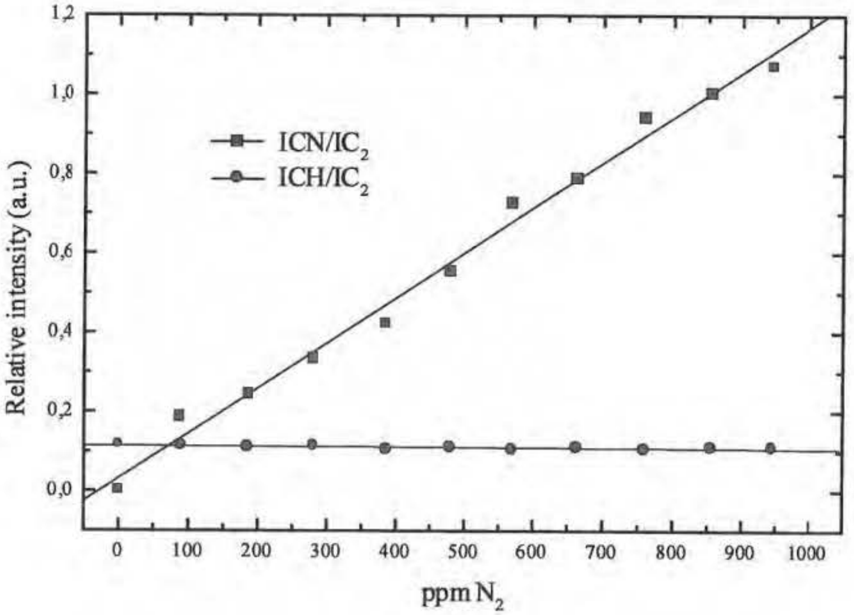

Figure 4.17: Evolution of the relative intensity ratios ICN(388.3nm)/IC$_2$(516.5nm) and ICH(431.4nm)/IC$_2$(516.5nm) as a function of the nitrogen content in the feed gas.

The temperature of the hydrogen atoms $T(H_\alpha)$ calculated from the broadening of the H_α emission line, assuming that the broadening is only Doppler dominated [86], shows that the temperature of hydrogen atoms drops from 5600 K at 0 ppm N_2 to 4800 K at 1000 ppm N_2. The main error made on the determination of the temperature of hydrogen atoms relies on the fact that the emission line broadening is not fully Doppler dominated. Gicquel *et al.* [86] showed that not taking into account the Stark broadening and pressure broadening could lead to an underestimation of 120 K to 260 K of the temperature of hydrogen atoms calculated from the H_α emission line, according to the experimental conditions.

The temperature of hydrogen atoms $T(H)$, calculated from a Boltzmann plot, drops exponentially from 5330 K ± 610 K to 4600 K ± 530 K between 0 ppm and 1000 ppm N_2 (Fig.4.18).

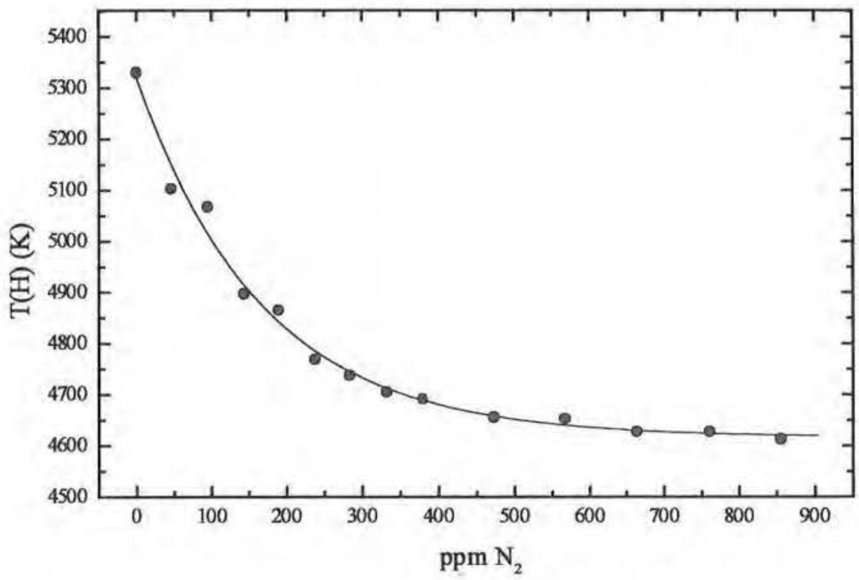

Figure 4.18: Evolution of the temperature of hydrogen atoms *T(H)* calculated from a Boltzmann plot using the Balmer atomic hydrogen emission lines as a function of the nitrogen fraction in the plasma.

As shown in Fig.4.19, the vibrational temperature of C_2 increases almost linearly from 3050 K ± 305 K to 4500 K ± 450 K between 0 ppm and 475 ppm N_2. The vibrational temperature then decreases slowly in an exponential way to stabilise around 4300 K ± 430 K for nitrogen fractions larger than 665 ppm.

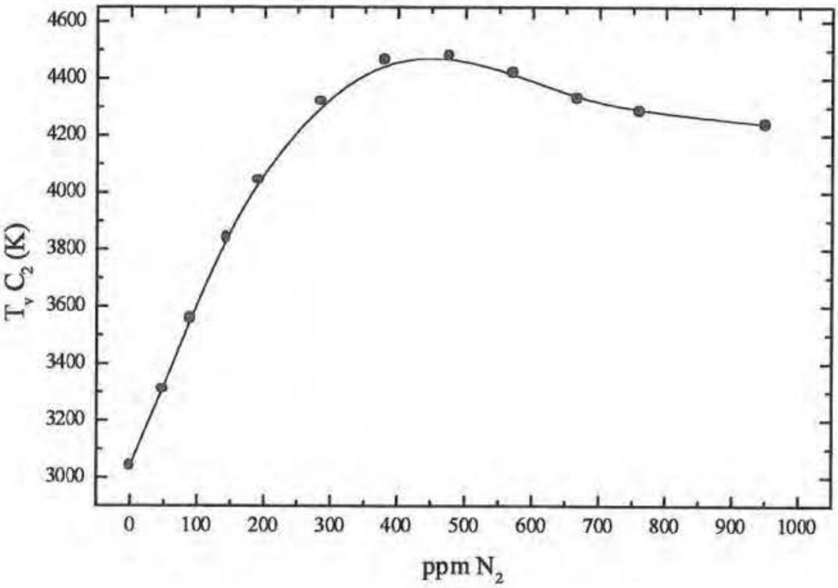

Figure 4.19: Evolution of the vibrational temperature of C_2 as a function of the nitrogen content in the plasma.

4.7 Spatial distribution of the light emitting species

By adjusting the height of the substrate holder millimetre per millimetre (with a precision of ± 0.25 mm), it is possible to monitor variations in the emission intensities of the plasma species as a function of the distance from the substrate surface. The process parameters are summarised in Table 4.7.

For convenience, the nitrogen content in the feed gas is fixed at 475 ppm in volume. Other nitrogen contents show the same trends with respect to their spatial distribution in the plasma.

Table 4.7: Spatial distribution of the plasma species: process parameters for the OES measurements.

Microwave power	3000 W
Vessel pressure	11.5 kPa
Total gas flow	210 sccm
Methane percentage (in volume)	4.8 %
Argon percentage (in volume)	3.8 %
Nitrogen content (in volume)	475 ppm
Substrate material	Si (100)
Substrate temperature	1000-1050 K

The IH_β/IH_α ratio remains constant from 1 up to 12 mm above the substrate surface, while the actinometric IH_α/IAr and IH_β/IAr ratios increase by a factor 2 over the same distance (Fig.4.20).

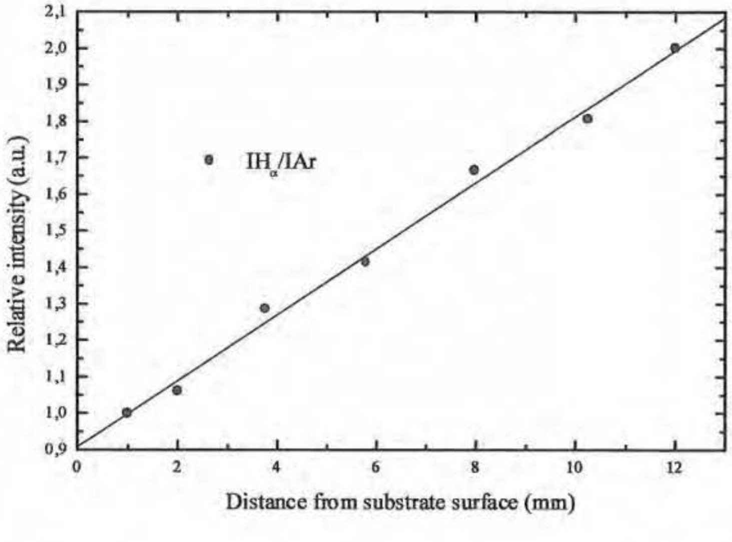

Figure 4.20: Evolution of the relative atomic hydrogen concentration as a function of the distance from the substrate surface.

The ICH(431.4 nm)/IH$_\alpha$ and IC$_2$(516.5 nm)/IH$_\alpha$ ratios increase in an exponential way with the distance from the substrate surface (Fig.4.21). The ICH(431.4 nm)/IH$_\alpha$ ratio increases with a factor 1.5 while the IC$_2$(516.5 nm)/IH$_\alpha$ ratio increases with a factor 2.3 between 0 mm and 11 mm from the substrate surface. On the other hand, the ICN(388.3 nm)/IH$_\alpha$ ratio decreases over the same interval. Most of the fall in the relative concentration of CN occurs within a 2 mm distance, after which the relative concentration of CN tends to decrease more gradually.

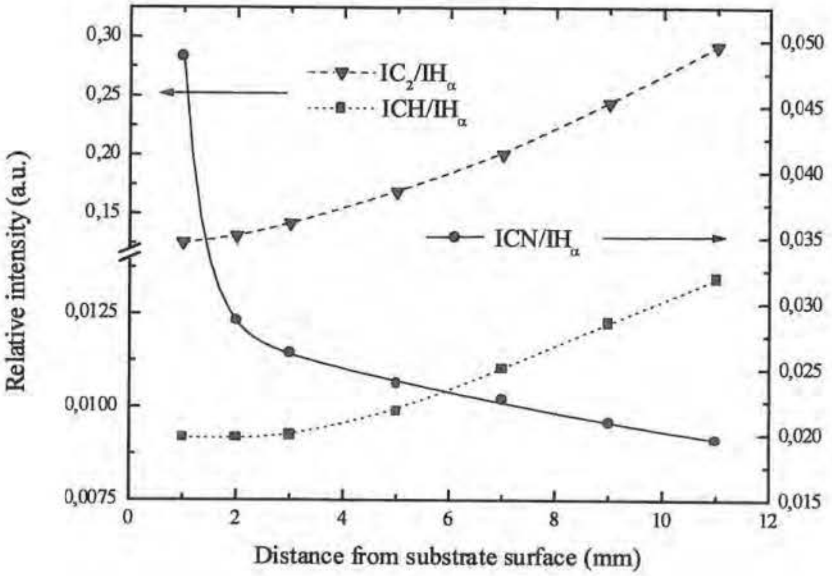

Figure 4.21: Evolution of the relative concentration of CH, C$_2$, and CN as a function of the distance from the substrate surface.

The ICN(388.3 nm)/IC$_2$(516.5 nm) and ICH(431.4 nm)/IC$_2$(516.5 nm) ratios decays in an exponential way from the substrate surface to the bulk of the plasma (Fig.4.22).

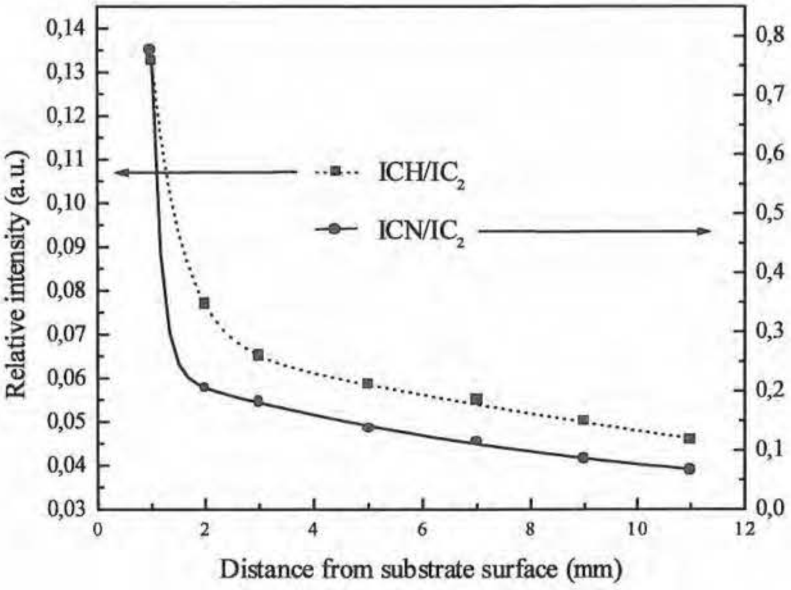

Figure 4.22: Evolution of the ICN(388.3 nm)/IC$_2$(516.5 nm) and ICH(431.4 nm)/IC$_2$(516.5 nm) ratios as a function of the distance from the substrate surface.

Fig.4.21 and Fig.4.22 suggest that the CN radicals are formed preferentially at or close to the substrate surface, since the relative concentration of CN decreases with the distance from the substrate surface. It seems therefore that there exits a dual reaction path leading to the formation of CN, one involving bulk plasma reactions, the other substrate surface reactions. This hypothesis is also supported by Chatei *et al.* [66].

To verify this assumption, the following experiment is carried out. In a first step, to be completely certain that the only source of carbon is coming from the feed gas, the reaction chamber is entirely freed of any carbon contaminant. The relative concentration of the CN radical in a CH_4 (4.8 %) - H_2 - N_2 (475 ppm) plasma is then monitored 2 mm above a clean silicon substrate. At $t = t_0$, the methane flow is shut down, and the CN intensity is monitored as a function of time (t). As shown in Fig.4.23, the ICN(t_0)/ICN(t) ratio decreases in an exponential way to zero with increasing time. The relaxation process takes about 50 s. The relative concentration of CH and C_2 follows the same behaviour, with a decay time of about 30 s. This experiment shows that the CN radical is produced within the plasma and that its relative concentration depends on the amount of methane present into the feed gas.

If the same experiment is conducted in the presence of a small graphite substrate, the relaxation time remains approximately the same (50 s), but the relative concentration of CN relaxes to about 1/10 of its initial value (Fig.4.23). This means that the fraction of graphite that is etched away by atomic hydrogen and/or atomic nitrogen is large enough to sustain the production of CN radicals. The intensity of the C_2 emission band due to the etching processes corresponds to an equivalent CH_4 fraction of about 1 vol.% ± 0.2 % in pure hydrogen plasma. The carbon etching processes occurring at the substrate surface can explain why the relative concentrations of CH and CN are much larger near the substrate surface than in the bulk of the plasma.

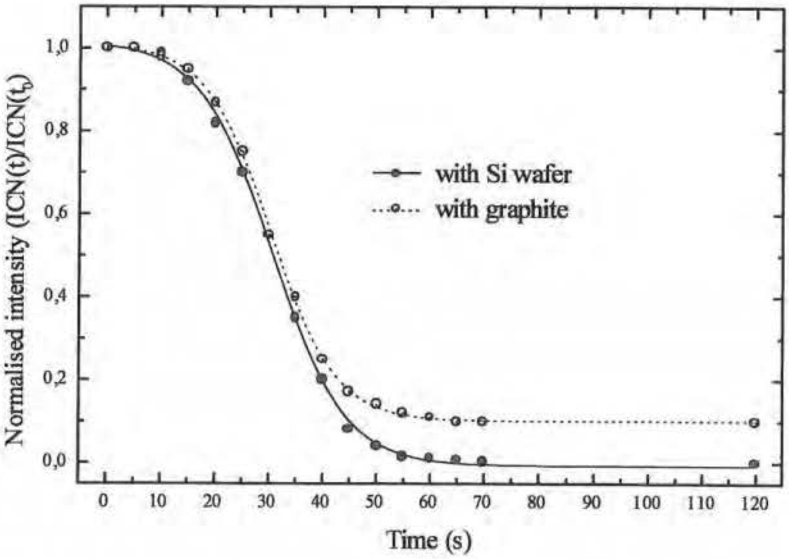

Figure 4.23: Evolution of the relative concentration of CN as a function of the elapsed time *t* after methane cut off (t_0).

As it can be seen from Fig.4.24, the increase in the temperature of hydrogen atoms *T(H)*, from 4750 K ± 570 K to 5275 K ± 630 K, occurs mainly at distances from the substrate comprised between 4 mm and 6 mm. On the other hand, the vibrational temperature of C_2 decreases from 4570 K ± 460 K to 4230 K ± 425 K over the same distance. The main loss in the vibrational temperature occurs in the same 2 mm interval too (Fig.4.25).

The region between 4 mm and 6 mm height corresponds precisely to the boundary between a dark violet plasma region in contact with the substrate surface and a light pink plasma region corresponding to the bulk colour of the plasma (Fig.4.26).

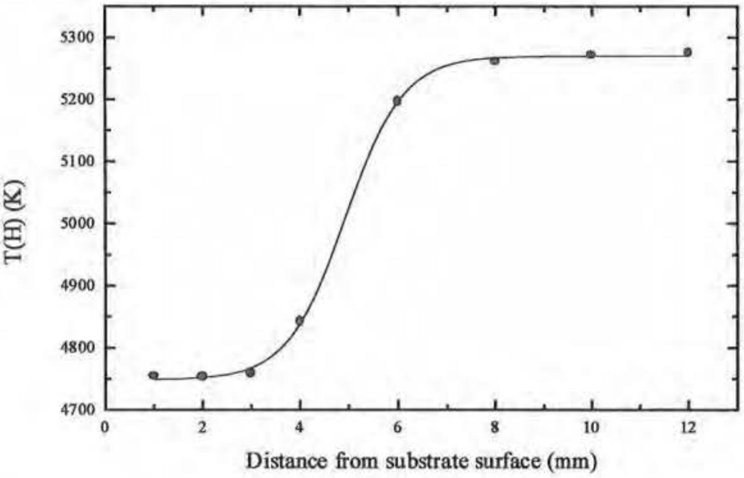

Figure 4.24: Evolution of the temperature of hydrogen atoms *T(H)* as a function of the distance from the substrate surface.

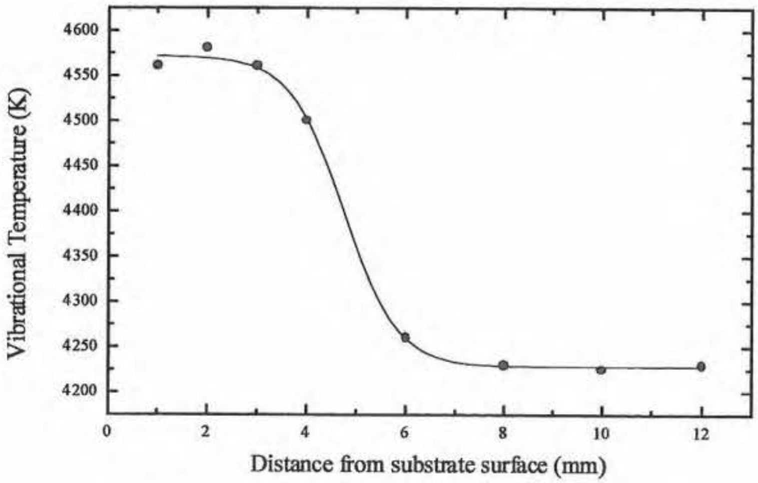

Figure 4.25: Evolution of the vibrational temperature of C_2 as a function of the distance from the substrate surface.

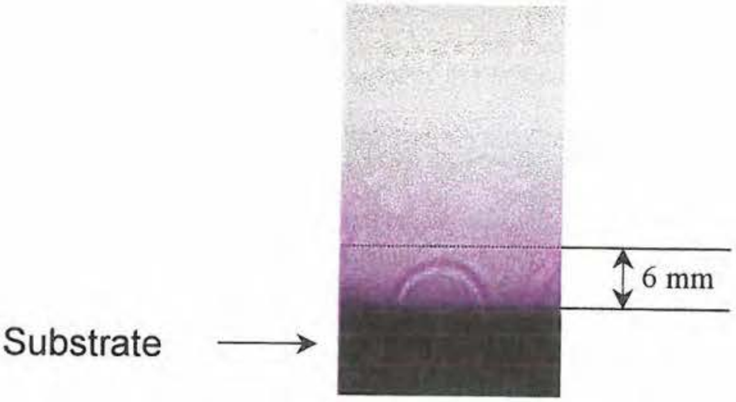

Figure 4.26: Picture of the plasma showing the change in colour of the plasma taking place between 4 mm and 6 mm above the substrate surface.

These results suggest that the plasma tends to thermalise near the substrate surface, as the atomic hydrogen and vibrational temperatures tend to equilibrate.

The relatively large difference between the calculated atomic hydrogen temperature and vibrational temperature in the bulk of the plasma (about 1000 K) could be linked to other competing de-excitation processes taking place preferentially in the bulk of the plasma. Amongst these non-spontaneous emission processes are collisional quenching and rotational and vibrational energy transfers. In particular, the rate of collisional quenching could be much larger in the bulk of the plasma than at the periphery of the plasma ball.

4.8 Conclusions

The use of Optical Emission Spectroscopy as-it allows only qualitative analysis of the emitting plasma species. As Optical Emission Spectroscopy needs an optical fibre to catch the light emitted by the source, the plasma is mainly seen as a whole by the optical system. Spatial resolution is therefore not conceivable, and little information but the bulk composition of the plasma, can be gained from such a system.

On the other hand, we showed that the use of a well characterised and simple optical system, combined with a series of assumptions allowing the use of elementary mathematical formulas, made it possible to increase the amount of information that could be obtained from a common emission spectrum. The home-made optical probe made it possible to confine the volume captured by the optical system and allowed therefore to record variations in the composition of the plasma as a function of the distance from the substrate surface. Simple assumptions on the physical chemistry of the plasma sustained by mathematical formulas made it possible to perform semi-quantitative analysis (actinometry) of the atomic hydrogen contained in the plasma. We showed how the plasma atomic hydrogen concentration and the CH, C_2 and CN radicals concentrations evolved as a function of the nitrogen content in the plasma as well as a function of the distance from the substrate surface.

Through a simple experiment, we showed that there are probably two pathways for the production of CN radicals in the plasma, one involving bulk plasma reactions, the other involving substrate surface reactions.

The temperature of hydrogen atoms along with the vibrational temperature of C_2 radicals were calculated, using the Boltzmann plot method, from the obtained optical emission spectra as a function of the nitrogen fraction in the plasma, and as a function of the distance from the substrate surface for a given nitrogen concentration. Both the Doppler broadening and the Boltzmann plot technique give temperature of hydrogen atoms that are in very good agreement. The higher temperature of hydrogen atoms values obtained by the Doppler broadening method can be related to the poor resolution of the monochromator. Without nitrogen, the difference between the vibrational temperature of C_2 (T_v) and the temperature of hydrogen atoms (T_H) is quite large (about 2300 K).

The difference between the vibrational and temperature of hydrogen atoms diminishes with the nitrogen fraction in the feed gas. For nitrogen contents larger than 475 ppm, the vibrational and temperature of hydrogen atoms are almost equal. This could suggest that the addition of minute quantities of nitrogen is responsible for the thermalisation of the plasma.

We also showed that the recorded variations in the composition and temperature of the emitting species could be correlated to the change in colour of the plasma ball in the vicinity of the substrate surface.

5. Characterisation of the diamond thin film

The depositions are carried out in an ASTeX PDS-17 Microwave (2.45 GHz - 5 kW) CVD system. The diamond thin films are deposited on Si (100) wafers using a methane (4.8 vol.%) - hydrogen gas mixture to which nitrogen is added in minute concentrations (0 - 1000 ppm in volume). The total gas mass flow is fixed at 210 sccm (standard cubic centimetre per minute). To enhance the nucleation density, the silicon wafers are abraded for 30 min on a vibrating plate covered with diamond powder (∅ = 0.1 µm). They are then rinsed twice with ethanol in an ultrasound bath.

The substrate temperature is monitored by an IR-pyrometer calibrated in function of the emissivity of diamond. The microwave power, vessel pressure and substrate temperature are set respectively at 3000 W, 11.5 kPa and 1100 K.

5.1 Characterisation techniques

The chemical bonding of various carbon allotropes varies in hybridisation from the sp^1 chain structure of carbyne to the sp^2-layered structure of graphite, to the sp^3 covalently bonded cubic structure of diamond. In addition, many disordered carbon forms consist most of the time of a mixture of various carbon hybrid bonds. This wide diversity of carbon forms makes the characterisation of diamond complicated. Consequently, numerous characterisation techniques have to be combined to analyse diamond films.

The diamond film morphology is examined by Scanning Electron Microscopy (SEM).

The evolution of the texture or preferred orientation of the diamond film is determined by X-ray diffraction (XRD). The T_{hkl} texture coefficients of the diamond film are calculated from the X-ray diffraction pattern obtained in the Bragg-Brentano geometry [95]. To gain a comparative figure on which to base changes in texture from sample to sample, the relative peak heights of all the *(hkl)* reflections compared with the standard intensity values are used. The experimental intensity values for each *(hkl)* reflection is determined as peak heights above background. The standard intensity values are determined for a randomly oriented

material. In our case, polycrystalline diamond powder is used as standard material. The expression of the T_{hkl} texture coefficient is as follow [96]:

$$\overset{*}{T}_{h'k'l'} = \frac{\overset{*}{I}_{h'k'l'} / I^{0}_{h'k'l'}}{(1/n)\sum_{0}^{n}(\overset{*}{I}_{hkl} / I^{0}_{hkl})} \qquad (Eq.5.1)$$

where $T^{*}_{h'k'l'}$ is the so-called texture coefficient for the reflection (*h'k'l'*), $I^{*}_{h'k'l'}$ is the $I_{h'k'l'}$ measured peak intensity for the reflection (*h'k'l'*) corrected for the film thickness ($I^{*}_{h'k'l'} = I_{h'k'l'}/Vl$), and $I^{0}_{h'k'l'}$ is the reference standard peak intensity for the reflection (*h'k'l'*). The term in the denominator represents an average over all observed (*hkl*) reflections of the ratio of the measured to the standard peak intensity values. The volume correction factor *Vl* is related to the film thickness by the following equation:

$$Vl = \frac{1}{2}\left\{1 - \exp(-\mu.t\frac{2}{\sin(\frac{2\Theta}{2})})\right\} \qquad (Eq.5.2)$$

with 2Θ being the diffraction angle, μ the mass absorption coefficient of diamond film for a copper cathode ($\mu = 4.6cm^2/g \times 3.515g/cm^3$) and *t* the thickness of the layer expressed in cm.

The diamond film quality is determined by Micro-Raman Spectroscopy [97, 98], using a 7-8mW Dilor Ar laser working at 514.5nm in a back scattering geometry with a spot size around 2 µm in diameter. In order to analyse the Raman data in a semi quantitative fashion, we adopt the Raman quality quotient Q_D defined as

$$Q_D = \frac{I_D}{I_D + I_G}, \qquad (Eq.5.3)$$

where I_D and I_G are, respectively, the relative intensities of the sp^3 *C* peak (at a Stokes shift of ~ 1332 cm^{-1}) and the sp^2 feature (centred at ~ 1550 cm^{-1}).

Based on repeated measurements on single samples, Wolden *et al.* [98] found that the accuracy of this parameter is around 20%.

The SIMS technique is used to determine the concentration of N, O, and H in the diamond films. The in-depth profiling is performed on a Cameca IMS-5f magnetic sector instrument. Nitrogen can most efficiently be detected by monitoring the CN^- ion under Cs^+ primary beam bombardment. The other ions (H^-, O^-, C^-, and C_2^-) are easily detected in the same conditions. The focused primary beam scans over a square surface of 200 µm x 200 µm while a field aperture in the spectrometer selected a central area of 55 µm in diameter where the ions are monitored. In this way, a crater is punched in the diamond film until the signal recorded for the species of interest does not evolve anymore as a function of the depth (approximately 200 nm).

Although no suitable standards of similar composition are available for the quantification of the SIMS data, the relative concentration of N, O and H are obtained by means of the ratios of CN^-, O^- and H^- intensities with respect to the C^- and C_2^- matrix signal. The measurement of the $^{12}C^{14}N^-$ ion (mass M = 26 a.m.u.) requires the use of high-mass resolution power in order to eliminate the mass interference of $^{13}C^{13}C^-$ ions ($\Delta(M) = 0.00364$ a.m.u.). Care has also been taken to reduce the hysteresis of the magnet during sequential mass switching. For the present analysis, all specimens are coated with a 20 nm vacuum evaporated gold layer (± 30 nm) in order to prevent local charging-up during the impact of the high-energy primary ions.

5.2 Effect of methane concentration on the growth of diamond films

The deposition conditions are summarised in Table 5.1.

Table 5.1: Deposition parameters for the methane–hydrogen plasma.

Microwave power	3000 W
Vessel pressure	11.5 kPa
Total gas flow	210 sccm
Methane percentage (in volume)	0-10 %
Substrate material	Si (100)
Substrate temperature	1000-1050 K

5.2.1 Effect on the growth rate

The diamond deposition rate increases rapidly from 0 μm/h to 0.65 μm/h for a methane fraction of respectively 0 vol.% to 5 vol.% and then decreases slowly with increasing methane content in the feed gas (Fig.5.1). At 10 vol.% CH_4, the growth rate decreases to approximately 0.4 μm/h.

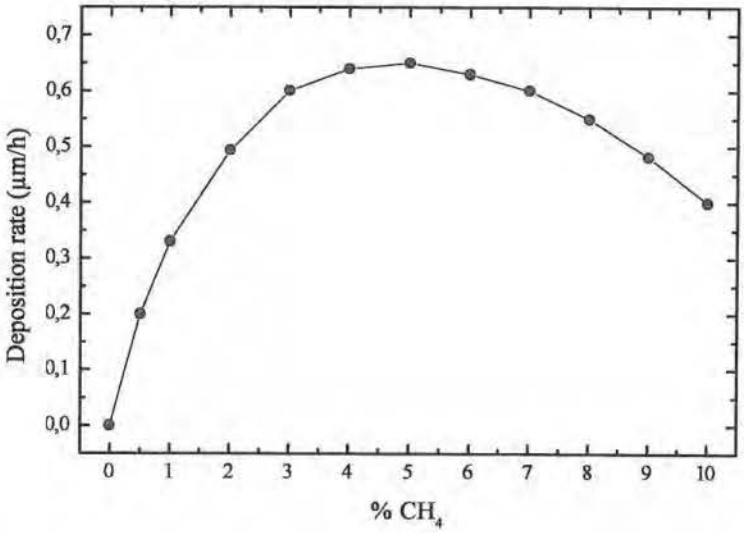

Figure 5.1: Evolution of the growth rate as a function of the methane fraction in the feed gas (Microwave power = 3000 W, P = 11.5 kPa, total gas flow = 210 sccm, substrate temperature = 1000 - 1050 K).

5.2.2 Effect on the film properties

The diamond films grow with a polycrystalline morphology up to about 8 vol.% CH_4. The films show a lot of "dimpled icosahedron" structures with numerous re-entry grooves. Above 8 vol.% CH_4, the film grows with a cauliflower morphology. The Raman quality of the deposited diamond films is rather good up to 5 vol.% CH_4, after which the diamond films turn black as they contain more and more graphite. The graphite phase at 10 vol.% CH_4 is sufficiently ordered to be identified by XRD. The decrease in the growth rate at high methane concentration is due to the increasing graphite content in the film, as graphite is etched away more efficiently as diamond by atomic hydrogen.

5.3 Effect of nitrogen addition on the growth of diamond films

The deposition parameters are summarised in Table 5.2

Table 5.2: Deposition parameters for nitrogen addition

Microwave power	3000 W
Vessel pressure	11.5 kPa
Total gas flow	210 sccm
Methane percentage (in volume)	4.8 %
Argon percentage (in volume)	3.8 %
Nitrogen content (in volume)	0-950 ppm
Substrate material	Si (100)
Substrate temperature	1000-1050 K

5.3.1 Effect on the growth rate

The diamond growth rate increases by about a factor 4.2 (from 0.6 µm/h to up to 2.5 µm/h) with the addition of only 95 ppm N_2 in the feed gas. The growth rate is stable up to 600 ppm N_2 (~ 2.6 µm/h) after which it decreases slowly together with increasing nitrogen fraction in the feed gas (Fig.5.2).

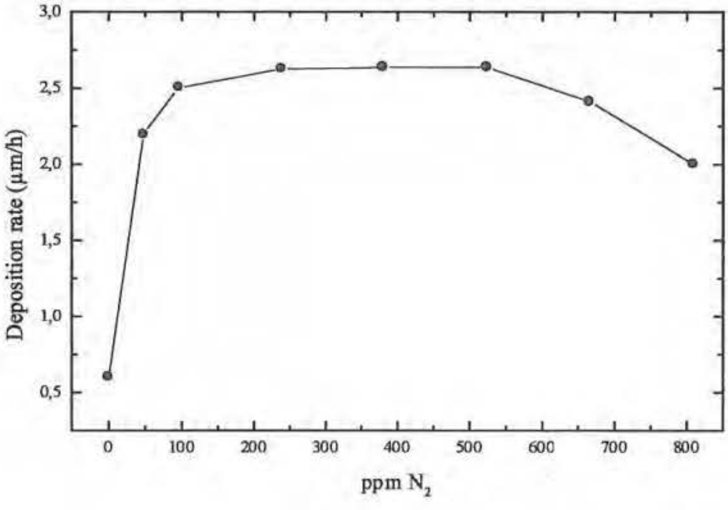

Figure 5.2: Evolution of the growth rate as a function of the nitrogen fraction in the plasma.

5.3.2 Effect on the film properties

Significant changes in the film morphology are observed when nitrogen is added to a conventional methane (4.8 vol.%)-hydrogen gas mixture (Fig.5.3 (a)-(j)).

Diamond films grown without nitrogen in a methane (4.8 vol.%)-hydrogen gas mixture consist of randomly oriented crystals with some 'dimpled' icosahedron structures present (Fig.5.3 (a)). Numerous re-entry grooves can also be observed.

The addition of 47.5 ppm N_2 is responsible for the development of {111} crystal facets inclined with respect to the substrate surface plane (Fig.5.3 (b)). At a concentration of 190 ppm N_2, the diamond film evolves towards a {111} crystal morphology (Fig.5.3 (d)). The development of {111} penetration twins on {111} surfaces leads to the growth of a {111} crystal morphology. Due to secondary twinning, smaller grain size are formed. Because the {111} twins are oriented with an angle of 15.8° with respect to their parent {111} facet [99], the final {111} morphology consists of crystals with the <100> direction almost perpendicular to the substrate surface. When nitrogen is added in larger amounts (237.5 ppm $< N_2 <$ 522.5 ppm), the diamond films develop with rough {100} crystal facets (Fig.5.3 (e)-(g)). Consequently, the number of {111} penetration twins on the {111} surfaces decreases. Above 665 ppm N_2, the diamond film grows with the typical 'cauliflower' morphology (Fig.5.3 (h)-(j)).

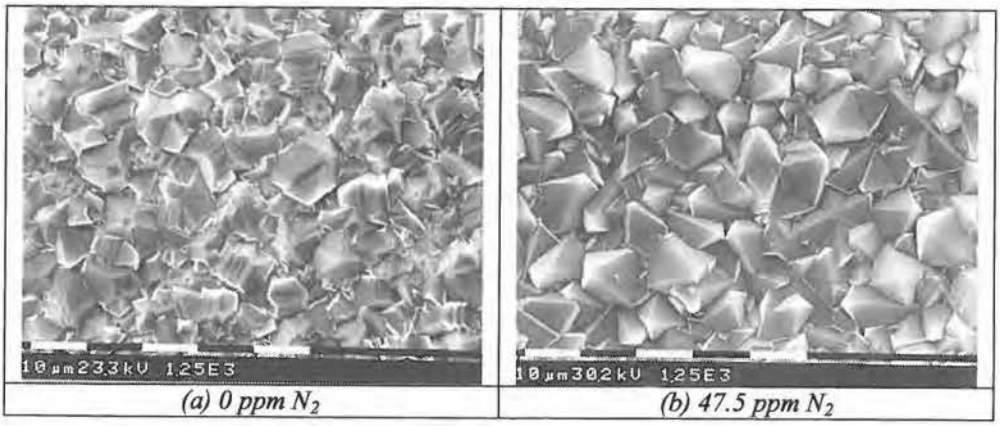

(a) 0 ppm N_2 *(b) 47.5 ppm N_2*

Figure 5.3: Evolution of the diamond film morphology as a function of the nitrogen fraction in a methane (4.8 vol.%)-hydrogen plasma.

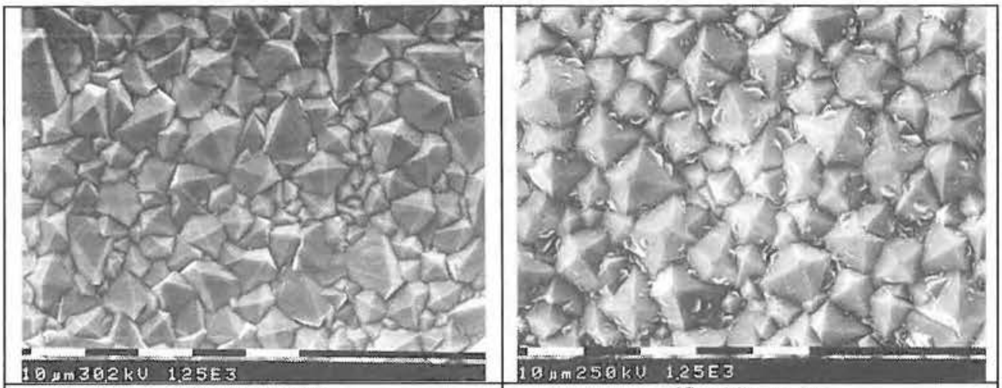

(c) 95 ppm N_2 *(d) 190 ppm N_2*

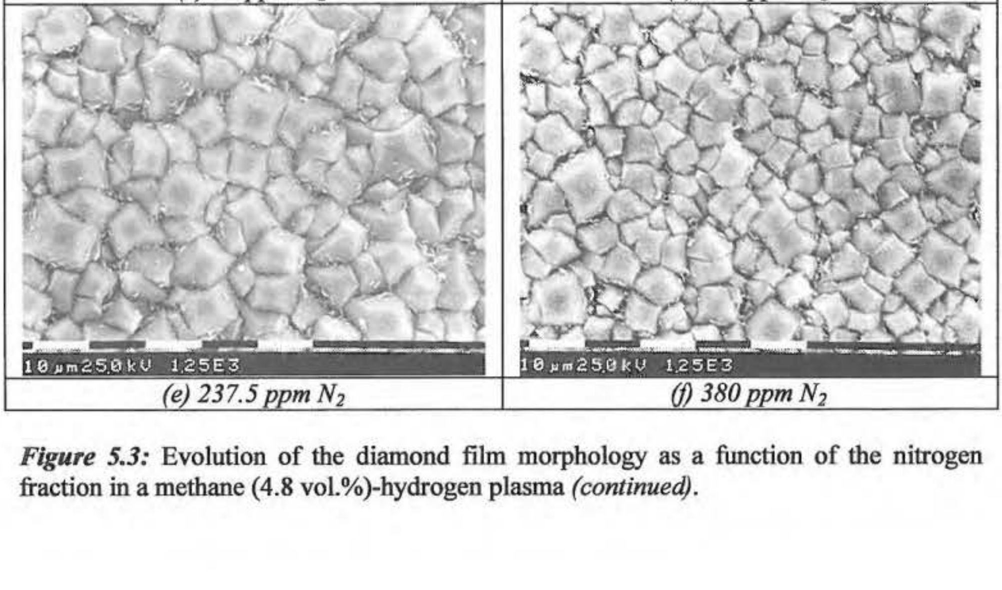

(e) 237.5 ppm N_2 *(f) 380 ppm N_2*

Figure 5.3: Evolution of the diamond film morphology as a function of the nitrogen fraction in a methane (4.8 vol.%)-hydrogen plasma *(continued)*.

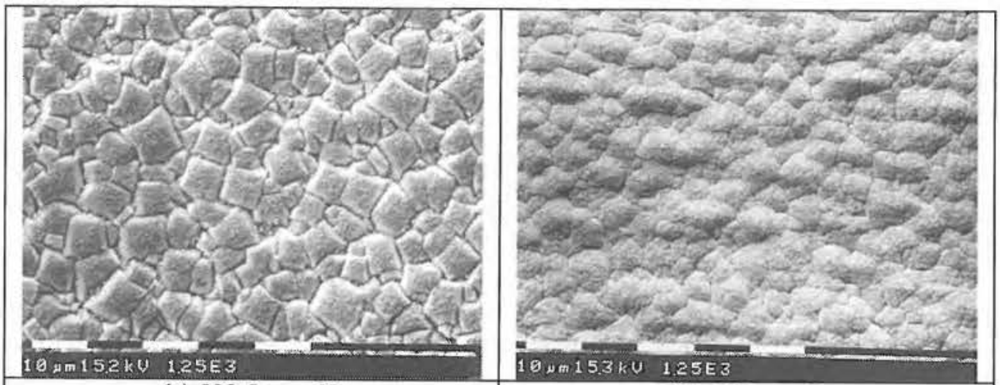

(g) 522.5 ppm N_2 *(h) 665 ppm N_2*

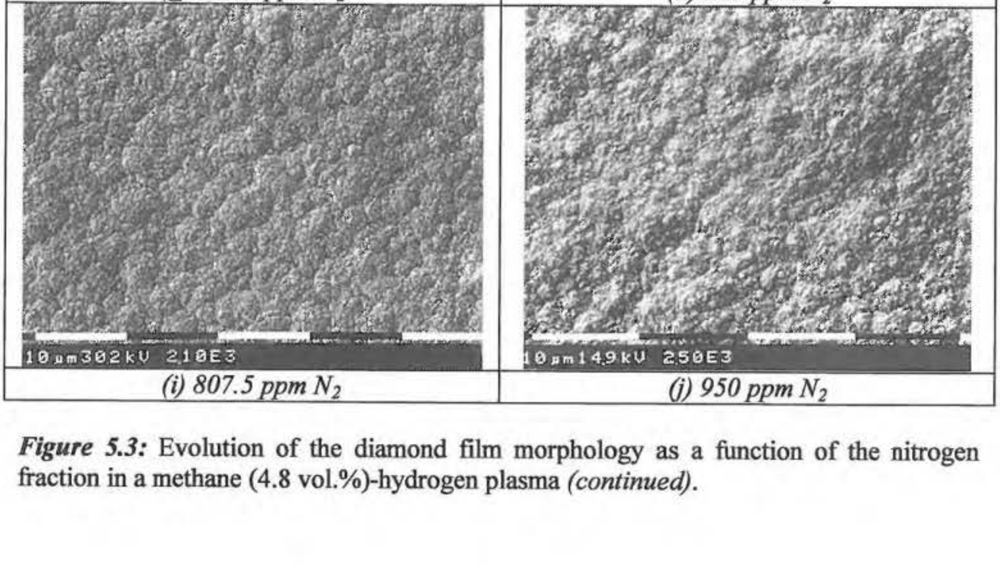

(i) 807.5 ppm N_2 *(j) 950 ppm N_2*

Figure 5.3: Evolution of the diamond film morphology as a function of the nitrogen fraction in a methane (4.8 vol.%)-hydrogen plasma *(continued)*.

Calculation of the texture coefficient from the XRD diffraction pattern (Fig.5.4) shows that the film evolves clearly towards a {100}-preferred orientation with the nitrogen content in the feed gas mixture.

Without nitrogen addition, the film has a slightly {110}-preferred orientation. The T_{220} texture coefficient is about twice as large as any other texture coefficient. It can be seen that the smallest texture coefficient is T_{400}. T_{331}, T_{111} and T_{311} lie between 0.5 and 1.25.

Around 100 ppm N_2, the T_{111} texture coefficient prevails. The value of T_{111} is about twice the value of the second largest texture coefficient, T_{311}. The value of the other texture coefficients, T_{220}, T_{400} and T_{331} are comprised between 0.25 and 0.5.

Above 200 ppm N_2, T_{400} is by far the most predominant preferred orientation of the diamond film. The other texture coefficient decreases rapidly towards the zero value.

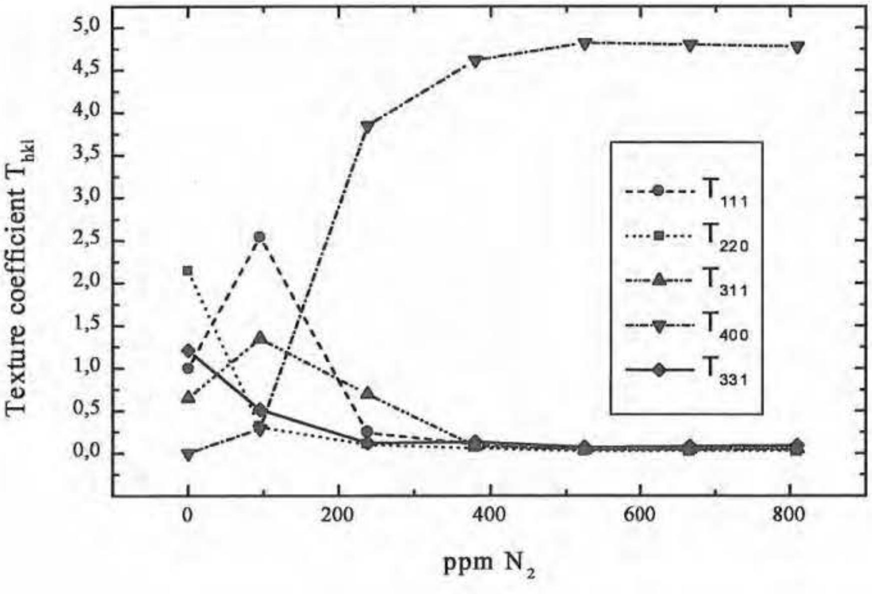

Figure 5.4: Evolution of the various T_{hkl} texture coefficients as a function of the nitrogen fraction in a methane (4.8 vol.%)-hydrogen plasma.

5.3.3 Effect on the quality of the film

If minute nitrogen addition to the feed gas mixture leads to some extent to an improvement in the diamond film texture, it also deteriorates the Raman quality of the deposited film (Fig.5.5). At low nitrogen content (< 190 ppm N_2), the Raman quality of the diamond films is rather good, with a high sp^3 content at 1332 cm^{-1} and a low sp^2 contribution in the region 1500 cm^{-1} – 1550 cm^{-1}. The intensity of the sp^3 feature at 1332 cm^{-1} decreases together with increasing nitrogen content in the process gases, while the graphitic sp^2 feature increases over the same concentration range.

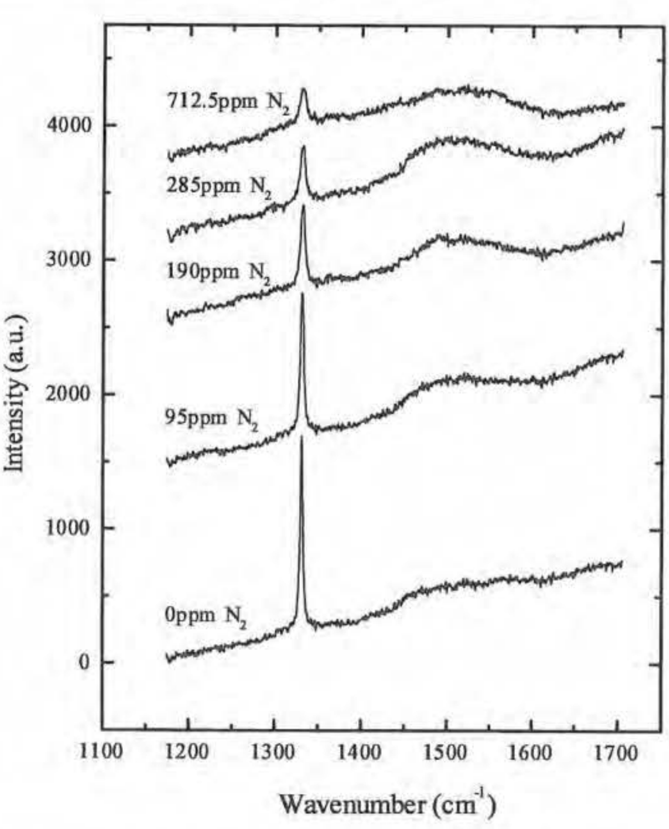

Figure 5.5: Raman quality of the diamond film as a function of the nitrogen content in a methane (4.8 vol.%)-hydrogen plasma.

Using the definition of Raman quality introduced previously, the Raman quality is plotted as a function of the nitrogen concentration in the feed gas mixture. Fig.5.6 shows that the Raman quality (Q_D) decreases in an exponential way from 0.3 to 0.06 in the 0 to 712.5 ppm N_2 range. These results are in agreement with the change of colour of the deposited films, which are turning black with increasing nitrogen fraction in the feed gas.

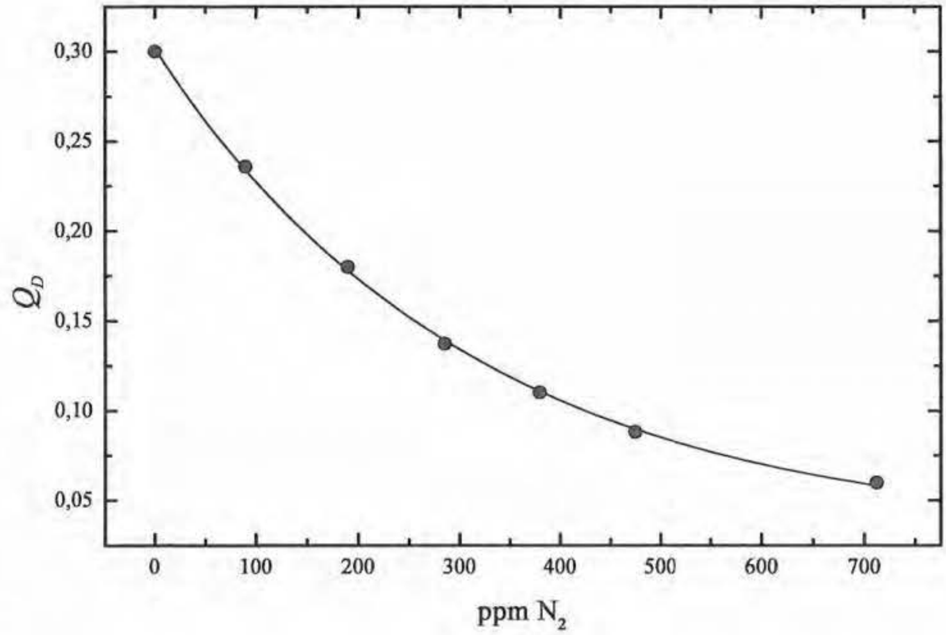

Figure 5.6: Raman quality (Q_D) as a function of the nitrogen content in the feed gas.

5.3.4 Effect on the SIMS composition of the film

The SIMS $[CN^-]/[C_2^-]$ and $[H^-]/[C_2^-]$ ratios increase linearly with the nitrogen content in the plasma (Fig.5.7). The nitrogen fraction in the film increases with an order of magnitude between 0 ppm and 600 ppm N_2, while in the same interval, the hydrogen content in the film increases by a factor 8. The other ratios of interest, $[C^-]/[C_2^-]$ and $[O^-]/[C_2^-]$, remain constant at respectively 0.75 and 0.12 throughout the studied domain.

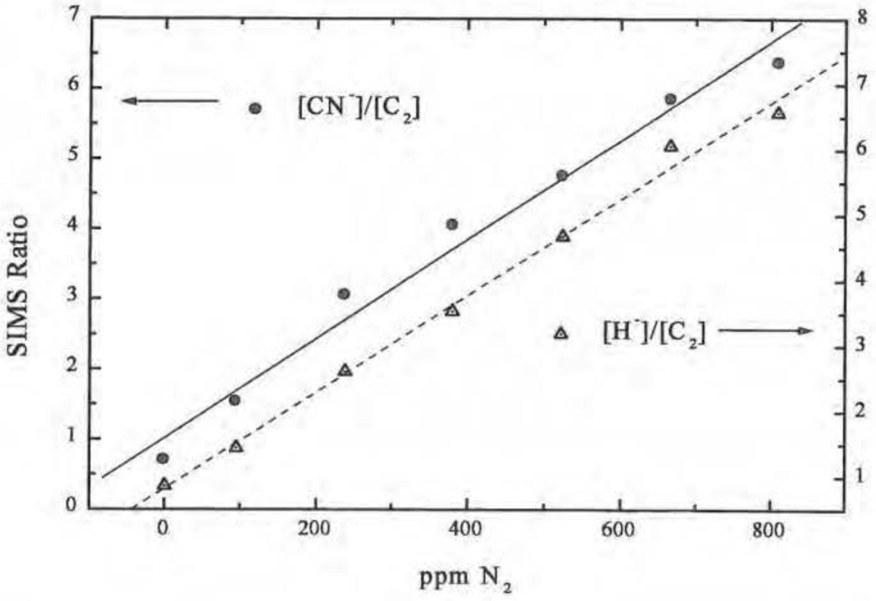

Figure 5.7: Evolution of the SIMS $[CN^-]/[C_2]$ and $[H^-]/[C_2]$ ratios as a function of the nitrogen content in a methane (4.8 vol.%)-hydrogen plasma.

These results show clearly that the H and N fraction in the film increase with the nitrogen fraction in the feed gas.

As the SIMS measurements give only a general overview of the evolution of the nitrogen content in the diamond film, it is impossible to know precisely where the nitrogen is incorporated into the film.

5.4 Conclusions

In this chapter we showed how the addition of minute amount of nitrogen to the gas phase could influence the growth of diamond films.

Nitrogen increased the growth rate by almost factor 4.5. Several possible explanations have been proposed. Bar-Yam and Moustakas [100] proposed a quasi-thermodynamic model on defect-induced stabilisation of diamond. This models predicts that the incorporation of nitrogen donors charges the vacancies in the growing diamond surfaces, reverses therefore the thermodynamic stability of diamond relative to graphite and thus enhance the growth rate of diamond. However it does not explain the orientation dependence of the increase in growth rates. In fact, the {110} and {111} surfaces incorporate more nitrogen than the {100} surface [58, 101]. According to the defect-induced model, a larger enhancement of growth rate would be expected for {110} and {111} surfaces rather than for the {100} surface, which is not what is observed.

Nitrogen drastically altered the morphology of the growing film. The diamond film evolved from polycrystalline non-oriented diamond films to the so-called cauliflower texture, through {111} and {100} well oriented textured diamond films.

X-ray diffraction spectra indicated that the film evolved towards a {100}-preferred orientation with increasing nitrogen content in the plasma.

On the other hand, micro-Raman measurements revealed that the diamond sp^3 content in the deposited film decreased together with the increasing concentration of nitrogen in the gas phase.

The SIMS measurements stressed out that the nitrogen fraction in the diamond film, increased with increasing nitrogen content in the gas phase. These results do not exclude that nitrogen can, together with the increasing nitrogen content in the gas phase, take an extending part in the graphitic phase [54-60].

6. Possible pathways for diamond growth

6.1 Diamond nucleation and growth

A conventional growth process in CVD of diamond films typically shows several distinguishable stages. Before nucleation starts, an incubation period may take from a few minutes up to hours, depending on the deposition parameters, the substrate material and the substrate pre-treatment. The individual 3-D nuclei formed on the substrate surface exhibit a sphere-like geometry. With increasing time, the nucleation density reaches a certain value where the surface nucleation stops. The isolated crystals grow homogeneously in size and facets develop due to abundant surface diffusion of carbon from the relatively large diamond-free area surrounding them. Finally, when the isolated crystals coalesce together, a continuous film is formed. Under certain growth conditions, the competition growth of crystals may govern the subsequent growth process of a continuous film. The grains increase in size and perfection with the direction of fastest growth nearly perpendicular to the substrate, leading to a columnar structure [102]. Based on the Van der Drift's principle of evolutionary selection [45], the crystals with the direction of fastest growth nearly perpendicular to the substrate are in the favour position and will survive (Fig.6.1). This principle governs the growth orientation, or texture, in vapour deposited films.

In a microwave plasma system, energy from the microwave electric field ionises the gas, which is primarily molecular hydrogen with small amounts of hydrocarbon, methane in our case. Energy is subsequently transferred from the electrons to vibrational levels of H_2. This vibrational energy then serves to heat the gas through vibration-to-translation energy transfer to atomic hydrogen and vibration-to-vibration or vibration-to-translation energy transfer to the other H_2 molecules [103]. Ion chemistry is important in these systems as an electron-loss source. Electron can dissociate H_2 and lead to a concentration of H^+ ions, which can undergo charge exchange with hydrocarbon, oxygen and/or nitrogen species. Neutral chemistry in the gas phase is also initiated by electron-impact dissociation of H_2, O_2 and hydrocarbons [102]. In microwave reactors, the dominating transport process is diffusion.

Figure 6.1: Columnar structure of the diamond growth film based on Van der Drift's principle of evolutionary selection [45].

The diffusion transport mechanism and geometry are often unique to a specific deposition technology, but common to most methods is a transport time much longer than the characteristic time for the hydrocarbons to react with hydrogen atoms. As a result, the reactants coupled by hydrogen transfer reactions rapidly equilibrate and their distribution depends directly on the atomic to molecular hydrogen ratio. Subsequent reactions among hydrocarbon species may be near or far from equilibrium depending upon pressure and residence time since hydrocarbon concentrations are quite low. The composition of the flux of species arriving at the deposition surface may differ from the bulk gas well away from the surface due to chemical reactions caused by temperature and concentration gradients. This simplistic overview of the deposition process is consistent with the in situ probing of the plasma by Optical Emission Spectroscopy.

Diamond nucleation on non-diamond surfaces without pre-treatment is usually too slow to obtain continuous films within reasonable time. Therefore, to significantly enhance the nucleation density and the growth rate, substrate pre-treatment is usually required. The most commonly used technique consists in scratching the substrate surface by an abrasive material. The mechanisms of nucleation enhancement by scratching are mainly due to the following reasons. Firstly, the seeding effect, as residues from polishing or abrading powders are left adherent or embedded in the polished surface, providing nucleation sites for diamond growth. Secondly, highly disoriented substrate surfaces or microscopic crater edge sites on the abraded surface create high-energy sites, which become preferred nucleation sites for diamond.

The surface chemical reaction mechanisms leading to diamond growth of diamond has been from the beginning the subject of much research, debate and controversy. Actually, a universally accepted diamond-growth reaction mechanism has still not been found yet. As an example, much controversy exists about the identification of the dominant precursor species leading to growth, although methyl radicals and acetylene molecules are the most predominant carbon containing species in most CVD growth systems. It is unlikely that there is a single and simple diamond mechanism that applies to all deposition systems and deposition conditions.

Elementary chemical reactions are used to describe the detailed step mechanisms and are the reactions used for kinetic calculations. An elementary reaction is defined as a one-step chemical transformation that proceeds via a single transition state.

Reactions involving atomic hydrogen seem to be a dominant factor in the chemistry of diamond CVD. They control not only the gas-phase chemistry, and thereby the nature of the reactive species reaching the growth surface, but also determine the availability of reactive sites upon the growth surfaces. In addition, the recombination of hydrogen on the surface is an important source of heat in the system, and must be accounted for in the substrate thermal management [4].

The selection of the chemical processes is judgmental and is based on our experience and on a wealth of literature on diagnostics and characterisation of various diamond CVD processes.

6.2 Gas phase reactions

OES measurements give a partial and truncated view of the plasma composition, as only emitting species can be identified. Moreover, the species that are identifiable are not the one commonly perceived to be responsible for diamond growth, such as CH_3 and C_2H_2.

Reactions of atomic hydrogen with hydrocarbon species and reactions among hydrocarbon species drive the subsequent gaseous chemistry. A schematic of the major elements of this complex mix of reactions is depicted in Fig.6.2, where reactions of larger than C_2 hydrocarbons are omitted.

A simplified reaction scheme is proposed in this section. Chemical reactions involving species with more than two carbon atoms are here not taken into account, firstly because they have little influence on the relative concentration of species containing one or two carbon atoms, and secondly because large carbon-containing species are not stable in an atomic hydrogen rich environment [35, 104]. The following reaction path is based on experimentally identified species and on the possible chemical reactions conducting to their formation and/or consumption in the gas phase.

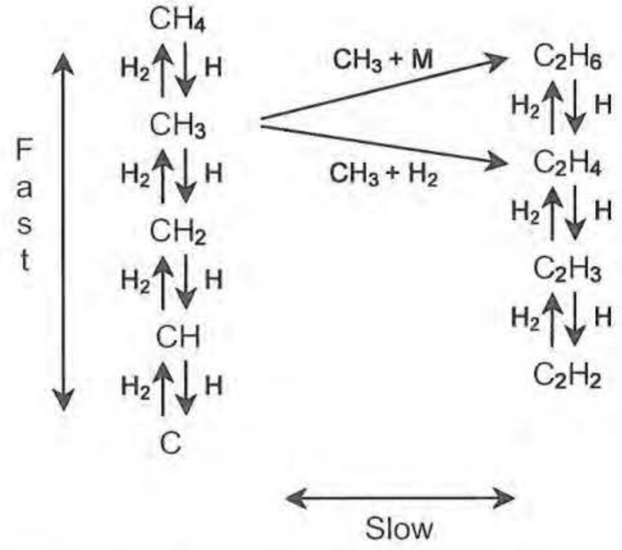

Figure 6.2: The principal gas phase reactions involve the rapid hydrogen transfer reactions amongst the C_1 and C_2 species, and to a lesser degree, the bimolecular hydrocarbon reactions forming C_2 and higher species (M = third-body) [105].

A simplified chemical reaction scheme conducting to the various plasma species is presented in Table 6.1 for conventional methane-hydrogen plasma. This simplified reaction scheme is compiled from reaction models developed by Baulch *et al.* [106], Frenklach *et al.* [36], Harris *et al.* [39, 107, 108] and Warnatz *et al.* [109].

Table 6.1: Simplified chemical reaction scheme for a CH_4-H_2 plasma, compiled from Baulch *et al.* [106], Frenklach *et al.* [36], Harris *et al.* [39, 107, 108] and Warnatz *et al.* [109].

$CH_2 = {}^3CH_2$
M = third-body, including electrons.

P(1) $2H + M \Leftrightarrow H_2 + M$
P(2) $H + CH \Leftrightarrow H_2 + C$
P(3) $H + CH_2 \Leftrightarrow H_2 + CH$
P(4) $H + {}^1CH_2 \Leftrightarrow H_2 + CH$
P(5) $H + CH_3 \Leftrightarrow H_2 + {}^1CH_2$
P(6) $H + CH_3(+M) \Leftrightarrow CH_4(+M)$
P(7) $H + CH_4 \Leftrightarrow H_2 + CH_3$
P(8) $CH_3 + M \Leftrightarrow H + CH_2 + M$
P(9) $C_2H_2 + M \Leftrightarrow H + C_2H + M$
P(10) $C + CH_3 \Leftrightarrow H + C_2H_2$
P(11) $H_2 + C_2H_2 \Leftrightarrow H + C_2H_2$
P(12) $C_2H_3(+M) \Leftrightarrow H + C_2H_2(+M)$
P(13) $CH + CH_3 \Leftrightarrow H + C_2H_3$
P(14) $H + C_2H_3 \Leftrightarrow H_2 + C_2H_2$
P(15) $CH + CH_4 \Leftrightarrow H + C_2H_4$
P(16) $CH_2 + CH_3 \Leftrightarrow H + C_2H_4$
P(17) $H + C_2H_4 \Leftrightarrow H_2 + C_2H_3$
P(18) $C_2H_5 \Leftrightarrow H + C_2H_4$
P(19) $H + C_2H_5 \Leftrightarrow 2CH_3$
P(20) $H + C_2H_5 \Leftrightarrow H_2 + C_2H_4$
P(21) $H + C_2H_6 \Leftrightarrow H_2 + C_2H_5$
P(22) ${}^1CH_2 + M \Leftrightarrow CH_2 + M$
P(23) $2CH_2 \Leftrightarrow H_2 + C_2H_2$
P(24) $2CH_2 \Leftrightarrow 2H + C_2H_2$
P(25) $2CH_3 \Leftrightarrow H_2 + C_2H_4$
P(26) $C_2H_6(+M) \Leftrightarrow 2CH_3 + M$

Reaction P(1), P(6), P(12), P(18) and P(26) are highly pressure sensitive.

When nitrogen is added to methane-hydrogen plasma, chemical reactions involving nitrogen-containing species have to be taken into account too. Observations on nitrogen containing plasma's by Chatei *et al.* [66, 67] and Vandevelde *et al.* [110-113] using Optical Emission Spectroscopy (OES) during microwave PA-CVD and by May *et al.* [64, 65] using Molecular Beam Mass Spectrometry (MBMS) during hot-filament PA-CVD are combined to build up a simplified reaction scheme. A combustion model developed by Miller *et al.* [25] is also used to determine the feasibility of the chemical reactions involving nitrogen and its derivatives.

Several reaction pathways can lead to the production of CN radicals in the plasma. May *et al.* [64, 65] suggest that the formation of methylamine, by the reaction of ammonia with methyl radicals, is a prerequisite for the formation of HCN molecules.

$$CH_3 + NH_3 \Leftrightarrow CH_3NH_2 + H \ \boldsymbol{P(27)}$$

$$CH_4 + NH_2 \Leftrightarrow CH_3NH_2 + H \ \boldsymbol{P(28)}$$

Reactions *P(27)* and *P(28)* are immediately followed by the fast conversion of methylamine into HCN:

$$CH_3 - NH_2(+M) \Leftrightarrow CH_2 = NH + H_2 \ \boldsymbol{P(29)}$$

$$CH_2 = NH(+M) \Leftrightarrow HC \equiv N + H_2 \ \boldsymbol{P(30)},$$

with M being a third-body.

These two last reactions are the most likely on thermodynamic grounds due to the stability of the $C \equiv N$ bond (Table 6.2), though they showed by MBMS that the prevalent N-containing species in the plasma is NH_3, and not HCN.

A prerequisite to the methylamine pathway is the dissociation of the N_2 molecule and the formation of NH_y species.

Miller *et al.* [25] proposed in their model a set of chemical reactions that can lead to the dissociation of N_2 by reaction with H atoms, and the formation of NH_2 and NH_3 radicals.

$$N_2 + H \Leftrightarrow NNH \ \boldsymbol{P(31)}$$

$$NNH + H_2 \Leftrightarrow N_2H_2 + H \ \boldsymbol{P(32)}$$

$$N_2H_2 + H \Leftrightarrow NH_2 + NH \ \boldsymbol{P(33)}$$

$$NH_i + H_2 \Leftrightarrow NH_{i+1} + H \ \boldsymbol{P(34)}.$$

Table 6.2: Bond dissociation energies [114-116]

Bond	Bond strength ($kJmol^{-1}$)
$H-H$	435
$N-N$	163
$N=N$	418
$N\equiv N$	945
$C-H$	411
$C-C$	345
$C=C$	602
$C\equiv C$	838
$H-N$	386
$H-NH_2$	442
$H-CH_3$	435
$H-CN$	531
$C-N$	304
$C=N$	615
$C\equiv N$	887

Another reaction pathway leading to the formation of HCN is a pathway involving N_2 and proposed by Walch *et al.* [117]

$$CH + N_2(+M) \Leftrightarrow HCN_2(+M) \quad \boldsymbol{P(35)}$$
$$HCN_2 \Leftrightarrow HCN + N \quad \boldsymbol{P(36)}.$$

Miller *et al.* [25] proposed in his combustion model additional chemical reactions involving N_2 too:

$$CH_2 + N_2 \Leftrightarrow HCN + NH \, \boldsymbol{P(37)}$$
$$CH_2 + N_2 \Leftrightarrow H_2CN + N \quad \boldsymbol{P(38)}$$
$$C + N_2 \Leftrightarrow CN + N \quad \boldsymbol{P(39)}$$

where reactions *P(38)* and *P(39)* are prevailing on reaction *P(37)*.

Reactions involving atomic nitrogen are also a possible pathway for the formation of CN radicals. Energy is probably transferred from electrons and/or excited atoms and molecules leading to the formation of an excited N_2 state that can undergo dissociation more readily:

$$N_2 + Y^* \Leftrightarrow N_2^* + Y \quad \boldsymbol{P(40)}$$
$$N_2^* + Y^* \Leftrightarrow 2N + Y \quad \boldsymbol{P(41)}$$

with *Y* being an electron or a third-body.

Therefore, chemical reactions conducting to the formation of CN radicals and involving nitrogen atoms have to be taken into account too, as microwave plasmas are enough energetic to dissociate N_2.

According to Miller *et al.* [25], HCN molecules can also be favourably produced by the reaction with methyl radicals:

$$CH_3 + N \Leftrightarrow H_2CN + H \quad \boldsymbol{P(42)}$$
$$H_2CN + M \Leftrightarrow HCN + H + M \quad \boldsymbol{P(43)}.$$

The chemical reactions *P(27)* to *P(39)* are all possible pathways conducting to the formation of HCN molecules, since each (hydro-) carbon containing radical taking part in the production of HCN is present in common CH_4–H_2 plasma (Table 6.1).

Most of the processes involved in this series of chemical reactions conducting to the formation of CN are not consuming hydrogen atoms. Only the methylamine pathway is consuming hydrogen atoms as prerequisite to the formation of NH_2 and NH_3 radicals.

The OES analysis of our microwave plasma showed that the relative concentration of atomic hydrogen, CH and C_2 in the plasma increases with the nitrogen fraction in the feed gas. The relative concentration of H_2 seemed on the contrary to decrease with increasing nitrogen content in the plasma. Once formed, CN could act as a very effective catalyst, abstracting hydrogen atoms from molecules and radicals and releasing them back to the plasma in a continuous cycling process (reactions *P(44)* to *P(46)*).

$$CH_i + CN \Leftrightarrow CH_{i-1} + HCN \quad \boldsymbol{P(44)}$$
$$H_2 + CN \Leftrightarrow H + HCN \quad \boldsymbol{P(45)}$$
$$HCN + M \Leftrightarrow CN + M + H \quad \boldsymbol{P(46)}$$

CN radicals seem to be stable radicals in the plasma undergoing little chemical transformations. The small chemical reactivity of the CN radicals was also observed by May *et al.* [64, 65], who showed that for HCN-H_2 gas mixtures, 75 % to 85 % of the nitrogen is locked up as non-dissociated HCN. This is probably linked to the extremely high strength of the $C \equiv N$ bond.

In our plasma's, nitrogen was only identified as being part of the CN radical. As only emitting species are detected by OES, it is not possible to relate for the presence of other N-containing species in the plasma, which cannot be ruled out. Bohr *et al.* [62] showed, by thermodynamic equilibrium calculations, that most of the nitrogen is locked up as HCN, N_2 and CN, and to a lesser extend as C_2N. May *et al.* [64, 65], using MBMS in a hot-filament reactor, showed that for $N_2 : CH_4$ 1 : 1 hydrogen gas mixtures that most of the nitrogen is trapped as HCN and NH_3, with NH_3 being the prevalent N-containing species in the plasma. Chatei *et al.* [66, 67], using electrically pulsed microwave discharges, reported the presence of both CN and NH in their N-containing plasma by OES. All presented results showed that, according to the initial activation technique, many N-containing species could participate to the plasma chemistry.

6.3 Substrate surface reactions

Review of available literature shows that theoretical modelling of the kinetic aspects of diamond nucleation is scarce and generally does not involve the events taking place during the initial stage of nucleation. The kinetics of impingement, adsorption and surface diffusion of adatoms, as well as the formation of intermediate carbonaceous phases has not been considered in these studies, nor has the competition of the carbide formation with diamond nucleation for the carbon species been treated.

Moreover, most of the diamond growth models have been developed by fitting the model to experimental data, which are highly system or experiment dependent.

Generally accepted chemical mechanisms that lead to low-pressure growth of diamond are therefore still lacking.

One-dimensional growth models, elaborated mainly by Badzian *et al.* [35], Frenklach *et al.* [36, 37], Dandy *et al.* [26, 38] and Harris *et al.* [39, 40], have been useful for verifying proposed growth mechanisms. However, these models typically consider the kinetics of only one diamond growth mechanism, and do not explicitly account for competing mechanisms or the effect of surface atomic structure and morphology on growth behaviour. Three-dimensional atomic-scale simulations of diamond growth have been performed recently by Dawnkaski *et al.* [33], but were limited to growth at particular surface configurations on the {100} diamond surface.

Lately, Battaile *et al.* [41] introduced a more realistic three-dimensional simulation method based on a rigid three-dimensional lattice capable of simulating hours of growth under most CVD conditions and on virtually any surface. This model has the particularity to describe the growth of diamond by a series of chemical reactions involving methyl radicals and acetylene molecules on both graphite and diamond growing surfaces. Methyl radicals and acetylene are found to be the most predominant carbon-containing precursors detected in the vicinity of the substrate in diamond growth experiments.

Table 6.3 summarises the presumed chemical reactions involved in the diamond growth process for (hydro) carbon-hydrogen containing plasma [26, 40, 118].

Table 6.3: Reactions leading to the growth of diamond for a (hydro-) carbon-hydrogen containing plasma [26, 40, 117].

C_d = diamond sp^3 dangling bond
C_g = graphite sp^2 bond
dimer = dimer bond

1. $C_d\text{-}H + H \Leftrightarrow C_d + H_2$
2. $C_d + H \Leftrightarrow C_d\text{-}H$
3. $C_d + CH_3 \Leftrightarrow C_d\text{-}CH_3$
4. $C_d + C_2H_2 \Leftrightarrow C_d\text{-}C_2H_2$
5. $C_d\text{-}CH_2 + H \Leftrightarrow C_d + CH_3$
6. $C_d\text{-}CH_y + H \Leftrightarrow C_d\text{-}CH_{y-1} + H_2$
7. $C_d\text{-}CH_y + H \Leftrightarrow C_d\text{-}CH_{y+1}$
8. $C_d\text{-}C_2H_y + H \Leftrightarrow C_d\text{-}C_2H_{y-1} + H_2$
9. $C_d\text{-}C_2H_y + H \Leftrightarrow C_d\text{-}C_2H_{y+1}$
10. $C_d\text{-}C_2H_y + H \Leftrightarrow C_d\text{-}CH_{y-2} + CH_3$
11. $C_d\text{-}CH_y + CH_3 \Leftrightarrow C_d\text{-}C_2H_{y+3}$
12. $C_d\text{-}C_d \Leftrightarrow C_d + \text{dimer} + C_d$
13. $C_d + \text{dimer} + C_d\text{-}C_xH_y \Leftrightarrow C_d + C_d\text{-}C_{x-1}H_y + H_2$
14. $C_d\text{-}C_d\text{-}H + H \Leftrightarrow C_d\text{-}C_d + H_2$
15. $C_d\text{-}C_d + H \Leftrightarrow C_d\text{-}C_d\text{-}H$
16. $C_d\text{-}C_d\text{-}CH_2 + H \Leftrightarrow C_d\text{-}C_d + CH_3$
17. $C_d\text{-}C_d + CH_3 \Leftrightarrow C_d\text{-}C_d\text{-}CH_3$
18. $C_g\text{-}H + H \Leftrightarrow C_g + H_2$
19. $C_g + H \Leftrightarrow C_g\text{-}H$
20. $C_g\text{-}CH_2 + H \Leftrightarrow C_g + CH_3$
21. $C_g + CH_3 \Leftrightarrow C_g\text{-}CH_3$
22. $C_g + C_g + H \Leftrightarrow C_d + C_d\text{-}H$

The growth of diamond by CVD processes occurs by the evolution and incorporation of chemisorbed species on a surface. Diamond is usually grown in an atmosphere containing H, H_2 and various hydrocarbon species. Under typical growth conditions, a passivating layer of H atoms largely covers the diamond surface. Surface sites can be activated by either H desorption or abstraction. Once a diamond surface is active, it can be repassivated either by an H atom or a (hydro-) carbon molecule. A chemisorbed hydrocarbon might either desorb, returning to the gas phase and reactivating consequently the surface sight, or it might be incorporated into the film by subsequent surface reactions leading to film growth.

A set of surface chemical reactions analogous to the one proposed by Bataille *et al.*, will be presented in an attempt to account for the effect of nitrogen on the substrate surface chemistry.

Nitrogen presents numerous similarities with the physical properties of carbon atoms as both are found in adjacent columns in the Mendeleev's periodic table of the elements. The radius of the N and C atom are very close (C: 0.077 nm, N: 0.074 nm). In addition, the bond lengths in normal covalencies of C-N bonded species are close to those of C-C bonded species (Table 6.4). Both atoms also form the same kind of hybrid orbitals (i.e. sp, sp^2 and sp^3), and the bond angle $C-N-C$ in trimethylamine is 109°, a value very close to the $H-C-H$ bond angle 109.5° in methane.

Table 6.4: Bond lengths in normal covalencies (in nm) [119]

$C-C:0.1537$	$C-N:0.1472$	$N-N:0.1451$
$C=C:0.1335$	$C=N:0.129$	$N\equiv N:0.123$
$C\equiv C:0.1202$	$C\equiv N:0.1157$	$N\equiv N:0.1098$

These informations suggest that N-containing species can undergo the same sort of chemical reactions at the growing surface as the C-containing species, and hence be incorporated in the diamond lattice as a single substitutional species.

A prerequisite for the nucleation and growth of diamond films is the generation of active sites at the growing surface. To generate active sites, hydrogen atoms have to be removed from the growing surface. This process can be accomplished by impingement of H atoms on the substrate surface, liberating H_2 in the gas phase.

$$C_d - H + H \Leftrightarrow C_d + H_2 \ \boldsymbol{S(1)}$$

Other molecules and radicals present at the vicinity of the substrate surface can play a similar role. Abstraction of H atoms by CH_y radicals is another possible reaction path, though probably minor since the reaction balance is not largely in favour of the end products.

$$C_d - H + CH_y \Leftrightarrow C_d + CH_{y+1} \ \boldsymbol{S(2)}$$

Reaction paths involving C atoms can also occur, though in hydrogen saturated plasma, they would first be more likely transformed in CH radicals.

More plausible reaction paths are paths involving H-atom abstraction from the substrate surface by N-containing compounds. Abstraction by CN radicals is an extremely favourable process (Table 6.2), since the newly formed H-CN bond is much more stable than the broken one [54].

$$C_d - H + CN \Leftrightarrow C_d + HCN \ \boldsymbol{S(3)}$$

Reactions involving NH_y species can also create active sites at the growing surface. They are thermodynamically favoured, as the newly created bond has a larger energy as the broken one too (Table 6.2).

$$C_d - H + NH_y \Leftrightarrow C_d + NH_{y+1} \quad \mathbf{\mathit{S(4)}}$$

Other N-containing species, such as N_2H radicals could also participate in the H abstraction process.

$$C_d - H + N_2H \Leftrightarrow C_d + N_2H_2 \quad \mathbf{\mathit{S(5)}}$$

Another important step in diamond growth is the removal of non-diamond species by atomic hydrogen.

$$C_s - CH_y + H \Leftrightarrow C_s + CH_{y+1} \quad \mathbf{\mathit{S(6)}}$$

with C_s being any surface carbon atom, C_d or C_g.

This step could as well be accomplished by other species, such as N atoms [54]

$$C_s - CH + N \Leftrightarrow C_s + HCN \quad \mathbf{\mathit{S(7)}}$$

or NH radicals

$$C_s - C + NH \Leftrightarrow C_s + HCN \quad \mathbf{\mathit{S(8)}}.$$

These three last reactions could be responsible for the observed increase in the CN and CH relative concentrations at the vicinity of the substrate surface during our OES spatial measurements.

In addition, nitrogen dissociation could occur more efficiently at the substrate surface, the growing surface acting as a catalyst for the dissociation of N_2. This factor could increase locally at the substrate surface the concentration of atomic nitrogen and consequently favour reactions involving N atoms.

The fact that nitrogen addition in the plasma increases the growth rate is quite straightforward since it was shown that nitrogen increases the total number of available reactive carbon containing species in the plasma. CN, as well as C_2N [62] radicals could take an active part in diamond growth.

$$C_d + CN \Leftrightarrow C_d - CN \ \mathbf{S(9)}$$
$$C_d + C_2N \Leftrightarrow C_d - C_2N \ \mathbf{S(10)}$$

which could respectively yield by successive hydrogenation,

$$C_d - CN + 3H_2 \Leftrightarrow C_d - CH_3 + NH_3 \ \mathbf{S(11)}$$
$$C_d - C_2N + 2H_2 \Leftrightarrow C_d - C_2H + NH_3 \ \mathbf{S(12)}.$$

Moreover, to outline the growth of diamond, Rau *et al.* [120] proposed a model based on the incorporation of C_2H species. This model could as well be applied to the C_2N species.

Instead of dissociating, chemisorbed N_2 could also form bridge structures with the growing surface analogous to acetylene and being in this way incorporated as substitutional nitrogen in the diamond lattice:

$$C_d + C_d + N_2 \Leftrightarrow C_d - N = N - C_d \ \mathbf{S(13)}.$$

These bridge structures could accumulate preferentially in specific growth sectors, where the thermodynamics of the chemisorption process are favourable. The presence of these structures could enhance, slow down, or even prevent further growth along the concerned growth sector, leading to some preferential growth processes. Kawarada *et al.* [101] showed for instance that significantly larger nitrogen concentrations are found in {111} growth sectors relative to {100} growth sectors.

Further addition of H and/or CH_y radicals could lead to the cleavage of the $N = N$ double bond.

The C_2N species could also be incorporated,

$$C_d + C_2N \Leftrightarrow C_d - NC_2 \ \mathbf{S(14)}$$

and yield

$$C_d + C_2N \Leftrightarrow C_d - NH_3 + C_2H_2 \ \mathbf{S(15)}.$$

or as a single nitrogen atom: $C_d + N \Leftrightarrow C_d - N \ \mathbf{S(16)}.$

Understanding diamond nucleation and growth requires knowledge of common surface structures and growth sites for diamond. Faceted diamond crystallites are dominated by cubic {100} and octahedral {111} surfaces, and {111} twins planes and combinations of these [105]. Observations of {110} surfaces are much less common. The focus of the following discussion will be on the {111} diamond surfaces, since rate-limiting nucleation and/or growth processes are generally thought to occur on sites associated with the low index plane surfaces. Nucleation or growth of the next layer requires the incorporation of three carbon atoms on the (111) surface, for two on the (110) and only one on the (100).

Fig.6.3 shows one of the several possible nucleation kernels of a new layer on a perfect {111} surface through successive attachment of methyl radicals. The methyl radical is emphasised as the growth species because of the kinetic [105] and spectroscopic data indicating that at least a single carbon species is responsible for most of the carbon incorporated into the diamond lattice. Most of the steps in the proposed mechanism involve the easy hydrogen abstraction and re-attachment, the occasional chemisorption on the hydrocarbon species at a radical site, unimolecular desorption of hydrocarbon species singly bonded to the surface at higher temperatures, and easy radical-radical reactions on the surface. Fig.6.3 shows for example the possible pathway for the growth of the next layer on a {111} diamond surface in a methane-hydrogen plasma from CH_3 moieties. In a first step, hydrogen abstraction occurs at the unreconstructed diamond surface, resulting in the formation of a growth site. In the second step, a methyl moiety reacts at the growing site. Further successive hydrogen abstraction and methyl addition results in the incorporation of methyl groups at the growing interface. Once chemisorbed, the methyl moiety can undergo hydrogen abstraction too. The resulting methyl radical can react with another plasma methyl moiety to form an ethyl group after hydrogen abstraction. The ethyl moiety can undergo hydrogen abstraction to form an ethyl radical. This ethyl radical can (a) rearrange to a more stable moiety, or (b) undergo β-scission and liberate ethylene. If another methyl radical is present in the β position with respect to the ethyl moiety, both can react to form a bridge (Fig.6.4). Two outcomes are possible (Fig.6.5). In the first, the bridge can lead to the formation of a twin if a methyl radical of an adjacent hexane ring of the diamond lattice takes part in the elaboration of the next layer. In the second one, the bridge can lead to the formation of an island if a methyl radical originating from the same hexane ring of the diamond lattice participates to the next layer.

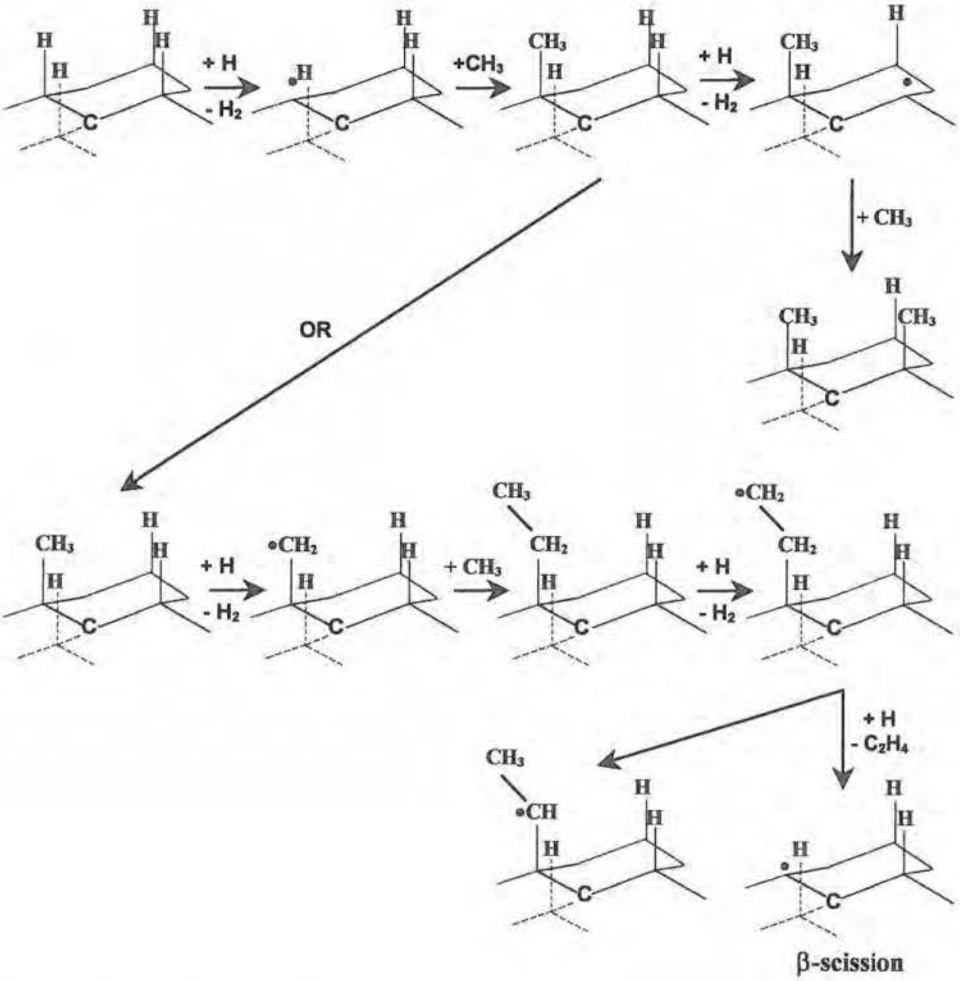

Figure 6.3: Growth on {111} surface from CH_3 (one carbon species) adapted from [105].

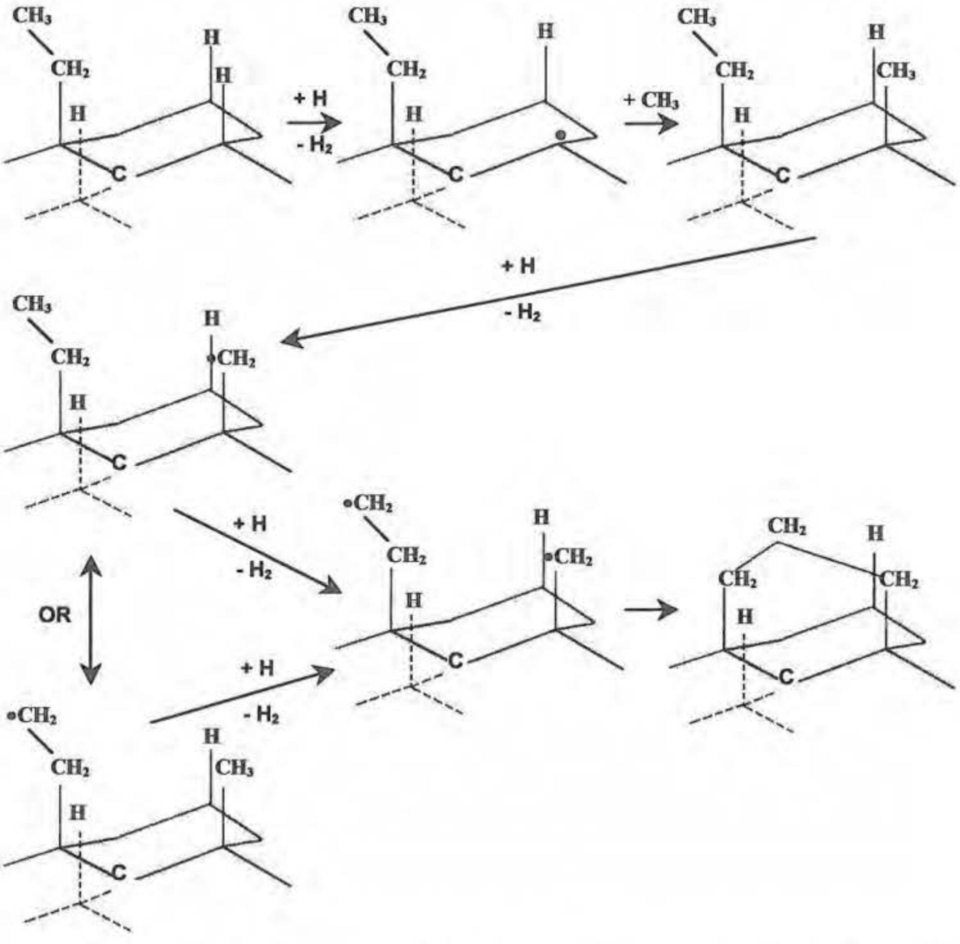

Figure 6.4: Growth on {111} surface from CH_3 (one carbon species) adapted from [105] (continued).

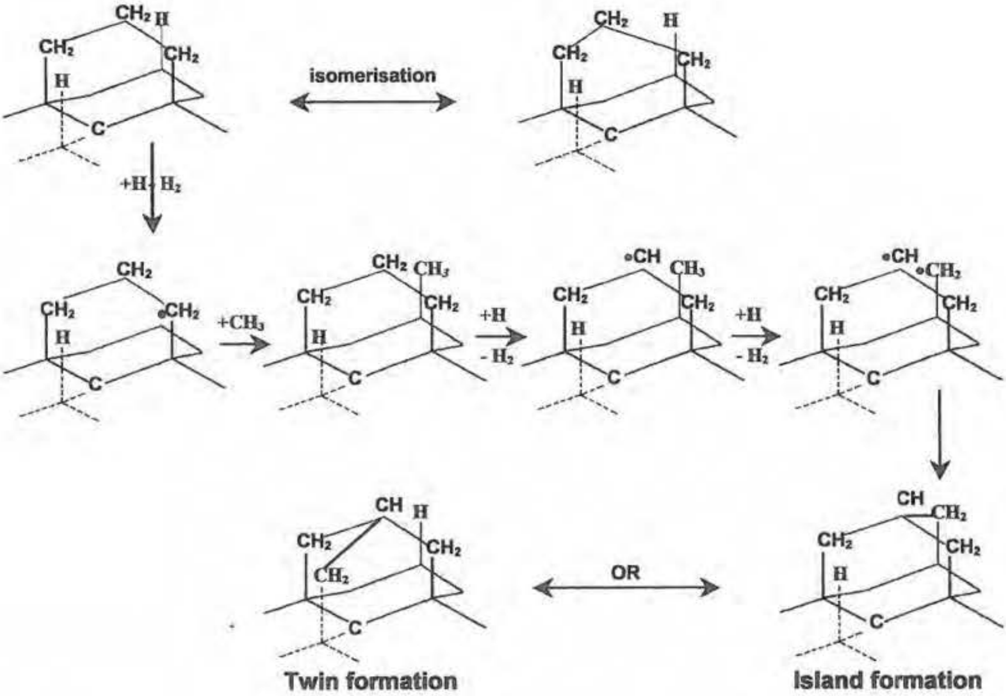

Figure 6.5: Next layer nucleation on {111} surface from CH_3 adapted from [105].

When nitrogen is present in the gas mixture, cyanide (CN) radicals are formed in the plasma. As emphasised earlier, these cyanide radicals can react at activated sites on the diamond surface in the same way as methyl moieties do. As shown in Fig.6.6, the CN radical can react at an active site and form stable bridge structures by reacting with other methyl radicals chemisorbed in the diamond lattice. The bridges can lead to the formation of twins or islands (Fig.6.7) depending on the origin of the methyl moiety that takes part in the development of the next layer of the diamond lattice. Compared to the methyl moiety, the cyanide moiety has the advantage that it cannot undergo β-scission reactions as there is no β-hydrogen atom present. This could mean that once chemisorbed, the cyanide radicals are more likely to remain incorporated in the diamond lattice. This factor could be responsible for the observed increase of the diamond growth rate during deposition with nitrogen addition.

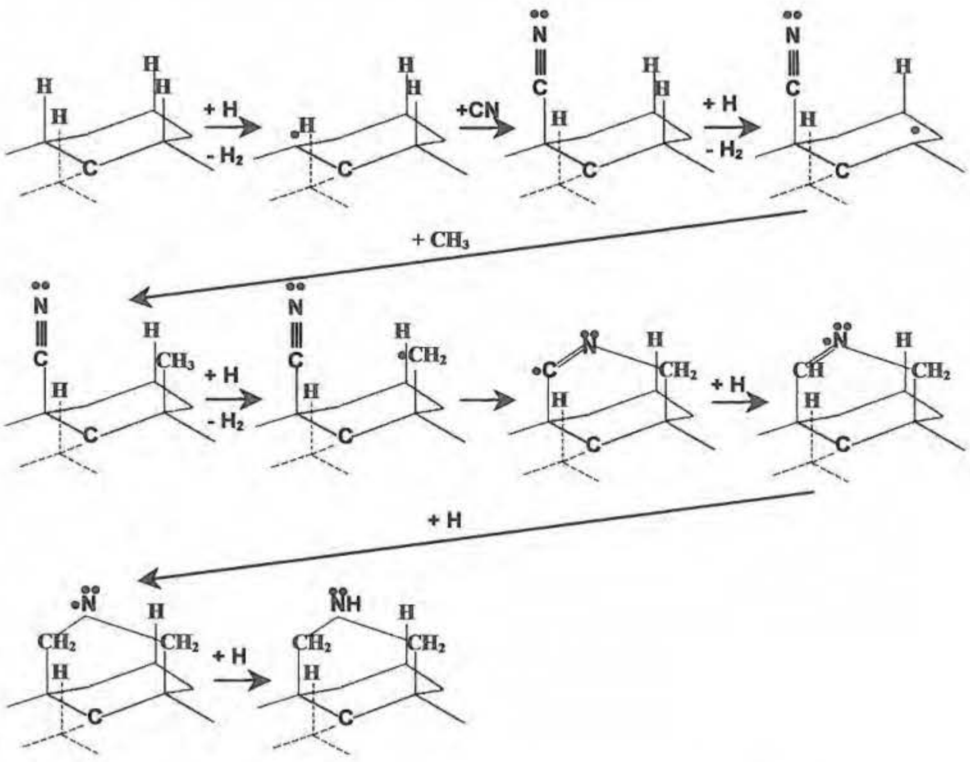

Figure 6.6: CN enhancement of the nucleation rate on {111} surface. No β-scission can occur due to the absence of terminal hydrogen adapted from [105].

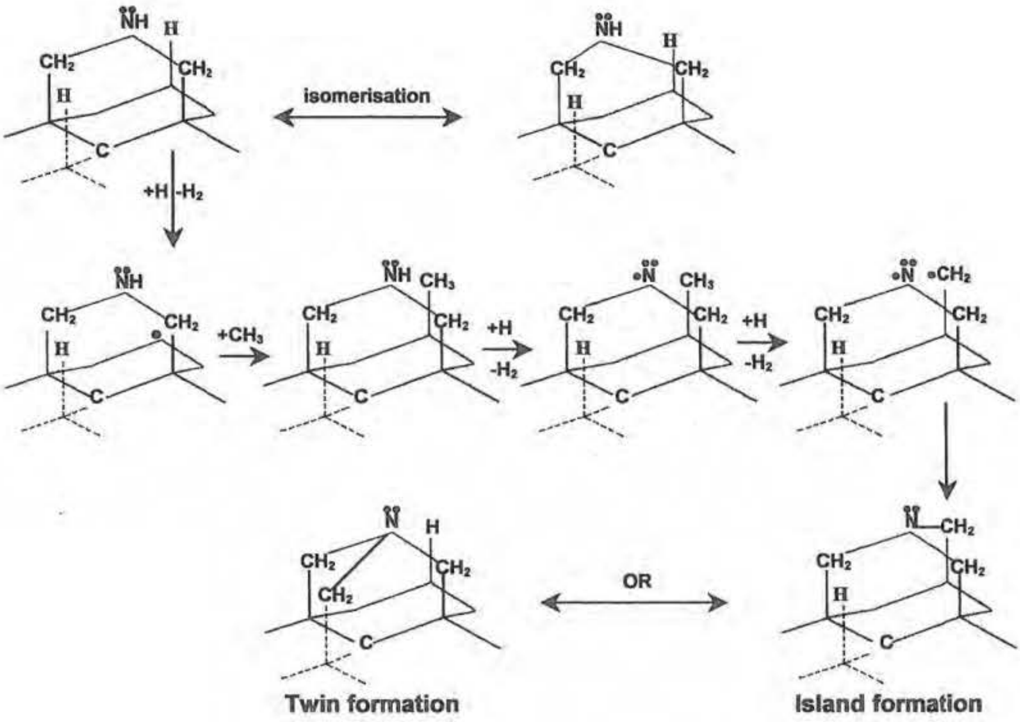

Figure 6.7: Next layer nucleation on {111} surface with nitrogen adapted from [105].

Unreconstructed dihydride (100) surfaces are problematic since adjacent hydrogen atoms are closer than they would be in molecular hydrogen. This structure has to reconstruct in some way, either as full monohydride or as a 50:50 monohydride : dihydride, to satisfy the steric constraints. The reconstruction of the {100} surface eliminates much of the steric energy caused by the neighbouring hydrogens, but it introduces distorted bond angles and thus larger energies for the tetrahedral surface carbons. For diamond, a tetrahedral carbon attached to a surface by one of its four bonds is chemisorbed to a surface site, by two of its four bonds is chemisorbed to a kink site, and by three or four of its four bonds becomes a part of the bulk diamond material.

But how could nitrogen influence the {100} preferential orientation of the diamond film as observed by X-ray diffraction?

To satisfy steric constraints in the diamond lattice, it is conceivable that nitrogen accumulates preferentially in specific growth sectors. An other possibility would be that nitrogen could lock preferentially some growth sites either by the reaction of CN radicals, N atoms, or N_2 activated molecules with active growing sites.

6.4 Conclusions

It is impossible to account for all the reactions involved at the substrate surface and conducting to the growth of a diamond film. The series of chemical reactions presented in this section are not exclusive, since up to now, little is known about the surface energies, the thermodynamics of the chemical reactions and the kinetics involved in the diamond growth processes.

In this chapter, based on existing reaction schemes and models for methane-hydrogen plasma, we showed how the presence of nitrogen could account for the experimental observations, as well for the plasma chemical reactions as for the surface chemical reactions. We demonstrated how the CN radicals are produced in the plasma and at the growing diamond interface and how the nitrogen compounds could influence the oriented growth of the diamond film.

Even if thermodynamical calculations or kinetic Monte Carlo simulation methods do not prove the proposed reaction schemes, they could account for the observed results. We showed that based on bond strength, bond length and steric constraints, some chemical reactions are more likely to occur. We also reported that nitrogen could have a catalytic effect on the growth of diamond, being mainly recycled in the growth process, and accidentally incorporated as a single substitutional species in the diamond lattice.

Atomic nitrogen coming from the dissociation of N_2 in first instance could play the same role as atomic hydrogen in the diamond growth process. The dissociation of N_2 could also be facilitated at the substrate/growing surface. This could explain the increase of the relative CN concentration at the vicinity of the substrate surface as observed by Optical Emission Spectroscopy.

We also showed that nitrogen-containing species could lock or inactivate some surface growing sites leading to the growth of preferentially oriented diamond films as observed by Scanning Electron Microscopy and XRD measurements.

Detailed mechanisms for the incorporation of the hydrocarbon species into the diamond growing surface have been proposed for the diamond (111) low index crystal surfaces.

Nevertheless, no mechanism has been generally accepted as the likely path for the incorporation of gas phase carbon into a bulk diamond structure yet.

7. General conclusions and perspectives

7.1 General conclusions

Since very small amounts of nitrogen in the process gas were found to drastically modify the growth of CVD diamond films, a strict and permanent control of the process parameters is essential to achieve reproducibility in diamond deposition experiments. Nitrogen was mainly found to enhance the growth rate, to promote preferential growth, and to alter the quality of the diamond deposited film. Nitrogen is always present in commercially available gases as impurity at ppm level. Moreover, in most deposition installations, vacuum leaks can be responsible for a non-negligible contribution of nitrogen in the plasma, since N_2 is the major constituent of air.

The scientific and technical understanding of diamond CVD processes has progressed significantly to the point where the generic mechanisms by which diamond is deposited at pressures and temperatures at which it is thermodynamically metastable are well understood. However, generally accepted chemical mechanisms that lead to low-pressure growth of diamond are still lacking, even for the commonly used binary methane-hydrogen feed gas mixture. Therefore, the mechanisms of nitrogen incorporation in a diamond film are still missing too. This is mainly due to the extreme complexity of the processes involved, as it is unlikely that there is a single and simple diamond growth mechanism that applies to all deposition systems and deposition conditions.

Since the processes involved in diamond growth cannot be observed *in situ*, much of our understanding is extracted from the modelling and simulation or inferred from experimental observations. To increase our knowledge on the part taken by nitrogen in the plasma chemistry and in the surface chemical reactions, we investigated several aspects of minute nitrogen addition to the process gases during microwave plasma assisted Chemical Vapour Deposition of diamond.

Optical Emission Spectroscopy, as non-intrusive analysis technique, was used to monitor variations in the plasma composition and chemistry during the deposition processes. Though OES is a very sensitive technique, the identification of the species is limited to the few species with excited electronic states that fluoresce in the plasma.

To get more out of the optical emission spectra than purely qualitative analytical features, we had to characterise the optical set-up and determine its spectral dependence. By doing so, we were able to monitor the evolution of the relative concentration of the various emitting plasma species as a function of the nitrogen fraction added to the feed gas mixture.

The elaboration of an optical probe allowed us to reduce the plasma volume captured by the optical fibre and therefore to attenuate the influence of scattering light on our measurements. Before use, the spectral dependence of the complete optical set-up was settled, and the limit of detection of the various emitting species defined for a wide variety of plasma compositions.

Analysis of the OES spectra showed that microwave plasmas consisting of a mixture of methane and hydrogen always contain the same emitting species: the Balmer emission lines and the Fulcher α bands for respectively hydrogen atoms and molecules, and the CH and C_2 emission bands as carbon containing species. Minute nitrogen addition in the plasma was responsible for the presence of the violet CN emission bands in the emission spectra. Used as is, OES provides only qualitative information about the chemical composition of the gas, as the determination of the ground state concentrations is difficult without detailed knowledge of the excitation processes. Nevertheless, the relative concentration of hydrogen atoms in the plasma could be deduced from the emission intensities by applying actinometry. The temperature of the hydrogen atoms and the C_2 molecules could also be calculated from their respective emission intensities.

We showed that minute nitrogen addition (ppm range) changed significantly the chemistry of the plasma. The relative concentration of CN, CH, and C_2 was found to increase linearly with the nitrogen fraction in the feed gas. Actinometric measurements revealed that the relative H concentration in the plasma increased linearly with the nitrogen concentration in the plasma, while the relative concentration of H_2 decreased over the same interval.

The increase in the gas temperature, as recorded for the vibrational temperature of C_2, could be at the origin of the overall increase of the emission intensities. However, the observed decrease in the relative concentration of H_2 and the temperature of hydrogen atoms can almost completely rule out this assumption. Nitrogen atoms and molecules could in fact facilitate the dissociation of H_2 and CH_4, favouring therefore the formation of the end products, and increasing the concentration of H, CH and C_2, in the plasma as observed by OES. A series of chemical reactions involving nitrogen and responsible for the dissociation of H_2 and CH_4 were developed in the modelling section.

Furthermore, we observed that the addition of larger N-fractions was responsible for a thermalisation of the plasma, though the electron energy distribution function was found to diverge from a Maxwell-Boltzmann distribution with the increasing N-fraction in the feed gas. The discrepancy from a Maxwell-Boltzmann distribution observed mainly for the H_α emission line is probably due to non-radiative de-excitation processes. Actually, rotational and/or vibrational energy transfers could take place between the Balmer H emission lines and the first positive system $B^3\Pi_g$-$A^3\Sigma_u^+$of N_2 molecule, not visible in the frame of our experiments. The measured intensities of some of the H emission line could consequently be seriously underestimated, which, in return, would exclude plasma thermalisation at higher nitrogen fractions.

With the optical probe, we were able to sample the plasma light at different heights in the plasma, and to record variations in the emission intensities as a function of the distance from the substrate surface. These measurements showed that the relative concentration of the H, CH and C_2 increased with the distance from the substrate surface, while the relative concentration of CN decreased exponentially over the same interval. These results suggested that nitrogen addition increased the level of carbon supersaturation at the substrate surface, probably by an increased dissociation of the methane.

By a simple experiment, we demonstrated that the CN radicals are formed as well in the plasma as at the substrate surface. Dissociation of molecular nitrogen could be enhanced by the substrate surface through several mechanisms specified in the modelling section, and increase artificially the concentration of the CN radical at, or close to the substrate surface. These chemical reactions were also developed in our model. We also showed that the relative concentration of CH and CN with respect to C_2 is larger near the substrate surface as in the bulk of the plasma. These results suggested strongly that the CH radicals were also formed at the substrate surface by the etching of chemisorbed carbon species by hydrogen atoms.

Temperature measurements of the gas phase showed that the plasma was near thermal equilibrium close to the substrate surface.

The growth rate of the films increased by almost a factor 4.5 when as little as 95 ppm N_2 was added to the feed gas during deposition. Further increase in the nitrogen concentration did not seem to have any further effect on the growth rate.

Nitrogen was found to increase the number of penetration twins on {111} and {100} crystal facets. The morphology of the diamond film evolved from a polycrystalline texture to a cauliflower texture when the injected nitrogen concentration in the plasma exceeded 800 ppm. In between, {111} and {100} well faceted diamond films could be obtained.

Calculation of the texture coefficient from the XRD pattern showed that the film texture evolved clearly towards a {100}-preferred orientation with increasing nitrogen content in the feed gas mixture.

The analysis of the deposited diamond films showed that the Raman quality ratio Q_D decreased exponentially with the nitrogen content in the feed gas. We found out that at a carbon supersaturation corresponding to a fraction of more than 300 ppm N_2, the deposition of the graphitic phase was favoured with respect to the diamond phase.

The SIMS analysis performed on the deposited films showed that the H and N content in the films increased together with the nitrogen fraction in the feed gas.

The results obtained during the diamond film characterisation could not rule out that nitrogen could also be partially incorporated in non-diamond phase of the film, as the sp^2 fraction in the film increased together with the nitrogen content in the feed gas. According to Bar-Yam and Moustakas [100], the incorporation of nitrogen donors reverses the thermodynamic stability of diamond with respect to graphite, increasing consequently the growth rate of diamond. This phenomenon was observed in our deposition experiments, but only to a certain extent, as the growth rate stabilised rapidly when more than 100 ppm N_2 were added to the plasma.

In our experiments, the addition of nitrogen caused the growth of multiple twinned diamond crystallites at low nitrogen fractions, and the formation of {100} facets at the expense of {111} facets at higher nitrogen contents. This {100} fibre texturing depends critically on the deposition temperature [111].

Based on existing reaction schemes and models for methane-hydrogen plasma, we showed how the presence of nitrogen could account for the experimental observations, as well for the plasma chemistry as for the surface chemistry. We demonstrated how the CN radicals are produced in the plasma and at the growing diamond interface and how the nitrogen compounds could influence the oriented growth of the diamond film. We also showed that based on bond strength, bond length and steric constraints, some chemical reactions are more likely to occur. We also reported that nitrogen could have a catalytic effect on the growth of diamond, being mainly recycled in the growth process, and accidentally incorporated as a single substitutional species in the diamond lattice.

Atomic nitrogen coming from the dissociation of N_2 in first instance could play the same role as atomic hydrogen in the diamond growth process. The dissociation of N_2 could also be facilitated at the substrate/growing surface. This could explain the increase of the relative CN concentration at the vicinity of the substrate surface as observed by Optical Emission Spectroscopy.

Nitrogen-containing species could also lock or inactivate some surface growing sites leading to the growth of preferentially oriented diamond films as observed by Scanning Electron Microscopy and XRD measurements.

Detailed mechanisms for the incorporation of the hydrocarbon species into the diamond growing surface have been proposed for the diamond (111) low index crystal surfaces.

7.2 Perspectives

Volume reduced Optical emission spectroscopy was found to be a useful tool for the characterisation of the plasma during deposition, especially for reducing the perturbation of scattered light on our emission measurements and for registering variations in intensities as a function of the distance from the substrate surface. Though the technique might be improved. The use of a grating with a larger amount of grooves or a monochromator with a longer focal length could significantly enhance the resolution of the spectrometer. For instance, increasing the focal length from 0.46m to 1.25m would increase the theoretical resolution of the spectrometer by an order of magnitude. With an increased resolution, we would be able to calculate the rotational temperature of the various radicals and molecules present in the plasma, and consequently have access to the gas temperature of the system. Gicquel *et al.* [80] showed in a comparative study that the rotational temperature determined by OES coincides with the real gas temperature of the system determined by Laser Induced Fluorescence (LIF).

In addition, a drastic modification of the reaction vessel would be necessary to improve the spatial resolution for the determination of the spatial distribution of the plasma emitting species. The reactor chamber in stainless steel could be replaced by a quartz bell jar, making hence a complete mapping of the plasma ball feasible. With a reaction chamber in quartz, LIF or CARS could be implemented and used to determine the absolute concentration of the various species in the plasma.

A lack of quantitative data for temperature and composition in microwave plasma reactors have led investigators to use models to predict macroscopic observables such as film growth rate and examine near-substrate gas composition for potential growth precursors. For instance, a significant factor complicating reactors models is the presence of the energy source (e.g. D.C. arc jet, hot-filament, RF, microwave, ...). Assumptions must invariably be made in constructing a physical model of the source. Not surprisingly, the particular assumptions strongly affect the predicted temperature and species distributions within the reactor.

It is therefore not possible to construct a single model that can capture the physics of all CVD diamond deposition processes across a range of length scales spanning ten orders of magnitude. Instead, different types of models must be constructed, each one appropriate to a specific range of length and time scales. Molecular-growth models may be constructed based on the kinetic Monte Carlo technique. Continuum models are based on conservation equations for mass, momentum, and energy. To bridge the length-scale gap between the molecular and continuum approaches, it is necessary to implement models that describe the evolution of microstructure and morphology. The models associated with the three length-scale regimes are tightly coupled to one another through the mass and energy flux conservation conditions applicable at the deposition surface. This coupling necessitates that the three different length-scale ranges be considered simultaneously. By the same token, the solutions for the three different scales provide a clear picture of diamond deposition. Nevertheless, more development is needed to extend the microstructural model to more complete spatially resolved descriptions of the reactor, and the atomic model to include twinning and additional growth mechanisms.

8. Bibliography

[1] H.O.Pierson, *Handbook of Carbon, Graphite, Diamond and Fullerenes*, Noyes Publications, Park Ridge, New Jersey, 1993.

[2] J.E.Field, *The properties of Diamond*, Academic Press, London, 1979.

[3] P.K.Bachmann & R.Messier, Chemical & Engineering News, 15 (1989), p.24.

[4] H.Liu & D.S.Dandy, *Diamond Chemical Vapor Deposition: Nucleation and Early Growth Stages*, Noyes Publications, Park Ridge, New Jersey, 1995.

[5] F.P.Bundy, Science, 137 (1962), p.1057.

[6] K.E.Spear & M.Frenklach, *Synthetic diamond: Emerging CVD Science and Technology,* edited by K.E.Spear & J.P.Diskmukes, John Wiley & Sons, New York, 1994, p.243.

[7] H.Liander, ASEA Jl, 28 (1955), p.97.

[8] F.P.Bundy, H.T.Hall, H.M.Strong & R.H.Wentorf, Nature 176 (1955), p.51.

[9] H.B.Dyer, F.A.Raal, L. du Preez & J.H.N.Loubser, Phil. Mag, 11 (1965), p.763.

[10] G.Cowan, B.Dunnington, A.Holtzman, *Process for Synthesizing Diamond*, U.S. Patent 3,401,019 (Sept.10, 1968).

[11] M.N.Yoder, *Diamond Films and Coatings: Development, Properties, and Applications*, edited by R.F.Davis, Noyes Publications, Park Ridge, New Jersey, 1993, p.1.

[12] W.G.Eversole, *Synthesis of Diamond*, U.S. Patents 3,030,187 and 3,030,188 (April 17, 1962).

[13] B.V.Derjaguin, D.V.Fedoseev, B.V.Spitsyn, D.V.Lukyanovich, B.V.Ryabov & A.V.Lavrentev, J.Cryst.Growth, 2 (1968), p.380.

[14] J.C.Angus, H.A.Will & W.S.Stanko, J.Appl.Phys., 39 (1968), p.2915.

[15] J.J.Lander & J.Morrison, Surf.Sci., 4 (1966), p.241.

[16] B.Lux & R.Haubner, *Proceedings 12th Int.Plansee-Seminar Mai 89*, Reutte, Austria, p.615.

[17] K.Kurihara, K.Sasaki, M.Kawaradi and N.Koshino, Appl.Phys.Lett., 52 (1988), p.437.

[18] N.Ohtake and M.Yoshikawa, J.Electrochem.Soc., 137 (1990), p.717.

[19] N.Ohtake and M.Yoshikawa, Thin Solid Films, 212 (1992), p.112.

[20] P.K.Bachmann, D.Leers & H.Lydtin, Diam.Relat.Mater., 1 (1991), p.1.

[21] J.A.Miller, C.F.Melius, Combust. Flame, 91 (1992), p.21.

[22] R.J.Kee, J.A.Miller, T.H.Jefferson, Sandia Tech. Rep. SAND80-8003, *CHEMKIN: A General-Purpose, Problem Independent, Transportable, Fortran Chemical Kinetics Code Package*, Sandia Nat. Lab., 1980.

[23] R.J.Kee, F.M.Rupley, J.A.Miller, Sandia Tech. Rep. SAND87-8215B, *The CHEMKIN Thermodynamic Database*, Sandia Nat. Lab., 1987

[24] C.T.Bowman *et al.*, GRI-Mech, http://www.me.berkeley.edu/gri_mech/ (1996).

[25] J.A.Miller & C.T.Bowman, Prog.Energy Combust.Sci., 15 (1989), p.287.

[26] ME.Coltrin & D.S.Dandy, J.Appl.Phys., 74 (1993), p.5803.

[27] D.S.Dandy & M.E.Coltrin, J.Appl.Phys., 76 (1994), p.3102.

[28] D.G.Goodwin & G.G.Gavillet, J.Appl.Phys., 68 (1990), p.6393.
[29] E.Meeks, Combust. Flame, 92 (1993), p.144.
[30] B.W.Yu & S.L.Girshik, J.Appl.Phys., 75 (1994), p.3914.
[31] N.G.Glumac & D.G.Goodwin, Combust.Flame, 105 (1996), p.321.
[32] K.Hassouni, S.Farhat, C.D.Scott & A.Gicquel, J.Phys.III France, 6 (1996), p.1229.
[33] E.J.Dawnkaski, D.Srivastava & B.J.Garrison, J.Chem.Phys., 104 (1996), p.5997.
[34] M.M.Clark, L.M.Raff & H.L.Scott, Comp.in Phys., 10 (1996), p.584.
[35] A.R.Badzian & R.C.De Vries, Mat.Res.Bull., 23 (1988), p.385.
[36] M.Frenklach & K.E.Spear, J.Mater.Res., 3 (1988), p.133.
[37] M.Frenklach & H.Wang, Phys.Rev., B43 (1991), p.1520.
[38] D.S.Dandy & M.E.Coltrin, J.Mater.Res., 10 (1995), p.1993.
[39] S.J.Harris, Appl.Phys.Lett., 56 (1990), p.2298.
[40] S.J.Harris & D.G.Goodwin, J.Phys.Chem., 97 (1993), p.23.
[41] C.C.Battaile, D.J.Srolovitz, J.E.Butler, J.Appl.Phys., 82 (1997), p.6293.
[42] F.G.Celii & J.E.Buttler, Appl.Phys.Lett., 54 (1989), p.1013
[43] K.E.Spear., J.Am.Ceram.Sci., 72 (1989), p.171.
[44] C.Wild, R.Kohl, N.Herres, W.Müller-Sebert, P.Koidl, Diam.Relat.Mater., 3 (1994), p.373.
[45] A.Van der Drift, Philips Res.Repts., 22 (1967), p.267.
[46] F.G.Celii & J.E.Butler, Ann.Rev.Phys.Chem., 42 (1991), p.643.
[47] Y.Liou, A.Inspektor, R.Weimer, D.Knight & R.Messier, J.Mater.Res., 5 (1990), p.2305.
[48] Y.Muranaka, H.Yamashita & H.Miyadera, Thin Solid Films, 195 (1991), p.257.
[49] Y.Muranaka, H.Yamashita & H.Miyadera, J.Cryst.Growth, 112 (1991), p.808.
[50] S.I.Shah & M.M.Waite, Appl.Phys.Lett., 61 (1992), p.3113.
[51] F.M.Cerio, W.A.Weimer & C.E.Johnson, J.Mater.Res., 7 (1192), p.1195.
[52] W.A.Weimer, F.M.Cerio & C.E.Johnson, J.Mater.Res., 6 (1191), p.2134.
[53] A.P.Dementjev & M.N.Petukhov, Diamond Relat.Mater., 6 (1997), p.486.
[54] A.Badzian & T.Badzian, Appl.Phys.Lett., 62 (1993), p.3432.
[55] R.Locher, C.Wild, N.Herres, D.Behr & P.Koidl, Appl.Phys.Lett., 65 (1994), p.34.
[56] S.Jin & T.D.Moustakas, Appl.Phys.Lett., 65 (1994), p.403.
[57] T-M.Hong, S.-H.Chen, Y.-S.Chiou & C.-F.Chen, Thin Solid Films, 270 (1995), p.148.
[58] G.Z.Cao, L.J.Giling & P.F.A.Alkemade, Diamond Relat.Mater., 4 (1995), p.775.
[59] G.Z.Cao, F.A.J.M.Driessen, G.J.Bauhuis & L.J.Giling, J.Appl.Phys., 78 (1995), p.3125.
[60] G.Z.Cao, W.J.P.van Enckevort & L.J.Giling, Appl.Phys.Lett., 66 (1995), p.688.
[61] W.Müller-Sebert, E.Wörner, F.Fuchs, C.Wild & P.Koidl, Appl.Phys.Lett., 68

(1996), p.759.
[62] S.Bohr, R.Haubner & B.Lux, Appl.Phys.Lett., 68 (1996), p.1075.
[63] G.Z.Cao, J.J.Schermer, W.J.P.van Enckevort, W.A.L.M.Elst & L.J.Giling, J.Appl.Phys., 79 (1996), p.1357.
[64] P.W.May, P.R.Burridge, C.A.Rego, R.S.Tsang, M.N.R.Ashfold, K.N.Rosser, R.E.Tanner, D.Cherns, R.Vincent, Diamond Relat.Mater., 5 (1996), p.354.
[65] R.S.Tsang, C.A.Rego, P.W.May, M.N.R.Ashfold, K.N.Rosser, Diamond Relat.Mater., 6 (1997), p.247.
[66] H.Chatei, J.Bougdira, M.Rémy, P.Alnot, C.Bruch, J.K.Krüger, Diamond Relat.Mater., 6 (1997), p.107.
[67] H.Chatei, J.Bougdira, M.Rémy, P.Alnot, C.Bruch, J.K.Krüger, Diamond Relat.Mater., 6 (1997), p.505.
[68] J.Walker, Rep.Prog.Phys, 42 (1979), p.1605.
[69] A.R.Lang, M.Moore, A.P.W.Makepeace, W.Wierzchowski, C.M.Welbourn, Phil.Trans.R.Soc.London Ser., A337 (1991), p.497.
[70] G.S.Woods, J.A.van Wyck, A.T.Collins, Philos.Mag., B62 (1990), p.589.
[71] A.Grill, *Cold Plasma in Materials Fabrication*, The Institute of Electrical and Electronics Engineers (IEEE) Press, New York, 1994.
[72] N.Hershkowitz, *Plasma Diagnostics*, eds. O.Auciello and D.L.Flamm, Academic Press, New York 1989.
[73] I.B.Chapman, *Glow Discharge Processes: Sputtering and Plasma Etching*, J.Wiley & Sons, New York 1980.
[74] S.Veprek, *Low Temperature (non equilibrium) plasmas*, eds. G.Bruno & G.K.Herb, International Summer School on Plasma Chemistry, 1989.
[75] R.R.Manory, U.Carmi, R.Avni, A.Grill, Thin Solid Films, 156 (1988), p.79.
[76] A.T.Bell, *Plasma Chemistry III*, eds. S.Veprek & M.Venugopalan, Springer-Verlag, Berlin 1980.
[77] G.Herzberg, *Atomic Spectra and Atomic Structure*, Dover Publications, New York 1944.
[78] J.W.Coburn & M.Chen, J.Appl.Phys., 51 (1980), p.3134.
[79] A.Gicquel, K.Hassouni, S.Farhat, Y.Breton, C.D.Scott, M.Lefebvre, M.Pealat, Diamond.Relat.Mater., 3 (1994), p.581.
[80] V.Shogun, A.Tyablikov, E.Shelyhmanov, M.Abachev, W.Scharff, T.Wallendorf, Surf.Coat.Technol., 74-75 (1995), p.571.
[81] T.Lang, J.Stiegler, Y.von Kaenel, E.Blank, Diamond.Relat.Mater., 5 (1996), p.1171.
[82] S.W.Reeves & W.A.Weimer, J.Vac.Sci.Technol., A13 (1995), p.359.
[83] J.L.Cooper & J.C.Whitehead, J.Chem.Soc.Faraday Trans., 88 (1993), p.1287.
[84] G.A.Raiche & J.B.Jeffries, Appl.Opt, 32 (1993), p.4629.
[85] R.H.Tourin, *Spectroscopic Gas Temperature Measurement*, Elsevier Publishing Company, Amsterdam 1966.
[86] A.Gicquel, M.Chenevier, Y.Breton, M.Petiau, J.P.Booth & K.Hassouni, J.Phys.III France, 6 (1996), p.1167.

[87] W.Tan, T.Grotjohn, J.Vac.Sci.Technol., A12 (1994), p.1216.

[88] C.D.Scott, S.Fahrat, A.Gicquel, K.Hassouni, M.Lefebvre, Journal of Thermophysics and Heat Transfert, 10 (1996), p.426.

[89] P.K.Bachman & W.van Enckevort, Diamond Relat.Mater., 1 (1992), p.1021.

[90] G.Herzberg, *Molecular Spectra and Molecular Structure*, Vol.1, 2nd edn., Van Nostrand Reinhold Company, New York 1950.

[91] G.Herzberg, *The Spectra and Structures of Simple Free Radicals*, Cornell University Press, Ithaca, New York 1971.

[92] R.W.B.Pearse & A.G.Gaydon, *The Identification of Molecular Spectra*, 4th edn., Chapman and Hall, London 1976.

[93] J.R.Dean, *Atomic Absorption and Plasma Spectroscopy*, ed. D.J.Dando, John Wiley & Sons, 1997.

[94] J.A.Mucha, D.L.Flamm & D.E.Ibbotson, J.Appl.Phys., 65 (1989), p.3448.

[95] D.S.Rickerby, A.M.Jones & B.A.Bellamy, Surf.Coat.Technol., 37 (1989), p.111.

[96] P.T.Moseley, K.R.Hyde, B.A.Bellamy & G.Tappin, Corros.Sci., 24 (1984), p.547.

[97] J.J.Schermer, J.E.M.Hogenkamp, G.C.J.Otter, G.Janssen, W.J.P.van Enckevort, L.J.Gilling, Diamond Relat.Mater., 2 (1993), p.1149.

[98] C.A.Wolden, C.E.Draper, Z.Sitar, J.T.Prater, Diamond Relat.Mater., 7 (1998), p.1178.

[99] M.A.Tamor & M.P.Everson, J.Mater.Res., 9 (1994), p.1839.

[100] Y.Bar-Yam & T.D.Moustakas, Nature, 342 (1989), p.786.

[101] Y.Yokota, H.Kawarada & A.Hiraki, MRS Symp.Proc., 162 (1990), p.231.

[102] R.A.Bauer, N.M.Sbrockey & W.E.Brower Jr., J.Mater.Res., 8 (1993), p.1993.

[103] E.Hyman, K.Tsang, A.Drobot, B.Lane, J.Casey & R.Post, J.Vac.Sci.Technol.A, 12 (1994), p.1474.

[104] T.R.Anthony, Mat.Res.Soc.Symp.Proc., 162 (1990), p.61.

[105] J.E.Butler, R.L.Woodin, Phil.Trans.R.Soc.Lond., A342 (1993), p.209.

[106] D.L.Baulch, C.J.Cobos, R.A.Cox, C.Esser, P.Frank, T.Just, J.A.Kerr, M.J.Pilling, J.Troe, R.W.Walker, J.Warnatz, J.Chem.Phys.Ref.Data, 21 (1992), p.411.

[107] S.J.Harris & A.M.Weiner, J.Appl.Phys., 74 (1993), p.1022.

[108] S.J.Harris & A.M.Weiner, J.Appl.Phys., 67 (1990), p.6520.

[109] J.Warnatz, *Combustion Chemistry*, edited by W.C.Gardiner, Springer-Verlag, New York 1984.

[110] T.Vandevelde, M.Nesladek, K.Meykens, C.Quaeyhaegens, L.M.Stals, I.Gouzman, A.Hoffman, Diamond Relat.Mater., 7 (1998), p.152.

[111] T.Vandevelde, M.Nesladek, C.Quaeyhaegens, L.Stals, Thin Solid Films, 290-291 (1996), p.143.

[112] T.Vandevelde, M.Nesladek, C.Quaeyhaegens, L.Stals, Thin Solid Films, 308-309 (1997), p.154.
[113] T.Vandevelde, T.D.Wu, C.Quaeyhaegens, J.Vlekken, M.D'Olieslaeger, L.Stals, Thin Solid Films, 340 (1999), p.159.
[114] R.T.Morrison & R.N.Boyd, *Organic Chemistry*, 5th edn., Allyn and Bacon Inc., Boston 1987.
[115] S.M.Hwang, T.Higashihara, K.S.Shin & W.C.Gardiner Jr., J.Phys.Chem., 94 (1990), p.2883.
[116] J.E.Huheey, *Inorganic Chemistry*, 3rd edn., Harper & Row, New York 1983.
[117] S.P.Walch, Chem.Phys.Lett., 208 (1993), p.214.
[118] D.G.Goodwin, J.Appl.Phys., 74 (1993), p.6888.
[119] N.V.Sidgwick, *The organic Chemistry of Nitrogen*, 3rd edn., Clarendon Press, Oxford 1966.
[120] H.Rau & F.Picht, J.Mater.Res., 8 (1993), p.2250.
[121] L.J.Giling & W.J.P.van Enckevort, Surf.Sci., 161 (1985), p.567.

Appendix A

Observed molecular transitions

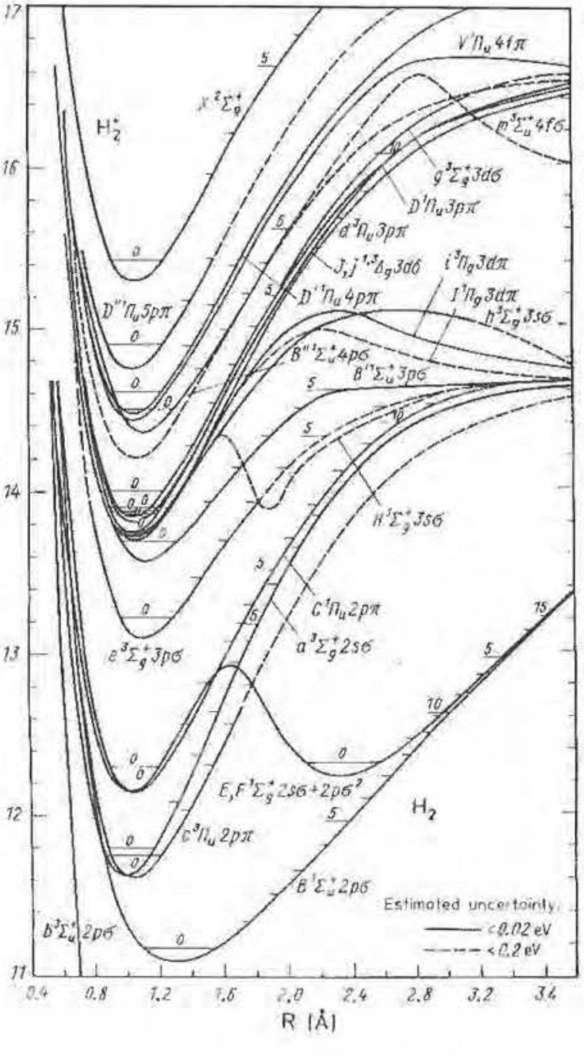

Potential curves of the observed electronic states of the H_2 molecule from M.Konuma, Film Deposition by Plasma Techniques, ed. G.Ecker, Springer-Verlag, Berlin Heidelberg 1992.

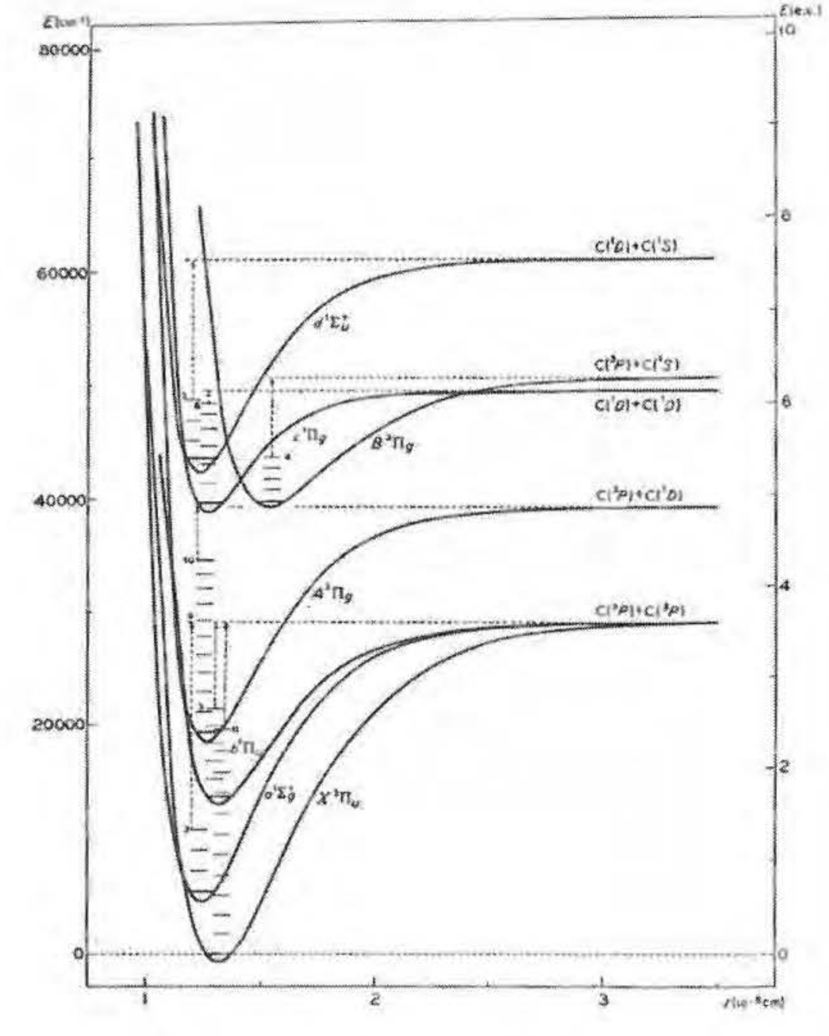

Potential curves of the observed electronic states of the C_2 molecule from G.Herzberg, Molecular Spectra and Molecular Structure, Vol.1, 2^{nd} edn., Van Nostrand Reinhold Company, New York 1950.

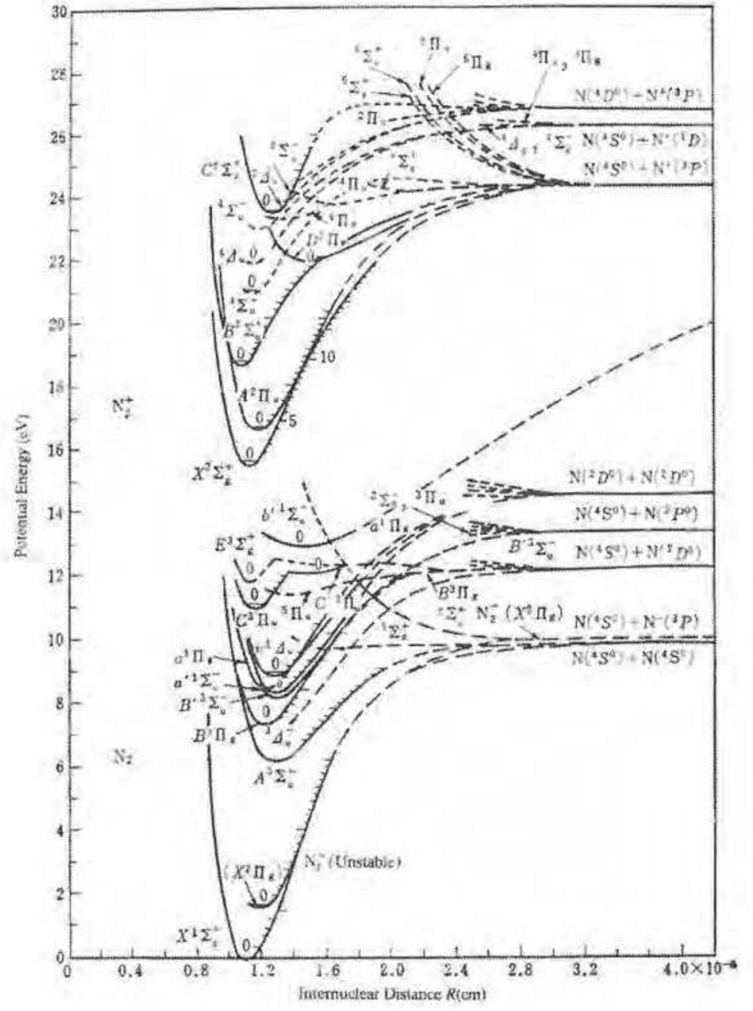

Potential curves of the observed electronic states of the N_2 molecule from M.Konuma, Film Deposition by Plasma Techniques, ed. G.Ecker, Springer-Verlag, Berlin Heidelberg 1992.

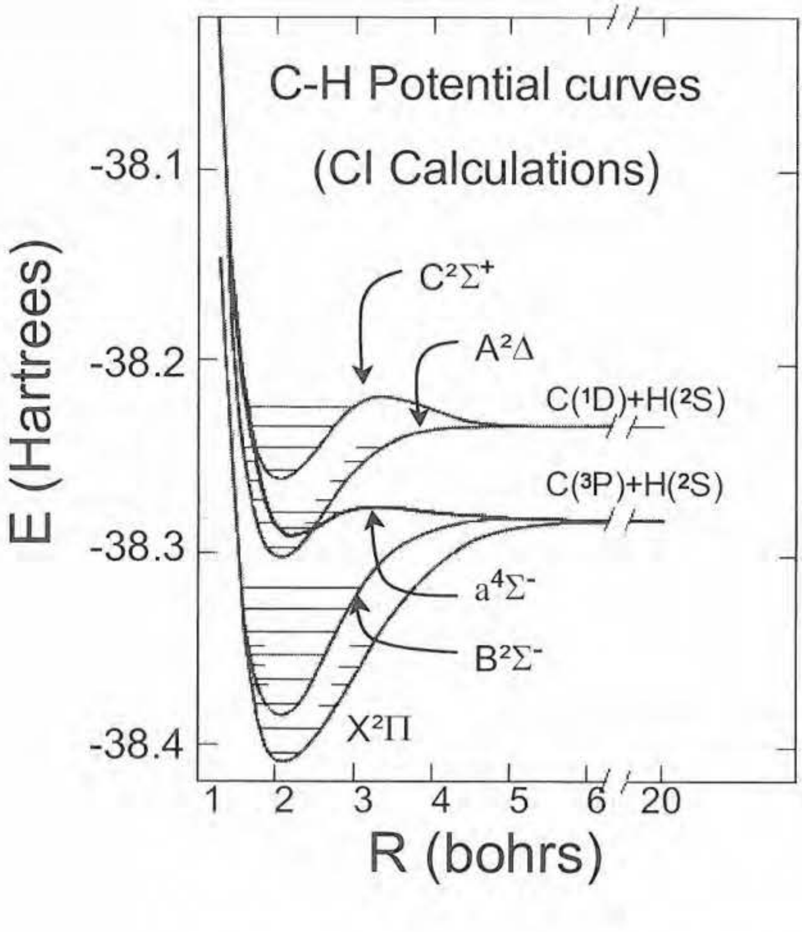

Potential curves of the calculated electronic states of the CH molecule from G.C.Lie, J.Hinze & B.Liu, J.Chem.Phys. 59 (1973), p.1887.

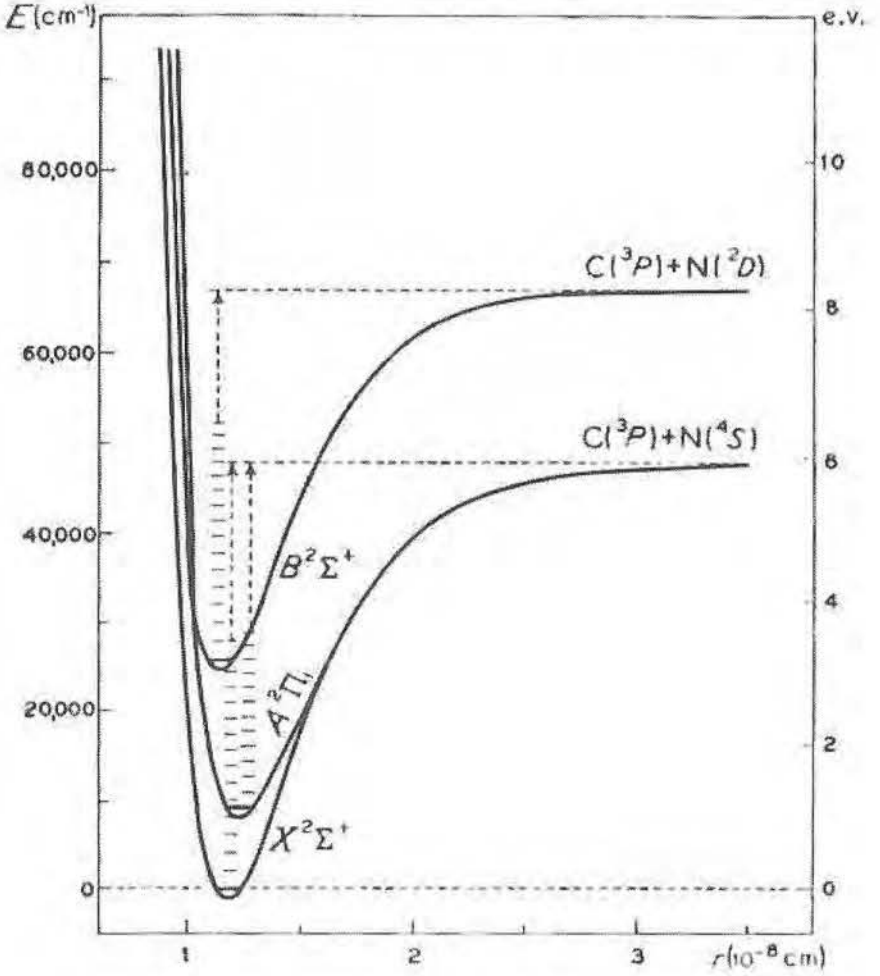

Potential curves of the observed electronic states of the CN molecule from G.Herzberg, Molecular Spectra and Molecular Structure, Vol.1, 2nd edn., Van Nostrand Reinhold Company, New York 1950.

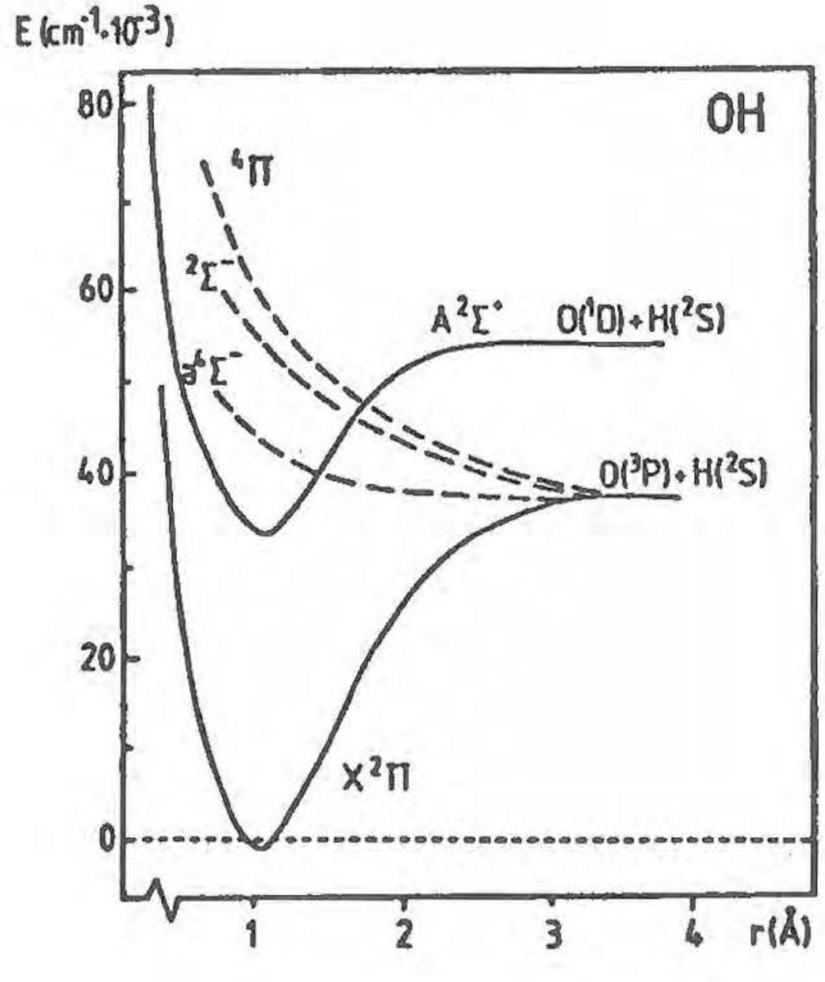

Potential curves of the observed electronic states of the OH molecule from A.Grill, Cold Plasma in Materials Fabrication, The Institute of Electrical and Electronics Engineers (IEEE) Press, New York 1994.

Appendix B

Publications related to this work

1) "*Correlation between the OES plasma composition and the diamond film properties during microwave PA-CVD with nitrogen addition*", T.Vandevelde, T.D.Wu, C.Quaeyhaegens, J.Vlekken, M.D'Olieslaeger, L.Stals, Thin Solid Films, 340 (1999), p.159-163.
2) "*On Nitrogen Incorporation during PE-CVD of Diamond Films*", T.Vandevelde, M.Nesladek, K.Meykens, C.Quaeyhaegens, L.M.Stals, I.Gouzman, A.Hoffman, Diamond and Related Materials, 7 (1998), p.152-157.
3) "*Optical Emission Spectroscopy of the Plasma during Microwave CVD of Diamond Thin Films with Nitrogen Addition and Relation to the Thin Film Morphology*", T.Vandevelde, M.Nesladek, C.Quaeyhaegens, L.Stals, Thin Solid Films, 308-309 (1997), p.154-158.
4) "*On the Development of CVD Diamond Film Morphology due to the Twinning on {111} Surfaces*", G.Knuyt, M.Nesladek, T.Vandevelde, K.Meykens, C.Quaeyhaegens, L.M.Stals, Diamond and Related Materials, 6 (1997), p.435-439.
5) "*On the {111} <111> penetration twin density in CVD diamond films*", G.Knuyt, M.Nesladek, T.Vandevelde, K.Meykens, C.Quaeyhaegens, L.M.Stals, Diamond and Related Materials, 6 (1997), p.1697-1706.
6) "*Optical Emission Spectroscopy of the Plasma during CVD Diamond Growth with Nitrogen Addition*", T.Vandevelde, M.Nesladek, C.Quaeyhaegens, L.Stals, Thin Solid Films, 290-291 (1996), p.143-147.

DOCTORAATSPROEFSCHRIFT

Faculteit Wetenschappen

Dry machining of abrasive aluminium alloys with carbon-based coated tools : dream or reality ?

Bijgevoegde stelling voorgelegd tot het behalen van de graad van
Doctor in de Wetenschappen, richting Natuurkunde

THIERRY VANDEVELDE

Promotor : Prof. dr. L.M. Stals

2000

INSTITUUT VOOR MATERIAALONDERZOEK

LIMBURGS
UNIVERSITAIR
CENTRUM
IN HET CENTRUM VAN DE KENNIS

C3100

DOCTORAATSPROEFSCHRIFT

Faculteit Wetenschappen

Dry machining of abrasive aluminium alloys with carbon-based coated tools : dream or reality ?

Bijgevoegde stelling voorgelegd tot het behalen van de graad van
Doctor in de Wetenschappen, richting Natuurkunde

THIERRY VANDEVELDE

Promotor : Prof. dr. L.M. Stals

2000

INSTITUUT VOOR MATERIAALONDERZOEK

LIMBURGS
UNIVERSITAIR
CENTRUM
IN HET CENTRUM VAN DE KENNIS

Table of contents

Abstract

Today, most machining processes of aluminium alloys are still conducted with coolants to reduce friction and to ease chip removal. The use of coolants has not only an impact on the manufacturing costs, they are also more and more a plague to the environment. The low coefficient of friction and high wear resistance of carbon-based coatings combined with their low sticking properties with respect to aluminium make carbon-based coated tools qualified candidates for the dry machining of aluminium alloys. In this work, we show how a thin CVD diamond coating can significantly improve the tool life while dry machining abrasive aluminium alloys.

1. Introduction

Diamond and Diamond-Like Carbon (DLC) coatings are the subjects of a substantial research effort worldwide. Diamond and, to a lesser extent, DLC exhibit properties that make them extremely attractive for a wide variety of applications. These properties include very high hardness, excellent wear resistance, low coefficient of friction under many regimes, chemical inertness, high thermal conductivity and high electrical resistivity.

Applications of diamond and DLC thin films presently include coatings on tooling for a range of cutting and machining operations on materials such as aluminium alloys, wood and composites, where hardness, chemical inertness and low coefficient of friction of the coatings are of particular significance [1].

Today, most machining processes are still conducted with liquid coolants to reduce the friction processes and to ease chip removal. The use of liquid coolants has not only an impact on the manufacturing cost [2]. They are also a plague to the environment. Therefore the growing interest of the machining industry in the development of new cutting tools that would make the use of coolants obsolete.

The combination of low coefficient of friction and of high wear resistance of carbon-based coatings and their low sticking property with respect to aluminium based alloys make them suited candidates for dry machining applications [1-4]. However, the low thermal stability of some hard carbon coatings is a major drawback for the machining for this kind of application.

DLC can be defined as an amorphous carbon material containing a mixture of sp^3, sp^2 and sp^1 hybridised carbon. DLC has no long-range order, but may have a medium-range ordering. Many DLC films contain a significant amount of hydrogen, dependent on the precursor material. The hydrogen content in the DLC film can vary from less than 10% to up to 60%. The ratio between the carbon atoms in the different coordinations is a function of the total hydrogen content of the films. DLC films can be grown on a range of metallic, ceramic and polymeric substrates at temperatures very much lower than those required for the growth of diamond (below 325°C) [5]. The lower substrate temperatures allow DLC to be deposited onto a range of heat treatable alloys without effecting the strength of the substrate or inducing phase changes. Due to the lower growth temperatures, the problems of residual stresses are less severe. Some of its properties are listed in Table 1.

Table 1
Some properties of natural diamond, CVD diamond and DLC [1].

	Type IIA	***CVD Diamond***	***DLC***
Hardness, $kgmm^{-2}$	> 9000	8000-9000	2000-9000
Mass density, Mgm^{-3}	3,515	2,8-3,5	2,0-2,8
Thermal conductivity at 300K, W/mK	~ 2000	1000-2000	> 400

Since the birth of modern diamond Plasma Assisted-Chemical Vapour Deposition in the early eighties [5], it was thought in short term, that the outstanding tribological properties of diamond (Table 1) could be tailored on a wide variety of tools and find their way to the potentially gigantic market of machining of non-ferrous materials and ceramics [2,3]. However, this goal has never been reached and we are still far away from the original potentiality of diamond coatings for tribological applications. The apparent stagnation in the breakthrough of CVD diamond coated tools has to do with the limitation in the substrate choice due to the specific deposition conditions of diamond CVD, namely the diffusion of carbon in iron, which exclude all iron containing substrates, and the high diamond deposition temperature (>750°C), which limits the substrate choice to hardmetals and ceramic substrates. The latter were found to be too brittle and are as good as abandoned in present time. Hardmetals (cemented carbides), on the other hand, contain cobalt as binder. Cobalt provides additional strength to the tool but has, as iron, high carbon solubility. It is therefore impossible to deposit diamond on untreated tungsten carbide tools. In addition, depending on the fabrication recipe of the carbide manufacturer, hardmetal can also contain a few weight percent of additives (e.g. Cr, Ni) and mixed carbides (e.g. Ta(Nb)C, TiC, Mo_2C, Cr_3C_2). These can negatively interfere during diamond deposition and even be responsible for the poor adhesion of the diamond coating. It is therefore crucial to characterise properly the hardmetal substrate before any diamond coating procedure can begin. For these reasons, carbide grades with low cobalt concentration ($\leq$ 6 wt%), and low additive and mixed carbides content are preferred. Once the suited carbide grade selected, we have to get rid of the cobalt at the substrate interface. The cobalt has to be removed deep enough to avoid retrodiffusion from the bulk to the interface during the deposition process. However, a large cobalt depleted zone can cause brittle cutting edges. The hardmetal pre-treatment is a delicate stage in the coating process and is highly carbide grade dependent. Together with the original choice of a suited carbide grade, the substrate pre-treatment is a crucial stage in the success or failure of the diamond coating process [6,7].

Even if the adhesion of the diamond coating is optimised on the carbide grade, it does not mean that the tool will function properly for any given cutting application. The tool geometry is another important aspect in cutting applications. The contact surface between the tool and the workpiece material, the cutting conditions (e.g. cutting speed, feed and cutting depth) are also elements that will make the difference between success and failure.

In the first part of this work, we evaluate three different commercially available carbon-based coatings for the dry machining of abrasive aluminium alloys : Diamond-like carbon (DLC), Hard Carbon (HC), a sort of DLC coating, and CVD diamond.

In the second part of this work, we propose to study the influence of the carbide grade, tool geometry, cutting parameters and coating thickness during the process of dry turning of abrasive aluminium alloys (AlSi10Mg + 20 wt% SiC).

2. Coating evaluation

2.1 Experimental details

For the turning of the aluminium silicon carbide (AlSi10Mg + 20wt.% SiC) composite, Sandvik K10 WC-Co inserts (geometry CCGX 09T3 04-Al, 5.5wt% Co) are used.

Commercially available CVD Diamond-like (DLC) coatings (Coater 1, Bekaert) and Hard Carbon (HC) coatings (Coater 2, Diarc) were deposited on the cutting inserts. These layers are only available in one thickness range (between 1μm and 2μm). A 6μm and a 20μm thick CVD diamond film were deposited on two cutting inserts by Coater 3 (Balzers).

Commercially available CVD diamond coatings have a hardness between 8000HV and 10000HV.

DLC coatings consist mainly of a mixture of 'diamond' sp^3 and 'graphite' sp^2 hybrid carbon atoms. The level of hardness of hard carbon films depends on the sp^3 concentration in the deposited film. As a result, they can be classified in function of their hardness. Hard carbon films with hardness comprised between 1500HV and 3000HV contain 5% to10% unhydrogenated sp^3 carbon. Hard carbon coatings with hardness from 3000HV to 5000HV have a sp^3/sp^2 ratio of about 15 to 20%. If the sp^3 concentration is close to 100%, then the hardness and the elasticity of the DLC coating are very similar to diamond (8000HV- 9000HV) [8].

Prior to machining, the carbon-based coatings were examined by SEM. The inserts and end-mills were all homogeneously coated. No cracks or lack of adhesion of the coating on the substrate surface could be observed.

According to the Coater specifications, DLC, Hard Carbon and Diamond coatings have a hardness of respectively 2500HV, 5000HV-6000HV, and 9000HV.

The thickness of the DLC and HC coatings is determined with a Calotest on the face of the cutting tools. The thickness of the diamond coating is determined by examination of a cross section of the tool under the microscope.

The end of lifetime of the cutting tools is reached when the wear of the flank (V_b) exceeds 0.3mm or when the measured roughness R_a of the machined material deviates.

Micro-Raman Spectroscopy is used to distinguish the various types of carbon (diamond, graphite, amorphous carbon and hydrogenated carbon) present in the various coatings [9]. The Raman set-up consist of a green light (514.53nm) Ar laser working in a backscattering geometry with a spot size of about 3μm in diameter. The laser power, measured at the substrate surface, varies between 2.5mW and 10mW, depending on the nature of the coating.

The study of the film morphology and the wear analysis of the hard carbon coatings are performed by Scanning Electron Microscopy (SEM). The surface elemental composition of the tools, before and after turning, is determined in the SEM equipped with an Energy-Dispersive X-ray Spectrometer (EDXS).

2.2. Results and discussion

Differences between the 3 hard carbon coatings are clearly visible in the micro-Raman spectra (Fig.1) [9-12]. The diamond coating contains a high sp^3 content (peak at $1332cm^{-1}$) with little sp^2 contribution ($1580cm^{-1}$). HC and DLC coatings contain a mixture of sp^2 and sp^3 hybrid carbon atoms. The microcrystalline sp^3 carbon contribution (around $1355cm^{-1}$) with respect to the sp^2 contribution at $1580cm^{-1}$ is larger for the HC film as for the DLC coating. The proportionally higher degree of sp^3 bonds in the HC film (>70% according to Coater 2) can explain the differences in hardness between the HC and DLC coatings.

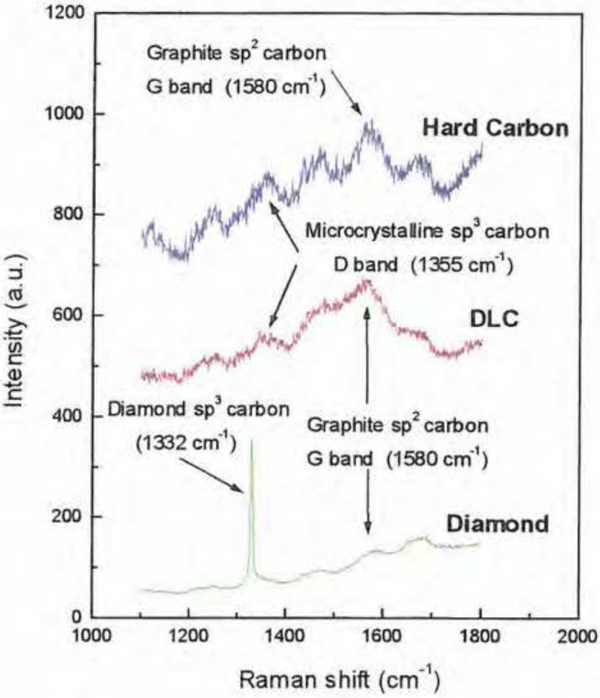

Fig.1 : Micro-Raman spectra of the diamond, DLC and Hard Carbon coatings.

SEM examination shows that the DLC (Fig.2), HC (Fig.3) and diamond (Fig.4) films cover homogeneously the entire substrate surface. The HC and DLC films present no texture, while the diamond coatings are randomly orientated polycrystalline diamond films.

Fig.2 : SEM picture of the DLC coating.

Fig.3 : SEM picture of the Hard Carbon coating.

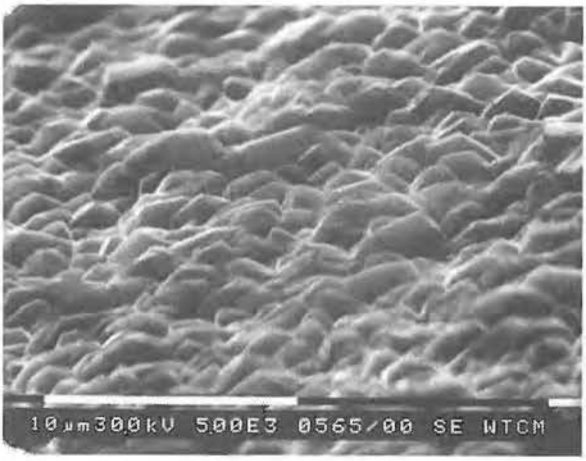

Fig.4 : SEM picture of the diamond coating.

The wear and surface investigations are carried out in a single tooth climb-cut turning process onto a conventional Demoor-type turning centre.

The dry cutting conditions are summarised in Table 2 and the test results summarised in Table 3. The optimum dry turning conditions were defined for a PCD (polycrystalline diamond) tipped tool.

Table 2

Cutting parameters for the dry turning of AlSi10Mg + 20% SiC (optimised dry turning conditions for PCD tipped tools).

Cutting speed (v_c):	100m/min
Feed (f):	0.1mm/rev
Cutting depth (a_p):	0.5mm

Table 3
Results of the dry turning test of AlSi10Mg + 20% SiC as a function of the coating type of the insert.

Coating type	*Thickness (μm)*	*Turning time (min)*	*V_b (mm)*	*End lifetime?*
Non-coated	0	0.17	>1.7	Yes
DLC	1.4	1.33	1.7	Yes
HC	1.6	1.33	1.7	Yes
CVD Diamond	6	12	0.1	Yes
CVD Diamond	20	30	0.16	Yes
PCD tipped tool	--	30	0	No

The tests show that the uncoated cemented carbide inserts cannot be used for this turning application. Breakage of the cutting edge occurs after only 30s. SEM investigation shows severe abrasive wear on the clearance face and large built-up edges at the cutting edge.

The DLC and HC tools exhibit both abrasive and adhesive wear (Fig.5), with transfer of the material from one sliding surface to the other (EDX analysis). The V_b values of the DLC and HC layers are equal to 1.7mm. The deposited HC and DLC layers are immediately worn away leaving the cutting edges uncovered. The thickness and hardness of both coatings are insufficient to resist the highly abrasive wear of the Al-SiC composite.

Fig.5 **:** Clearance face of a Hard Carbon coated WC-Co insert after 1,33min turning. Note the extent of abrasion and the formation of built-up edges.

The best results are obtained with the CVD diamond coated inserts. The clearance face of the diamond (20µm thick) coated insert is depicted in Fig.6. Loosening of the diamond layer from the tool surface is never observed. The end of the tool lifetime is, for the diamond coated inserts, induced by breakage of the cutting edge. Small built-up edges at the cutting edge are also observed (Fig.6). The V_b values of the diamond coated tools are always very small (~0.1mm). Thick diamond films (20µm thick) are more efficient as they last at least twice as long as the thinner ones (6µm thick).

For comparison, the PCD tipped tool did not reach end of lifetime after 30 minutes and showed no abrasive wear. Only small built-up edges on the cutting edge were observed by SEM.

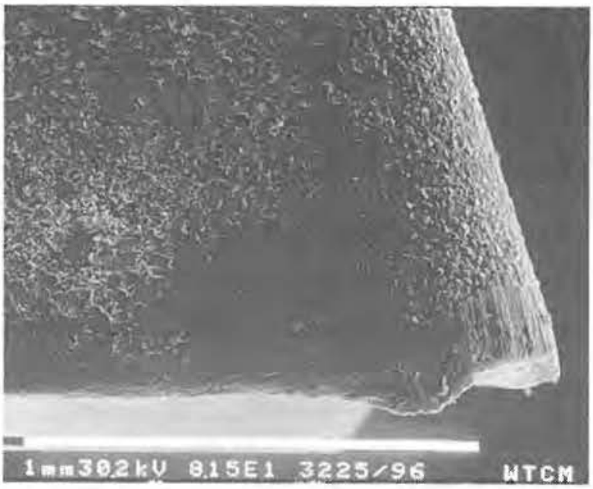

Fig.6 : Clearance face of a 20µm thick CVD diamond coated insert after 30min turning showing the breakage of the cutting edge.

2.3 Conclusions

DLC and HC do not give much improvement in the tool lifetime during the dry turning of Al-SiC composites. This suggests that in both cases the DLC and HC coatings are too soft and not thermally stable enough since both coatings are worn away approximately after the same turning time. The best results were obtained with CVD diamond coated inserts, where the tool lifetime could significantly be increased (6:1 ratio of CVD diamond coated inserts versus non-coated inserts). Diamond coatings reduced significantly the formation of built-up edges on the cutting edges of the tools. Nevertheless, the best tool lifetime is still obtained by PCD-tipped inserts. The advantages of the CVD diamond coatings versus the PCD tipped tools relies mainly in the ability for CVD diamond coating to protect the other crucial parts of the tool, as chip breakers, so that better surface finish of the workpiece can be achieved.

3. Selection of the tool geometry and carbide grade

3.1 Experimental details

The study of the diamond film morphology and the wear analysis of the coated tools were carried out using Scanning Electron Microscopy (SEM), while the cobalt concentration at the tool surface is monitored by a CMI X-Ray Fluorescence spectrometer with a penetration depth of about 6-8µm.

The thickness of the diamond coating was determined in a non-destructive way by using a CMI beta backscatter system with a Promethium source calibrated for this purpose.

The quality of the diamond coating was settled by Micro-Raman spectroscopy. Further details on the Raman set-up can be found in section 2.1.

The bending strength of the cemented carbide tools is determined by a Zwick type Z050 press.

Once the coating selected for this turning application, we studied the influence of the tool geometry and of the substrate material (carbide grade) on the tool performances.

The diamond films were deposited at WTCM using the High Current DC-Arc (HCDCA) Chemical Vapour Deposition technique (Fig.1) with an argon:methane:hydrogen (52:1:47 in volume) gas mixture at a deposition temperature of about 820°C and allowing a growth rate of +/- 1µm/h.

Prior to deposition, the tools are chemically pretreated. The substrates are first cleaned and then etched by Murakami's reagent (10g $K_3[Fe(CN)_6]$ + 10g KOH + 100ml water) in order to obtain a rough surface and favour the mechanical clamping of diamond on the tool surface. The time spent in this 'hardmetal' bath depends on the type of the grade and lies between 10min and 30min. The cobalt at the substrate interface is etched by an acidic solution containing hydrogen peroxide (6ml 96wt% H_2SO_4 + 14ml H_2O_2 + 80ml water). The XRD residual concentration of cobalt at the interface after cobalt etching never exceeds 1wt%. The samples are rinsed in demineralised water in between two wet pretreatments. After etching, the samples are seeded in a isopropanol solution containing diamond (0-1µm grain size) powder (0.35g/100ml) in an ultrasonic bath. The samples are then rinsed twice in isopropanol and dried immediately with hot air. The morphologies of the surface of the hardmetal tools before and after the chemical pretreatment are respectively presented in Fig.9(a) and Fig.9(b).

Fig.7 : Balzers High Current DC-Arc BAI 730D diamond deposition reactor.

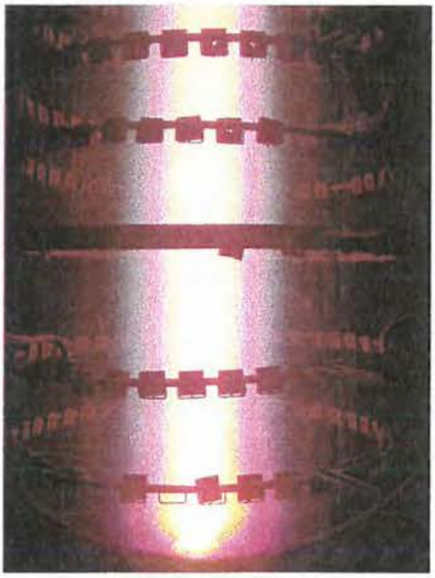

Fig.8 : Cemented carbide inserts during the coating process.

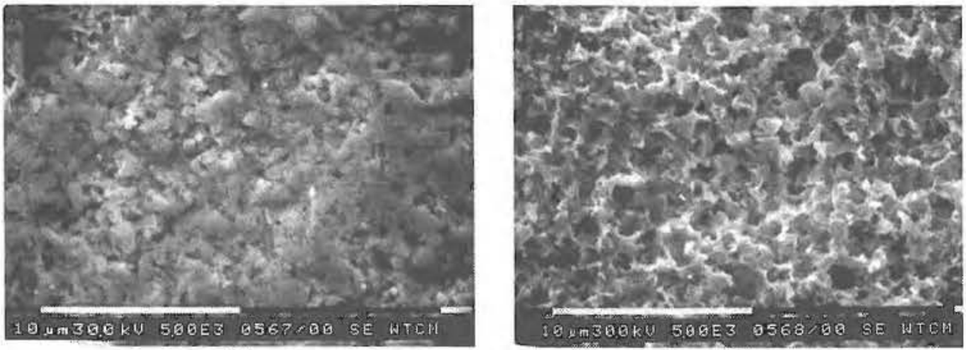

(a) (b)

Fig.9: Morphology of the surface of K01 hardmetal inserts before (a) and after (b) the chemical pretreatment.

The depth of the cobalt etching after the chemical pretreatment (6 to 7µm deep) was determined by the examination of cross sections of the tools by SEM. We could not observe any significant Co retrodiffusion towards the substrate surface after deposition.

The morphology of the diamond coating is depicted in Fig.10.

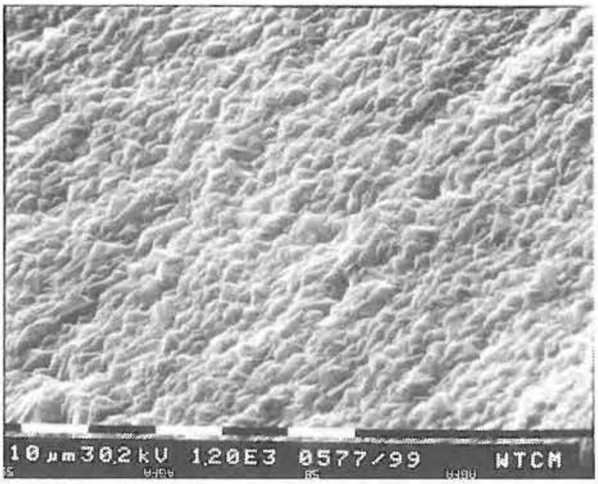

Fig.10 : Morphology of the CVD diamond coating on tool.

The Micro-Raman analysis shows that the diamond films have a very low sp^2 content (Fig.11).

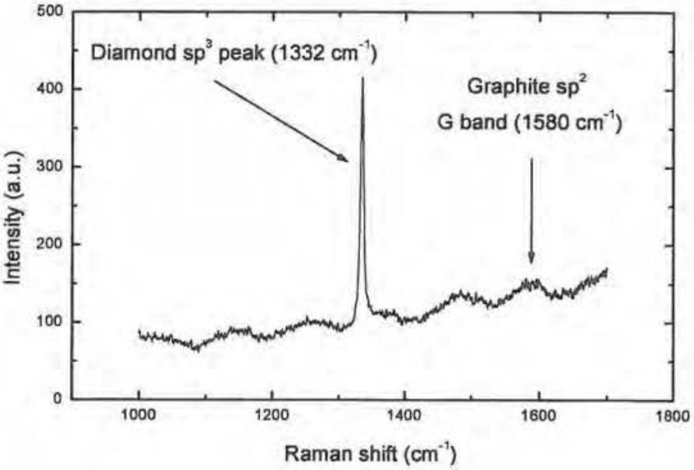

Fig.11 : Micro-Raman spectrum of a 10µm thick CVD diamond film.

The carbide grades selected for the purpose of our study are summarised in Table 4. The surface roughness (R_a) of the tools never exceeded the value of 0.3µm, even after the chemical pretreatment.

Table 4
List and composition of the carbide grades tested.

Manufacturer	**Carbide grade**	**Average grain size (µm)**	**Cobalt content (wt%)**
A (Cérametal)	K05	1-2	4
	K10	1-2	6
	K20	2-4	6
B (Sandvik)	K01	1-2	3.5
	K10	1-2	6
	K20	2	6
C (Widia)	K15	1-2	6

The tested tool geometries are the SPUN 120308, CCGX 090304, VBMT 160412 and VCGT 160404.

The performance of uncoated tools and coated tools with a CVD diamond coating of 6µm, 10µm, and 20µm are compared for the turning conditions summarised in Table 5. These optimised machining conditions are obtained from the optimised dry turning conditions of AlSi10Mg + 20wt% SiC with a PCD tipped tool.

The wear and surface investigations are carried out in a single tooth climb-cut turning process described in section 2.2.

The criteria applied in this section for the tool lifetime are the same as the ones described previously in section 2.2.

Table 5

Optimised dry turning parameters for a PCD tipped tool.

Cutting speed (v_c):	100 m/min
Feed (f):	0.1 mm/rev
Cutting depth (a_p):	0.5mm

3.2 Influence of the tool geometry.

In this section, we investigate the tool performances for two diamond coating thicknesses and four selected tool geometries (CCGX, SPUN, VBMT and VCGT) for one specific carbide grade (Manufacturer B). The dry turning parameters are listed in Table 4. The turning tests show that for a 10µm-thick diamond film, the tool life is extremely dependent on the tool geometry (Fig.11). The SPUN geometry scores as best from the turning test, followed by the VBMT, CCGX and VCGT geometry. It is to note that none of these geometries last longer than 20s when used uncoated. Tool failure is due in all cases to the delamination of the diamond coating on the clearance face.

Even if the CCGX and VCGT geometry are classical geometries for the machining of aluminium, they do not score better when diamond coated. This is probably due to the large nose radius (r_ε) of the SPUN and VBMT geometry, of respectively 0.8mm and 1.2mm, which is responsible for a larger contact area between the diamond coated tool and the workpiece material during the turning process. The larger nose angle reduces probably the internal stress in the diamond film, reducing by the same time the risk of flaking as it spreads the pressure on the clearance face over a much larger area. The CCGX, VBMT and VCGT have all a high positive insert geometry, but only the CCGX and VBMT geometry, which have the largest nose radius, work properly in AlSi10Mg + 20wt% SiC. The performances of the tool increase with the diamond coating thickness (20µm), though not in the same proportions for all geometries. Note that the end of tool life is not reached after 30min for the SPUN and VBMT geometry with a 20µm-thick diamond coating on top.

The roughness (R_a) of the workpiece material was not found to vary much with the tool geometry, as long as the diamond coating remained intact.

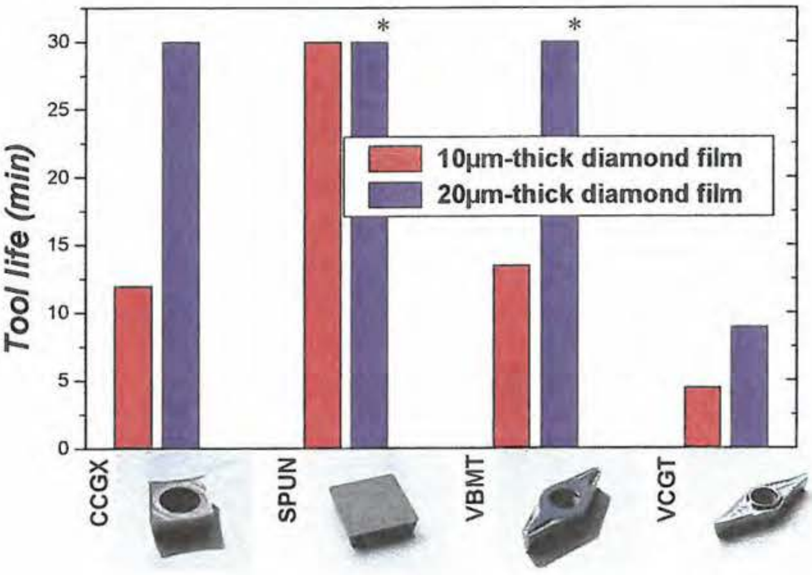

* : not end of tool life

Fig.11 : Tool performances as a function of the tool geometry for a Manufacturer B K10 grade with two diamond coating thicknesses.

3.3 Influence of the carbide grade

We performed a series of tests on SPUN inserts with a 20 µm-thick diamond coating. For this test, we selected the Manufacturer B K01, K10, and K20, Manufacturer A K05, K10 and K20 and Manufacturer C K15 carbide grades. The dry turning parameters are listed in Table 5.

As shown in Fig.12, the Manufacturer B carbide grades with a 20µm-thick diamond coating perform better than the Manufacturer A grades. The Manufacturer B K01 and Manufacturer C K15 score best, followed by the Manufacturer B K10 and K20. Next comes the Manufacturer A K20 followed by the Manufacturer A K10 and K05. The wear analysis shows that the Manufacturer A grades failed because of the breakage of the hardmetal, while the Manufacturer B grades showed flaking of the coating on the clearance face. Note that the Manufacturer B K01 grade did not reach end of tool life after 30min. From the test, it seems that the Manufacturer A grades are much more sensitive to the chemical pre-treatment than the Manufacturer B grades.

The R_a value of the workpiece material was much higher with the Manufacturer A grades ($5\mu m < R_a < 6\mu m$) than with the Manufacturer B and Manufacturer C carbide grades ($0.8\mu m < R_a < 1.2\mu m$).

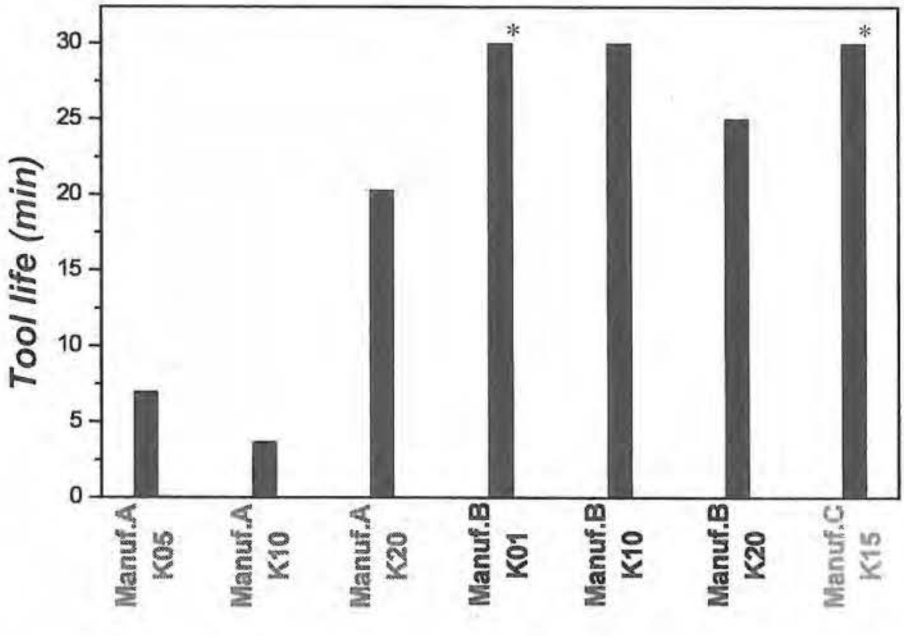

* : not end of tool life

Fig.12 : Tool performances as a function of the carbide grade for a SPUN tool geometry with a 20µm-thick diamond coating.

The resistance to flexion of the pretreated cemented carbide grades diminishes by 35 to 40% with respect to the value of untreated inserts. It is therefore clear that the chemical pretreatment embrittles the hardmetal in a non-negligible way. The bending strength measurements carried out on diamond coated tools reveal that the resistance to flexion is even lower for the diamond coated hardmetals than for the uncoated ones. The bending strength of the cemented carbide grade loses 42 to 46% of its nominal value after the diamond coating procedure. For example, the bending strength of the K10 carbide grade of Manufacturer A has a nominal value of 3200MPa. After the chemical pretreatment, the bending strength drops to 2020MPa, and after deposition, to 1760MPa. This means that the cemented carbide grades loose almost half of its bending strength during the chemical pretreatment and coating process.

3.4 Influence of the cutting conditions

For the best geometry and carbide grade from the two previous test series (i.e. Manufacturer B K01 SPUN 120308), we tried to optimise the cutting parameters.

Fig.13 shows the tool performances as a function of the diamond coating thickness and the dry turning parameters.

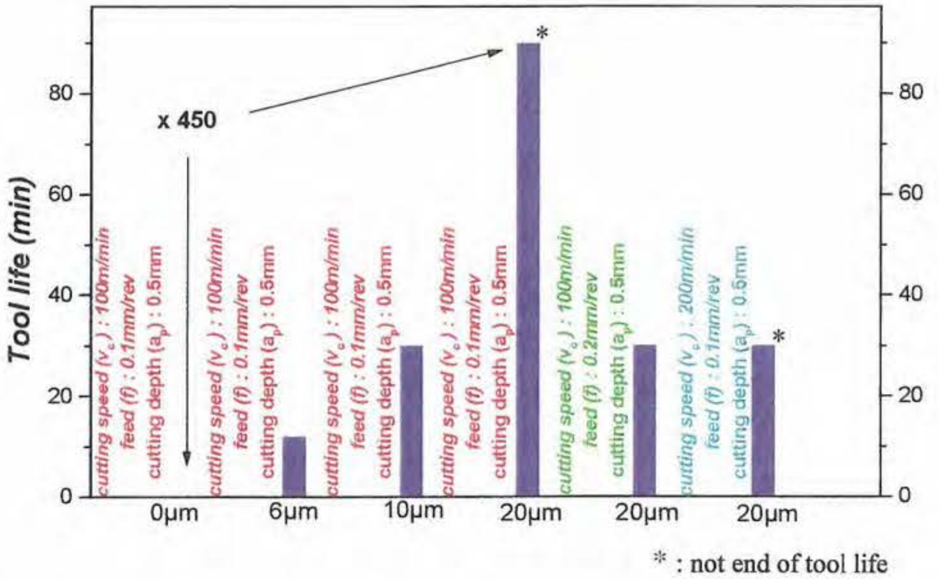

Fig.13 : Tool performances as a function of the cutting conditions for a Manufacturer B K01 SPUN geometry with various diamond coating thicknesses.

For the dry turning conditions used in Table 5, we could increase the tool life by a factor 450 with only a 20µm-thick diamond coating (0.2min for an uncoated insert compared to more than 90min with the 20µm thick diamond coated insert). Note that this specific tool did not even reach the end of tool life after a machining time of 90min. The wear analysis of the tool shows little adhesion of aluminium on the clearance face and no damage of the diamond coating on the tool (Fig.14).

Fig.14 : Wear analysis showing little adhesion of aluminium on the clearance face of the tool after 90min dry machining of AlSi10Mg + 20wt% SiC (v_c = 100m/min, f = 0.1mm/rev, a_p = 0.5mm).

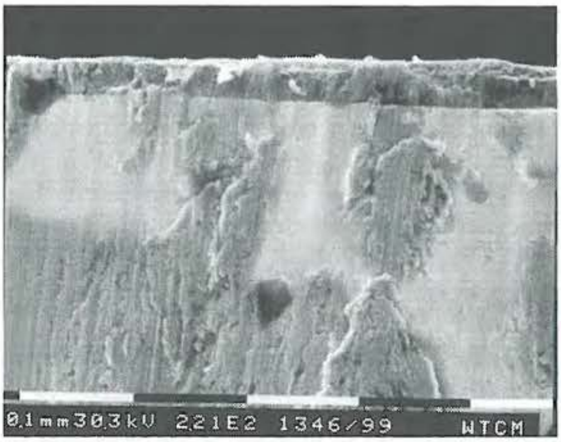

Fig.15 : Wear analysis showing abrasive wear of the hardmetal and adhesion of aluminium on the clearance face of the tool after 30min dry machining of AlSi10Mg + 20wt% SiC (v_c = 100m/min, f = 0.2mm/rev, a_p = 0.5mm).

The 20µm-thick diamond coated insert lasted only for 30 min after increasing the feed to 0.2mm/rev (v_c = 100m/min, f = 0.2mm/rev, a_p = 0.5mm) instead of the initial 0.1mm/rev (see Table 2). Wear analysis of this insert shows flaking of the diamond coating on the clearance face with abrasive wear of the hardmetal (Fig.15).

Doubling the cutting speed (Fig.13, v_c = 200m/min, f = 0.1mm/rev, a_p = 0.5mm) does not affect the surface quality of the workpiece material. The wear analysis of this tool shows sticking of aluminium on the clearance face and rake face and the presence of small built-up edges on the wedge angle (Fig.16). The underlying 20µm-thick diamond coating remains undamaged.

***Fig.16* :** Wear analysis showing adhesion of aluminium on the clearance face and formation of built-up edges on the cutting edge of the tool after 30min dry machining of AlSi10Mg + 20wt% SiC (v_c = 200m/min, f = 0.1mm/rev, a_p = 0.5mm).

3.5. Conclusions

Starting with turning parameters defined for the dry machining of AlSi10Mg + 20wt% SiC with a PCD tipped tool (v_c = 100m/min, f = 0.1mm/rev, a_p = 0.5mm), we were able to optimise the carbide grade, tool geometry and coating thickness for this specific application.

From our turning tests, we were able to define the best carbide grades for our specific pretreatment and diamond deposition technique (Manufacturer B K01, Manufacturer C K15).

It was demonstrated that the chemical pretreatment and the diamond deposition process are responsible for a lost of 42 to 45% of the bending strength of the underlying cemented carbide grade, resulting for some of them, in an almost immediate breakage of the hardmetal during the turning application.

The best tool geometry was found to be a geometry with a large contact area between the tool and the workpiece material, such as the SPUN and VBMT geometry with a large nose radius. With a larger nose radius, the pressure applied on the clearance face during the cutting process is spread over a much larger surface, reducing the chances of flaking of the diamond coating. Variations of the positive geometry of the insert did not seem to influence much the dry turning results.

As long as the diamond coating did not flake, the tool geometry did not much influence the roughness of the workpiece material. On the other hand, the carbide grade type seemed to have some influence on the surface finish, though the surface roughness of the tools did not vary significantly after the chemical pretreatment.

The tool life generally increased together with the diamond coating thickness. The best results were obtained with a 20µm-thick diamond coating.

By optimising the carbide grade and tool geometry (Manufacturer B K01, SPUN 120308) for this turning application, we were able to increase the tool life by at least a factor 450 with a 20µm-thick diamond coated insert compared to an uncoated insert. With these 20µm-thick diamond coated inserts, we were even able to increase the cutting speed by a factor 2, without damaging the tool or increasing the surface roughness of the workpiece material, overwhelming the dry turning results obtained with PCD tipped tools.

4. General conclusions

We showed in this work that the best carbon-based coating for the turning of AlSi10Mg + 20wt% SiC in dry conditions was diamond. DLC and HC do not give much improvement in the tool lifetime during the dry turning of Al-SiC composites. This suggests that in both cases the DLC and HC coatings are too soft and not thermally stable enough since both coatings are worn away approximately after the same turning time. The best results were obtained with CVD diamond coated inserts, where the tool lifetime could significantly be increased (6:1 ratio of CVD diamond coated inserts versus non-coated inserts). Diamond coatings reduced significantly the formation of built-up edges on the cutting edges of the tools.

From our turning tests, we were able to define the best carbide grades for our specific pretreatment and diamond deposition technique (Manufacturer B K01, Manufacturer C K15).

It was demonstrated that the chemical pretreatment and the diamond deposition process are responsible for a lost of 42 to 45% of the bending strength of the underlying cemented carbide grade, resulting for some of them, in an almost immediate breakage of the hardmetal during the turning application.

The best tool geometry was found to be a geometry with a large contact area between the tool and the workpiece material, such as the SPUN and VBMT geometry with a large nose radius. With a larger nose radius, the pressure applied on the clearance face during the cutting process is spread over a much larger surface, reducing the chances of flaking of the diamond coating. Variations of the positive geometry of the insert did not seem to influence much the dry turning results.

As long as the diamond coating did not flake, the tool geometry did not much influence the roughness of the workpiece material. On the other hand, the carbide grade type seemed to have some influence on the surface finish, though the surface roughness of the tools did not vary much after the chemical pretreatment.

The tool life generally increased together with the diamond coating thickness. The best results were obtained with a 20µm-thick diamond coating.

By optimising the carbide grade and tool geometry (Manufacturer B K01, SPUN 120308) for this turning application, we were able to increase the tool life by at least a factor 450 with a 20µm-thick diamond coated insert compared to an uncoated insert. With these 20µm-thick diamond coated inserts, we were even able to increase the cutting speed by a factor 2, without damaging the tool or increasing the surface roughness of the workpiece material, overwhelming the dry turning results obtained with PCD tipped tools.

5. Perspectives

Most machining processes of soft and hard aluminium alloys are still conducted with liquid coolants. This is probably due to the low cost price of uncoated hardmetal tools compared to the relatively high investment of CVD diamond coated tools and PCD tipped tools which do not perform any better in wet turning conditions.

To promote the dry turning of aluminium alloys, the diamond coated tools should meet the expectations of the users, which are a cheap and reliable tools that do not demand too many specific adaptation of their existing machinery park. We are today still very far from the user's needs.

There are also a lot of intrinsic problems linked to the CVD deposition of diamond on hardmetal tools.

The main problem encountered is the limitation to hardmetal substrates with a cobalt binder due to the high deposition temperature, and to carbon diffusion into ferrous metals. These substrates are already more brittle than their steel counterparts. The chemical pretreatment to which the hardmetal is exposed before coating, such as the cobalt depletion from the substrate surface, causes deterioration of the mechanical properties of the substrate.

To cope with this major problem, many research groups worldwide have tried to find an alternative to the chemical pretreatment. One of the alternative is the passivation of the cobalt binder in the near surface region either by the formation of the so-called Co η-phase, or by the formation of intermetallic cobalt phases with boron or aluminium [13]. Other pathways such as carbonitriding of the substrate surface [14], the use of intermediate layers [15, 16], or the cobalt depletion from the interface by a special sintering step in the carbide manufacturing process [17, 18] did not solve the problem either.

The solution could come from the CVD diamond coating of less brittle substrate material, such as steel substrates with the necessary intermediate layer to avoid carbon diffusion in the substrate matrix [19-20].

Acknowledgement

The author would like to thank Ir. Marc Van Stappen and Ir. Peter Perremans of CRIF/WTCM for their precious collaboration.

References

[1] I.R. McColl, J.V. Wood, D.M. Grant, Trans. I.M.F., 72 (3) (2000) 120.

[2] M. Lahres, P. Muller-Hummel, O. Doerfel, Surf. Coat. Tehnol. 91 (1997) 116.

[3] T. Michler, M. Grischke, I. Traus, K. Bewilogua, H. Dimigen, Diamond Relat. Mater. 7 (1998) 459.

[4] D. Neerinck, P. Persoone, M. Sercu, A. Goel, D. Kester, D. Bray, Diamond Relat. Mater. 7 (1998) 468.

[5] M.N. Yoder, in: R.F. Davis (Ed.), Diamond Films and Coatings, Noyes Publications, Park Ridge, NJ, 1993, p.3

[6] T.C.S. Vandevelde, K. Vandierendonck, M. Van Stappen, W. Du Mong, P. Perremans, Surf. Coat. Technol. 113 (1999) 80.

[7] S. Kamiya, H. Takahashi, R. Polini, E. Traversa, Diamond Relat. Mater. 9 (2000) 191.

[8] S. Neuville, A. Matthews, MRS Bulletin, September, 1997, p.22.

[9] P.K. Bachmann, H.D. Bausen, H. Lade, D. Leers, D.U. Wiechert, N. Herres, R. Kohl, P. Koidl, Diamond Relat. Mater. 3 (1994) 1308.

[10] D.S. Knight, W.B. White, J. Mater. Res. 4 (1989) 385.

[11] P.V. Huong, Diamond Relat. Mater. 1 (1991) 33.

[12] E. Liu, B. Blanpain, E. Dekempeneer, F. Loffler, J.P. Celis, J.R. Roos, Diamond Films Technol. 4 (1994) 37.

[13] R. Cremer, R. Mertens, D. Neuschütz, O. Lemmer, M. Frank, T. Leyendecker, Thin Solid Films 355-356 (1999) 127.

[14] T. Sato, Y. Hosokawa, S. Ito, K. Akashi, Surf. Coat. Technol. 112 (1999) 189.

[15] V.G. Ralchenko, A.A. Smolin, V.G. Pereverzev, E.D. Obraztsova, K.G. Korotoushenko, V.I. Konov, Y.V. Lakhotkin, E.N. Loubnin, Diamond Relat. Mater. 4 (1995) 754.

[16] C.R. Lin, C.T. Kuo, R.M. Chang, Diamond Relat. Mater. 7 (1998) 1628.

[17] E.J. Oles, A. Inspektor, C.E. Bauer, Diamond Relat. Mater. 5 (1996) 617.

[18] A. Hirata, H. Zheng, M. Yoshikawa, Diamond Relat. Mater. 7 (1998) 1669.

[19] T. Sato, S. Narumi, S. Ito, K. Akashi, Thin Solid Films 316 (1998) 29.

[20] H.-X. Zhang, Y.-B. Jiang, S.-Z. Yang, Z. Lin, K.-A. Feng, Thin Solid Films 349 (1999) 162.

Appendix A

Publications related to this work:

1. *'Cutting applications of DLC, hard carbon and diamond films'*, T.C.S. Vandevelde, K. Vandierendonck, M. Van Stappen, W. Du Mong, P. Perremans, Surf.Coat.Technol. 113 (1999) 80.
2. *'Verspanen met CVD-diamantbedekte gereedschappen: diamantcoating, nu ook voor aluminium- en houtverspaning'*, T. Vandevelde, Technisch Management, Oktober 2000.
3. *'Dry machining of abrasive aluminium alloys with CVD diamond coated tools'*, T.C.S. Vandevelde, M. Van Stappen, P. Perremans, submitted to Thin Solid Films, October 2000.